Exploiting angular correlations in the rare decay $B_d \to K^{*0}\mu^+\mu^-$ at LHCb

William R. Reece

Blackett Laboratory
Imperial College London

15th July 2010

Imperial College London

A thesis submitted for the degree of Doctor of Philosophy in the Department of Physics at Imperial College London

Abstract

In this thesis, methods for studying the flavour changing neutral current decay $\overline{B}_d \to \overline{K}^{*0}\mu^+\mu^-$ at LHCb are investigated. The decay proceeds via a $b \to s$ loop, and will be sensitive to the effects of new particles, predicted in many models of beyond-the-Standard-Model physics. The formalism used to describe the decay will be introduced, and a number of observables available in its angular distribution presented.

In the first few years of LHCb data taking, the number of signal events available will be relatively small and measurements must be optimized for experimental sensitivity. The vanishing point of the angular observable S_5 will be of particular interest; it has reduced theoretical uncertainties from hadronic form factors and can be extracted with high precision at LHCb. It provides a complementary measurement to that of $A_{\rm FB}$ and $F_{\rm L}$, already considered by *BABAR*, Belle, and CDF.

Once $\mathcal{O}(10^4)$ $\overline{B}_d \to \overline{K}^{*0}\mu^+\mu^-$ signal events have been collected, a full-angular analysis can be performed that will give the maximum available sensitivity to new physics in the decay. It will also provide access to many other observables with reduced theoretical uncertainties that are optimized for sensitivity to particular classes of new physics. It is shown that the full-angular analysis will be a sensitive probe of the decay, and can provide power to distinguish between models if physics beyond the Standard Model is discovered at the LHC. Many of the conceptual issues associated with making this measurement are explored.

Finally, a new decay model of $\overline{B}_d \to \overline{K}^{*0}\mu^+\mu^-$ is presented for the decay simulator EvtGen that allows the model independent simulation of new physics. This model is used to investigate the current state of $b \to s$ observables, and it is shown that their 2009 experimental values are in excellent agreement with the Standard Model.

Acknowledgements

In the last three and a half years, I've had the great pleasure to work on a number of interesting projects with some very talented people. I had always thought that studying for a PhD might be fun; now its (almost) done I'm pleased to confirm that it was! I've had a lot of opportunities for which I'm very grateful – visiting Moscow in winter was a particular highlight for me, as was working in the exciting place that is CERN for two years.

I'd like to start by thanking Imperial College and the Science and Technology Research Council for making all this possible. I've had help from many people over the years; I wouldn't have been able to get this far without their patience and support. Particular thanks should go to:

- ⋆ Ulrik Egede, who went far beyond the call of duty to help me out when I needed guidance and gave me a lot of freedom to pursue topics outside of the norm. I also had much support from other members of the Imperial group, including Mitesh Patel, Tom Blake, Mike Williams, and Andrei Golutvin. Thank you all.

- ⋆ Tobias Hurth, who spent many hours explaining complicated things to me slowly enough that I could follow. I finally understand what a form factor is! I'd also like to thank Quim Matias and Marc Ramon for their amazing enthusiasm over several years, and for hosting me so nicely in Barcelona.

- ⋆ I'd like to thank all the people I've collaborated with in the Ganga project, but particularly Kuba Mościcki, who was always available for a discussion on how to do something *properly*. Oslo in the snow with the Ganga team was another PhD highlight.

- ⋆ Aoife Bhuracha, with whom I collaborated closely for almost my entire PhD. It was fun, but it was also *a lot* of work, and she never complained! We both learnt a lot, and I'm proud of our paper together.

- ⋆ I had many interesting and useful discussions with members of the LHC*b* collaboration. I've met some great people at CERN and had a lot of good times.

- ⋆ My family for everything they've done for me over the years – its taken a lot of effort to get me this far! My final thank you goes to my wife Laura, who put up with me throughout and supported me in so many ways. You're my one and only!

Contents

List of figures

List of tables

Preface

This thesis presents work done by the author over three years, from early 2007 to 2010, and is the result of collaborations with Ulrik Egede, Tobias Hurth, Joaquim Matias, Marc Ramon, and Aoife Bharucha. It also builds on many useful conversations with members of the LHCb collaboration. The author made the following specific contributions to the work presented here:

Chap. 1: Figs 1.2 and 1.9.

Chap. 3: The model independent exploration of $\Lambda_{\rm QCD}/m_b$ corrections for the Standard Model as well as *CP*-violating and *CP*-conserving new physics models using the ensemble method. All figures related to this method (Figs 3.2b, 3.3, and 3.4).

Chap. 4: The development of the three-symmetry constrained fit, including the toy data generator. All experimental sensitivity estimates shown in the chapter and all comparisons made to the projection fits. The update to four symmetry constraints and the analysis of its effects. All figures shown in the chapter.

Chap. 5: The development of the C++ decay model as a plug-in for EvtGen and its integration into the LHCb software framework, including all numerical work required to reproduce a Mathematica version of the model provided by Aoife Bhuracha. The form factor parametrization presented, comparison with the previous model and the performance testing. All figures shown in the chapter.

Chap. 6: The experimental analyses for the observables $A_{\rm FB}$, $F_{\rm L}$, S_3, S_5, A_7, and A_9, including the toy data set generation and the fitting PDFs. The implementation of new physics constraints in C++, following Mathematica versions by Aoife Bhuracha, and the development of the MCMC algorithm used to explore parameter space. All figures shown in the chapter.

Work from this thesis was included in Refs [1–8], as indicated in the text. In addition to the work presented in this thesis, the author was a contributor to the Ganga project for LHCb, leading to Ref. [9].

Chapter 1

Introduction

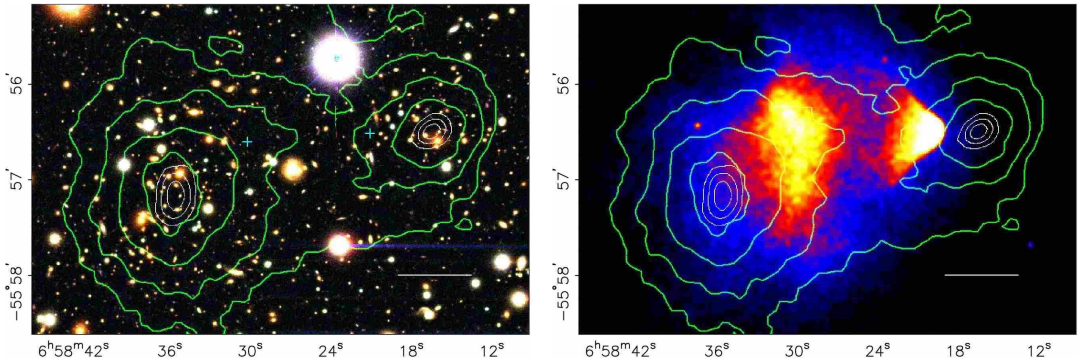

(a) Visible (b) X-ray

Figure 1.1: The merging galactic cluster 1E 0657-558 at visible and X-ray wavelengths. In each case, the white scale bar shows how large a 200 kpc object would appear if it was the same distance from us as the cluster. Fig. from Ref. [10].

1.1 Motivations

A drive to understand the world around us has long been an important feature of mankind. As new technologies have been pioneered, this understanding has grown, leading to a virtuous circle of development that has transformed our lives. Today, we live in a world quite different from our ancient ancestors; however, many of the same questions remain: Where did we come from? How were the things around us made? Why is our universe like it is? We have learnt so much, but as we develop new tools we find new questions to ask.

In modern physics, our ability to make measurements on very large and very small distance scales has left us with many new challenges. An example can be taken from astronomy. In 1933, the Swiss astrophysicist Fritz Zwicky showed that an analysis of the Coma cluster of galaxies led to an estimate of the cluster mass that was much greater than would be expected by looking at its light output

[11]. The large ratio of these two mass estimates (~ 500) led him to propose that there was *dark matter* present in the cluster. Fig. 1.1 shows the merging galactic cluster 1E 0657-558 in both X-ray and visible light [10]. The colliding cluster can be conceptually divided into three components: the stars, the dust and gas, and a hypothetical dark matter halo. The stars can be treated as gravitational point masses at these scales, and do not collide; the two sub-clusters are clearly distinguishable in Fig. 1.1a. The gas and dust, however, interact greatly, producing electro-magnetic (EM) radiation, visible in the X-ray image, Fig. 1.1b. These interactions cause drag, leading to the separation of the visible and X-ray distributions we see. The green lines show contours of the gravitational field, derived from the statistical ellipticity of the background galaxies. These contours follow the distribution of stars, but not that of the gas and dust. The gravitational warping effect extends much beyond the visible boundary of each grouping. This suggests that each sub-cluster is surrounded by a halo of dark and massive matter which does not interact electro-magnetically with the dust and gas.

Results from the Wilkinson Microwave Anisotropy Probe (WMAP) quantify this significantly when combined with other astrophysical constraints [12]. They find that only 4.6% of our Universe is made up of ordinary baryonic matter, and 23% from dark matter. Cosmological evolution models suggest that this must be stable or extremely long lived, low energy (*cold* or *warm*) and non-baryonic (for a review see Ref. [13]). Consideration of the conditions that existed in the early Universe can be used to predict the interaction cross-section required to produce the dark matter density we see today, e.g. Ref. [14]. The cross-section found is one typical of the weak scale, corresponding to particle masses in the 100 GeV-1 TeV range. This conclusion is known as the *WIMP miracle* and ties in with predictions from electroweak theory that there must be new physics (NP) at the TeV scale if any scalar fields present in the Standard Model (SM) are to be protected from logarithmic divergences, e.g. Ref. [15]. The missing *CP* violation in the Universe [16] or the experimental value of $(g-2)_\mu$ [17] are also seen as hints that there is beyond-the-SM physics at work in our Universe.

The LHC project [18] at the Organisation Européenne pour la Recherche Nucléaire (CERN) offers the chance for physics at the TeV scale to be studied in detail for the first time (for a brief review see Ref. [19]). If there is NP active at LHC energies then we may hope to find it. There are two basic approaches to this; we may look for the decays of new massive particles directly or study their virtual contributions to the decays of SM particles. The latter approach is the one taken in *flavour physics*, which deals with the couplings of quarks and leptons from different generations. At the time of writing, the agreement between

precision flavour measurements and SM predictions is rather good (e.g. Ref. [20]), which leaves us with a problem, known as the *new physics flavour puzzle*: If there is NP at the weak scale, why haven't we seen its effects in flavour physics? If we hope to understand the physics of weak scale interactions, then both high-p_T and flavour physics observables must be considered. This thesis is focused on the indirect search for NP contributions to $b \to s$ quark transitions in the rare electroweak penguin decay $\overline{B}_d \to \overline{K}^{*0}(\to K\pi)\mu^+\mu^-$ with the LHCb detector.

1.2 The Standard Model of particle physics

The SM [21–29] is a relativistic quantum field theory that describes the strong, weak, and electromagnetic forces and their interactions with the particles that make up the Universe as we know it today. It is based upon the principle that there are fundamental symmetries of nature that must be respected by any theory which attempts to describe it[1]. These symmetries are specified in the language of group theory as a product of three gauge groups,

$$G_{\rm SM} = SU(3)_C \otimes SU(2)_W \otimes U(1)_Y; \tag{1.1}$$

$SU(3)_C$ describes the strong interaction and $SU(2)_W \otimes U(1)_Y$ the electromagnetic and weak interactions. The twelve generators of the group correspond to the eight gluons, g, three weak bosons, $W^\pm$ and Z^0, and the photon, γ, which respectively mediate the strong, weak, and electromagnetic forces. Together these account for the known phenomenology of the quarks and leptons studied in collider and low-energy experiments.

The matter fields of the SM can be assigned electroweak and strong quantum numbers and grouped into gauge multiplets, as shown in Tab. 1.1. The parity[2] violation seen in weak interactions [36] is implemented by giving the right- and left-handed components different weak quantum numbers, so that they are placed in different multiplets of the $SU(2)_W \otimes U(1)_Y$ group. The left-handed leptons are grouped in $SU(2)_W$ doublets:

$$L_e = \begin{pmatrix} \nu_{e,L} \\ e_L \end{pmatrix}, \quad L_\mu = \begin{pmatrix} \nu_{\mu,L} \\ \mu_L \end{pmatrix}, \quad L_\tau = \begin{pmatrix} \nu_{\tau,L} \\ \tau_L \end{pmatrix}, \tag{1.2}$$

[1] This section has been written following Refs [30–35].

[2] The parity operator changes the sign of all spatial elements in a vector: $\mathcal{P}\begin{pmatrix} x \\ y \\ z \end{pmatrix} \to \begin{pmatrix} -x \\ -y \\ -z \end{pmatrix}$.

and similarly for the quarks,

$$Q_d = \begin{pmatrix} u'_L \\ d'_L \end{pmatrix}, \quad Q_s = \begin{pmatrix} c'_L \\ s'_L \end{pmatrix}, \quad Q_b = \begin{pmatrix} t'_L \\ b'_L \end{pmatrix}, \tag{1.3}$$

while their right-handed chiral partners are placed in singlets:

$$e_R, \quad \mu_R, \quad \tau_R; \tag{1.4}$$

$$u_R, \quad d_R, \quad c_R, \quad s_R, \quad t_R, \quad b_R. \tag{1.5}$$

The L and R labels denote the left- and right-handed projections of the spinor fields (chiralities),

$$\Psi_{L,R} = \frac{1}{2}(1 \mp \gamma_5)\Psi, \tag{1.6}$$

that, in the limit of vanishing particle mass, select the right and left helicity states. The primes indicate that these are the weak and not the mass eigenstates. In the simplest form of the SM, where the neutrino masses vanish, right-handed neutrinos do not interact with any of the known particles and so are removed from the theory, leaving purely left-handed neutrinos. A summary of the symmetry properties of the SM matter fields is shown in Tab. 1.1.

Field	$SU(3)_C$	$SU(2)_W$	$U(1)_Y$	Lorentz
$Q_L^i = \begin{pmatrix} u_L'^i \\ d_L'^i \end{pmatrix}$	3	2	1/6	$(1/2, 0)$
u_R^i	3	1	2/3	$(0, 1/2)$
d_R^i	3	1	$-1/3$	$(0, 1/2)$
$L_L^i = \begin{pmatrix} \nu_L^i \\ e_L^i \end{pmatrix}$	1	2	$-1/2$	$(1/2, 0)$
e_R^i	1	1	-1	$(0, 1/2)$
$H = \begin{pmatrix} H^+ \\ H^0 \end{pmatrix}$	1	2	1/2	$(0, 0)$

Table 1.1: Matter fields of the SM. The dimensions of the $SU(3)_C$ and $SU(2)_W$ representations are shown, as is the $U(1)_Y$ charge, and the properties of the field under the Lorentz group. The i index denotes the generation and runs from one to three.

The SM Lagrangian, $\mathcal{L}_{\text{SM}}$, is the most general re-normalizable Lagrangian that is consistent with the SM gauge group, describes the known particles and implements spontaneous symmetry breaking. It can be divided into three parts:

$$\mathcal{L}_{\text{SM}} = \mathcal{L}_{\text{Kinetic}} + \mathcal{L}_{\text{Higgs}} + \mathcal{L}_{\text{Yukawa}}. \tag{1.7}$$

The requirement of local gauge invariance leads to the natural inclusion of the force carriers of the SM. It is most easily introduced by considering the Lagrangian density for a free Dirac field, ψ, with mass m:

$$\mathcal{L} = \bar{\psi}(i\gamma^\mu \partial_\mu - m)\psi. \tag{1.8}$$

This is invariant under a global phase transformation, known as a *global gauge transformation*,

$$\psi \rightarrow e^{i\alpha}\psi. \tag{1.9}$$

The group of all such transformations is known as $U(1)$. In quantum mechanics (QM) the probability of finding a given state at position $\hat{x}$ can be found by taking the squared modulus of the wave-function,

$$P(\hat{x}) = |\psi|^2 = \psi^*\psi. \tag{1.10}$$

The probability density $P(\hat{x})$ is invariant under the global gauge transformation showing that α is not an observable, but it is also invariant under the more general *local gauge transform*,

$$\psi(\hat{x}) \rightarrow e^{i\alpha(\hat{x})}\psi(\hat{x}), \tag{1.11}$$

where this transformation can be also extended to transform $SU(N)$ spinors [37]. In order to *enforce* conservation of this symmetry on Eq. (1.8), the derivative can be replaced by a new *covariant derivative*,

$$D_\mu^{\mathrm{QED}} \equiv \partial_\mu + ieA_\mu, \tag{1.12}$$

where A_μ is a new vector gauge field, the photon. It is required if we are to include derivative terms in the Lagrangian, which describe how the spinor $\psi(\hat{x})$ transforms as $\hat{x}$ changes. We note that adding a mass term $m^2 A_\mu A^\mu$ is forbidden without spoiling the invariance; the photon is required to be massless.

These ideas can be extended to include the more complex SM group. In this case the covariant derivative required is

$$D^\mu \equiv \partial^\mu + ig_s G_a^\mu L_a + igW_b^\mu T_b + ig'B^\mu Y, \tag{1.13}$$

leading to the force carriers of the SM: G_a^μ are the eight gluon fields, W_b^μ the three bosons of the weak interaction and B^μ is a single hypercharge boson, all of which are also massless. The L_a terms are the generators of $SU(3)_C$ (the 3×3 Gell-Mann matrices), the T_b terms are the $SU(2)_W$ generators (the Pauli matrices), and the Ys are the $U(1)_Y$ charges. Finally, g_s, g, and g' are the associated gauge

coupling constants. In order to recover the Quantum Electrodynamics (QED) result, the SM group must be spontaneously broken, reducing the group from $SU(3)_C \otimes SU(2)_W \otimes U(1)_Y \rightarrow SU(3)_C \otimes U(1)_Q$, where the quantity

$$Q \equiv Y + T^3 \tag{1.14}$$

is conserved and can be identified with the electric charge quantum number. In order to implement this spontaneous symmetry breaking, a single scalar field,

$$H = \begin{pmatrix} H^+ \\ H_0 \end{pmatrix}, \tag{1.15}$$

is added to the theory, leading to the term

$$\mathcal{L}_{\text{Higgs}} = (D_\mu H)^\dagger (D^\mu H) - V(H), \tag{1.16}$$

appearing in the Lagrangian. The electroweak symmetry is broken by the Higgs potential, $V(H)$, an example of which is shown in Fig. 1.2. The symmetry breaking mixes the W and Y bases,

$$\begin{pmatrix} Z^0 \\ A \end{pmatrix} = \begin{pmatrix} \cos\theta_w & -\sin\theta_w \\ \sin\theta_w & \cos\theta_w \end{pmatrix} \begin{pmatrix} A^3 \\ B \end{pmatrix}, \tag{1.17}$$

to form the physical Z^0 and γ, where θ_w is the *weak mixing angle*. The mechanism is outlined for $U(1)$ in the caption of Fig. 1.2, however, the details for the $SU(2)_W \otimes U(1)_Y$ are similar but more involved. This transformation allows for gauge invariant mass terms for the Z^0 and $W^\pm$ to be generated and predicts a simple relationship between their coefficients,

$$m_W = m_Z \cos\theta_w. \tag{1.18}$$

Testing this and other predictions of the theory has led to remarkable agreement being found between SM predictions and precision electroweak data, e.g. Refs [38, 39].

The quarks and leptons do not acquire masses during this process, and this must be changed if the SM is to describe nature. Our choice of placing the left- and right-handed components of the fermion fields in different gauge multiplets means that we can not include a mass term in the Lagrangian without violating the local gauge symmetry. Spontaneous symmetry breaking can again be used to introduce fermion masses in a gauge invariant way. The quarks and leptons get

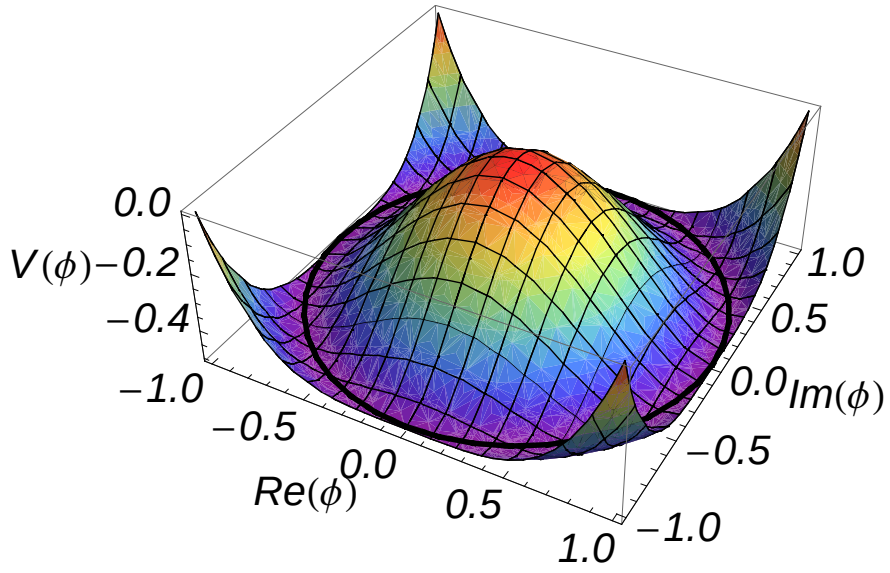

Figure 1.2: An example of a Higg's potential that leads to spontaneous symmetry breaking. In this case, the potential $V(\phi) = -\mu^2\phi^*\phi + \frac{\lambda}{2}(\phi^*\phi)^2$ leads to a $U(1)$ invariant minimum at $\langle\phi\rangle = \phi_0 = \left(\frac{\mu^2}{\lambda}\right)^{1/2}$. Decomposing ϕ around its minimum gives $\phi = \phi_0 + \frac{1}{\sqrt{2}}(\phi_1 + i\phi_2)$, so that $V(\phi) \approx -\frac{1}{2\lambda}\mu^4 + \frac{1}{2}\cdot 2\mu^2\phi_1^2$; ϕ_1 acquires a mass, $\sqrt{2}\mu$, while ϕ_2 is left massless.

masses because of their *Yukawa*[3] couplings to the Higgs doublet,

$$\mathcal{L}_{\text{Yukawa}} = g_u^{ij}\bar{u}_R^i H^T \epsilon Q_L^j - g_d^{ij}\bar{d}_R^i H^\dagger Q_L^j - g_e^{ij}\bar{e}_R^i H^\dagger L_L^j + \text{h.c.} \tag{1.19}$$

where repeated i, j indices are summed and ϵ is the antisymmetric matrix[4]. The non-zero vacuum expectation value of the H doublet,

$$\langle H\rangle = \frac{1}{\sqrt{2}}\begin{pmatrix}0\\ v\end{pmatrix}, \tag{1.20}$$

produces mass terms,

$$\Delta\mathcal{L}_{\text{Yukawa}} = -\frac{1}{\sqrt{2}}\lambda_e v\bar{e}_L^i e_R^i - \frac{1}{\sqrt{2}}\lambda_d v\bar{d}_L^i d_R^i - \frac{1}{\sqrt{2}}\lambda_u v\bar{u}_L^i u_R^i + \text{h.c.} \tag{1.21}$$

These terms give rise to the 3×3 quark and lepton mass matrices,

$$\mathcal{M}_u = v\lambda_u/\sqrt{2}; \quad \mathcal{M}_d = v\lambda_d/\sqrt{2}; \quad \mathcal{M}_e = v\lambda_e/\sqrt{2}, \tag{1.22}$$

where λ_i are the dimensionless and re-normalizable Yukawa couplings. We can

[3]Named following the ideas presented in Ref. [40].

[4] $\epsilon = \begin{pmatrix}0 & 1\\ -1 & 0\end{pmatrix}$.

define matrices, $\mathcal{U}$, which diagonalize the Yukawa couplings so that all Higgs interactions are generation specific,

$$\mathcal{U}(u,R)^\dagger \mathcal{M}_u \mathcal{U}(u,L) = \begin{pmatrix} m_u & 0 & 0 \\ 0 & m_c & 0 \\ 0 & 0 & m_t \end{pmatrix}, \tag{1.23}$$

$$\mathcal{U}(d,R)^\dagger \mathcal{M}_d \mathcal{U}(u,L) = \begin{pmatrix} m_d & 0 & 0 \\ 0 & m_s & 0 \\ 0 & 0 & m_b \end{pmatrix}, \tag{1.24}$$

$$\mathcal{U}(e,R)^\dagger \mathcal{M}_e \mathcal{U}(e,L) = \begin{pmatrix} m_e & 0 & 0 \\ 0 & m_\mu & 0 \\ 0 & 0 & m_\tau \end{pmatrix}. \tag{1.25}$$

For the leptons, this poses no problem as neutrino masses may be neglected. To diagonalize the quark Higgs couplings however requires different transformations for the u_L and d_L fields, which are part of the same $SU(2)$ doublet. We can redefine the original quark doublets as

$$Q_d = \begin{pmatrix} u'_L \\ d'_L \end{pmatrix} = \begin{pmatrix} \mathcal{U}(u,L) u_L \\ \mathcal{U}(d,L) d_L \end{pmatrix} = \mathcal{U}(u,L) \begin{pmatrix} u_L \\ V_{\mathrm{CKM}} d_L \end{pmatrix}, \tag{1.26}$$

where V_{CKM} is the unitary Cabibbo-Kobayashi-Maskawa (CKM) matrix [28, 29], defined as,

$$V_{\mathrm{CKM}} = \mathcal{U}(u,L)^\dagger \mathcal{U}(d,L) \tag{1.27}$$

$$= \begin{pmatrix} V_{ud} & V_{us} & V_{ub} \\ V_{cd} & V_{cs} & V_{cb} \\ V_{td} & V_{ts} & V_{tb} \end{pmatrix}. \tag{1.28}$$

Making the relevant substitutions in the SM Lagrangian leaves the quark kinematic terms, as well as the Z^0 and A couplings unaffected. However the W couplings are not invariant under V_{CKM}, leading to tree-level flavour changing charged interactions mediated by the $W^\pm$.

The unitarity constraint in the CKM matrix means that not all the elements are independent; further re-phasings of the quark fields can be used to remove five parameters, leaving three independent angles, θ_{12}, θ_{13}, θ_{23}, and a single *CP*-

violating[5] phase, δ. The most common parametrization has become [41],

$$V_{\rm CMK} = \begin{pmatrix} c_{12}c_{13} & s_{12}c_{13} & s_{13}e^{-i\delta} \\ -s_{12}c_{23} - c_{12}s_{23}s_{13}e^{i\delta} & c_{12}c_{23} - s_{12}s_{23}s_{13}e^{i\delta} & s_{23}c_{13} \\ s_{12}s_{23} - c_{12}c_{23}s_{13}e^{i\delta} & -c_{12}s_{23} - s_{12}c_{23}s_{13}e^{i\delta} & c_{23}c_{13} \end{pmatrix}, \qquad (1.29)$$

where $s_{ij} \equiv \sin\theta_{ij}$, $c_{ij} \equiv \cos\theta_{ij}$, and the angles are chosen so that $s_{ij}, c_{ij} \geq 0$. Experimentally, $s_{13} \ll s_{23} \ll s_{12} \ll 1$, meaning that there is clear hierarchy in the matrix structure, with off-diagonal elements being much smaller than diagonal elements. To an accuracy of better than $\mathcal{O}(0.05)$, we may write,

$$V_{\rm CMK} \approx \begin{pmatrix} 1 & \lambda & 0 \\ -\lambda & 1 & 0 \\ 0 & 0 & 1 \end{pmatrix}, \qquad (1.30)$$

where $\lambda = 0.2257\ ^{+0.0009}_{-0.0010}$ [41].

Many of the measurements made in B-physics investigate corrections to this picture, illustrated by the over-constrained unitary triangle, shown in Fig. 1.3. This makes use of the Wolfenstein parametrization [42], with the following definitions:

$$s_{12} = \lambda = \frac{|V_{us}|}{\sqrt{|V_{ud}|^2 + |V_{us}|^2}}; \quad s_{23} = A\lambda^2 = \lambda \left|\frac{V_{cb}}{V_{us}}\right|; \quad s_{13}e^{i\delta} = V_{ub}^* = A\lambda^3(\rho + i\eta);$$

so that we can write $V_{\rm CKM}$ as

$$V_{\rm CKM} = \begin{pmatrix} 1 - \lambda^2/2 & \lambda & A\lambda^3(\rho - i\eta) \\ -\lambda & 1 - \lambda^2/2 & A\lambda^2 \\ A\lambda^3(1 - \rho - i\eta) & -A\lambda^2 & 1 \end{pmatrix} + \mathcal{O}(\lambda^4). \qquad (1.31)$$

The unitarity of the CKM matrix requires that, e.g.,

$$V_{ud}V_{ub}^* + V_{cd}V_{cb}^* + V_{td}V_{tb}^* = 0. \qquad (1.32)$$

This relation prescribes a triangle in the complex plane; one of six which may be drawn. We define

$$\bar{\rho} + i\bar{\eta} = -\frac{V_{ud}V_{ub}^*}{V_{cd}V_{cb}^*}, \qquad (1.33)$$

so that expanding in a Taylor series around λ, we have,

$$\bar{\rho} = \rho - \frac{1}{2}\rho\lambda^2 + ...; \qquad \bar{\eta} = \eta - \frac{1}{2}\eta\lambda^2 + ... \qquad (1.34)$$

[5]The charge conjugation operator, $\mathcal{C}$, negates the charge quantum number, so $\mathcal{C} : e^- \to e^+$. CP is the combination of this and the parity operator previously defined.

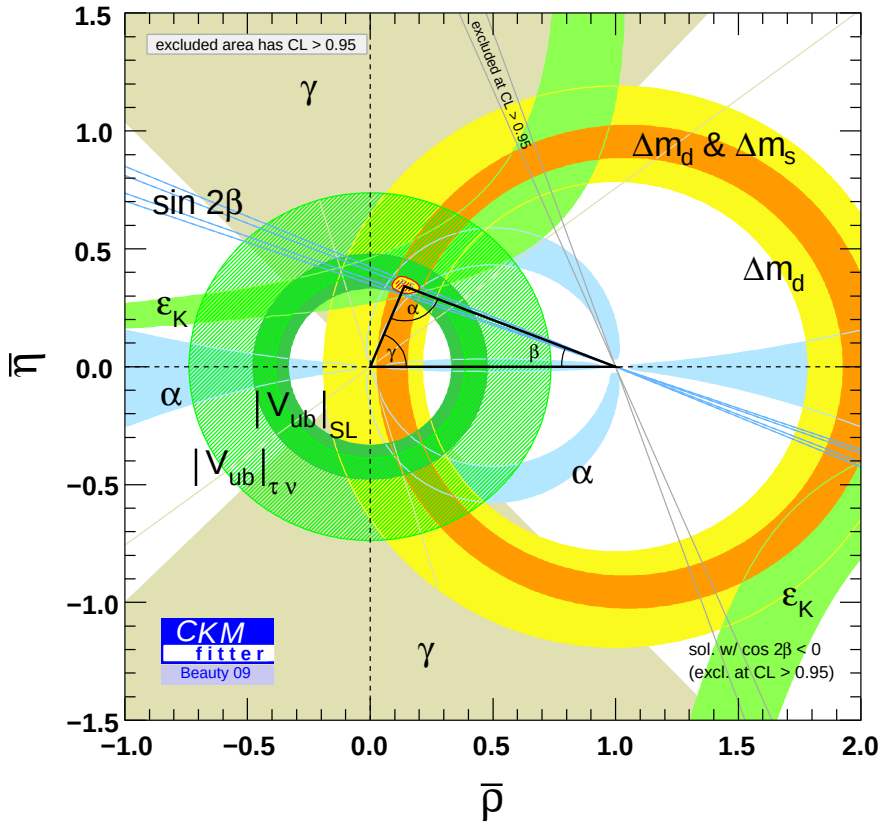

Figure 1.3: The current (summer 2009) status of the CKM matrix [43, 45].

The height of this triangle in the $\bar{\rho} - \bar{\eta}$ plane directly measures the *CP*-violation seen in the SM, while the angles are defined as

$$\beta = \arg\left(-\frac{V_{cd}V_{cb}^*}{V_{td}V_{tb}^*}\right); \quad \alpha = \arg\left(-\frac{V_{td}V_{tb}^*}{V_{ud}V_{ub}^*}\right); \quad \gamma = \arg\left(-\frac{V_{ud}V_{ub}^*}{V_{cd}V_{cb}^*}\right). \tag{1.35}$$

Fig. 1.3 combines many different measurements from the *B*-factories and the TeVatron to make multiple constraints on parameter space to check for inconsistencies which would be a sign of physics beyond the CKM picture. The length of each side of the triangle is $\mathcal{O}(\lambda^3)$, illustrating the precision required to make these measurements. This framework has been extensively tested at the *B*-factories and the TeVatron and has been found to be in excellent agreement with data [43, 44]. While some discrepancies have been reported, the overall picture is one of great consistency with the CKM picture, and so with the SM.

1.3 Rare decays

As discussed in Sec. 1.1, we are looking for the effects of NP at the weak scale, m_W, which naturally leads us to consider diagrams involving weak transitions. As any new particles discoverable at the LHC will likely have masses $\mathcal{O}(10^2\,\text{GeV})$, the decays of heavy SM particles will be of particular interest [46]; specifically the τ lepton and the t and b quarks. The mass hierarchy is such that $m_t \gg m_b > m_\tau$ [41]. The t quark has a huge mass relative to other SM particles; despite the large numbers that will be produced at the LHC, making detailed measurements will be very challenging due to the complex decay topologies involved.

The decays of the b quark are experimentally attractive for a number of reasons. It is the heaviest of the quarks that form bound states. These states are relatively stable, and decay a measurable distance from where they are produced[6]. This allows for their identification in a hadronic environment, by looking for decay vertices displaced from the primary interaction point. At the LHC, they will be produced in $b\bar{b}$ pairs via processes like $g \to b\bar{b}$ in huge quantities: the LHCb collaboration estimates that $\mathcal{O}(10^{12})$ $b\bar{b}$ pairs will be produced at their interaction point per nominal year of data taking [47]. The effects from high mass scale particles in the decays of the b quark will, in general, be less significant than for the t quark, however this may be compensated for by the large statistics and higher selection efficiencies available.

The study of rare b decays is an attempt to combine the advantages of making precision B-physics measurements with the probing of high mass scale processes. We define a *rare decay* as being one which proceeds via an electroweak flavour changing neutral current (FCNC) loop process, which are forbidden at tree-level in the SM. In the case of the $b \to s$ quark transition, the large mass of the t quark means that the electroweak contribution can be significant even where Quantum Chromodynamics (QCD) processes are also active [48]. One strategy is to consider final states were the loop contribution from electroweak processes must dominate. The canonical example of this are the $b \to s\gamma$ decays.

The one-loop SM diagrams for $b \to s\gamma$ are shown in Fig. 1.4. In this case, QCD effects only contribute as corrections, and relatively clean theoretical predictions can be made for its inclusive branching ratio [49]. This can also be measured cleanly at the B-factories (see Ref. [20] and references therein). If there are new massive particles acting on the weak scale, they may be able to enter the $b \to s$ loops, altering the branching fraction we see. Current measurements are, however, in good agreement with the SM predictions, and this represents one of the greatest challenges for the NP hypothesis. A more extensive treatment of the current state

[6]The B meson has a mean lifetime of $\tau_B = (1.530 \pm 0.009) \times 10^{-12}\,\text{s}$[41].

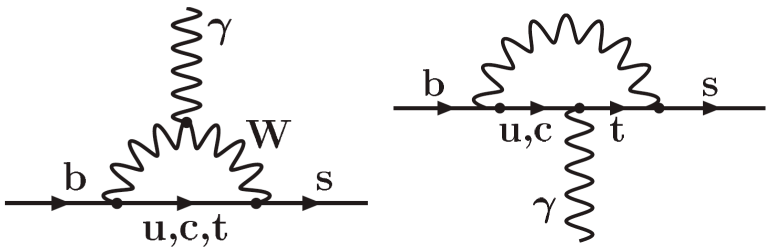

Figure 1.4: SM diagrams for the rare decay $b \to s\gamma$. Figures from Ref. [30].

of $b \to s$ constraints is given in Sec. 6.6. However, $\mathcal{B}(B \to X_s\gamma)$ is not the end of the story. It is only sensitive to certain *classes* of NP effects that could be added to Fig. 1.4. Other rare decays provide overlapping and complementary measurements of the underlying electroweak parameters and may be sensitive to NP effects with different underlying gauge structures. To take these ideas further requires the introduction of the Operator Product Expansion (OPE).

1.3.1 The Operator Product Expansion

Effective field theories in particle physics[7] are built on the idea that the typical energies involved in a particular process define a scale, μ, for that process. The contributions from virtual particles with masses much greater than that scale are suppressed [46]. This can be thought of in terms of the typical distances involved in an interaction. Unstable massive particles generally have short lifetimes so the distances over which they can be involved in a process must also be short. Processes operating at different scales are both spatially and temporally separated, and so *decoupled*.

The force carriers of the weak interaction are very heavy relative to the masses of the SM particles we see in the world around us; the typical distances at which the weak force operates on are very small. Effective theories enable us to model a process at the mass scale relevant to the particles involved. The canonical example of this is Fermi's description of β decay [50], shown in Fig. 1.5. The

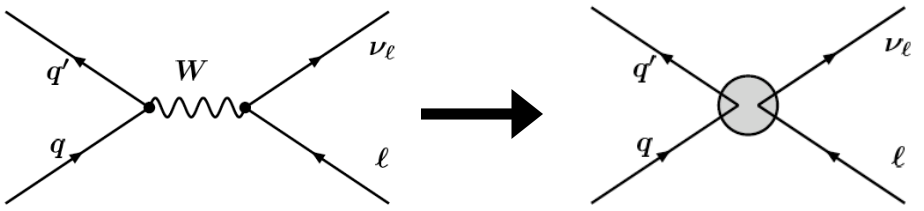

Figure 1.5: The electroweak process of β-decay in the full and effective pictures. Figures from Ref. [30].

[7]The following section is based on Refs [30, 35].

weak vertex is parametrized as an effective vertex with a coupling constant G_F, the Fermi constant, given by

$$G_F = \frac{\sqrt{2}}{8}\frac{g^2}{m_W^2} = 1.16637(1) \times 10^{-5}\,\mathrm{GeV}^{-2}, \tag{1.36}$$

where g is the coupling constant of the weak force [41]. Fermi's theory is invariant under *local* $SU(2)_W \otimes U(1)_Y$, and corresponds to the limit of the SM with infinite heavy boson masses.

The framework of effective field theories is often applied to weak interactions of the b quark. Rather than treat b decays with the full SM, we *integrate out* the particles whose masses are significantly greater than that of the b quark, such as the weak bosons and the t quark. This allows us to concentrate on modelling the physics active at the scale $\mu \approx m_b$, which is dominated by QCD, while still including the effects from higher scale physics.

Making this separation requires that our *full theory* can be *parametrized* at the scale at which it is active. For the SM, this is the weak scale, $\mu = m_W$. We can write the full SM Hamiltonian in terms of an effective Hamiltonian, so that for a given process

$$\langle f|\mathcal{H}_{\text{full}}|i\rangle = \langle f|\mathcal{H}_{\text{eff}}|i\rangle = \sum_k \mathcal{C}_k(\mu)\,\langle f|\mathcal{O}_k|i\rangle \Big|_\mu, \tag{1.37}$$

where the *Wilson coefficients*, $\mathcal{C}_k(\mu)$, parametrize the effects of physics acting on scales higher (shorter range) than μ, and $\mathcal{O}_k$ are matrix elements, often referred to as *local operators*, for physics acting on lower scales (longer ranges) [51]. This is know as the Operator Product Expansion. The values of the Wilson coefficients can be found by *matching* the full and effective Hamiltonians at the weak scale. They represent the coupling constants on effective vertexes, the gauge structure of which are specified by the local operators. An illustration of this may be seen in Fig. 1.5 for the process of β-decay.

The Wilson coefficients can be calculated with high precision in the SM, e.g. Ref. [52], matching *order-by-order* in α_s; the same can also be done for NP models, such as the Minimal Supersymmetric Standard Model (MSSM) [53]. The values of the Wilson coefficients are sensitive to the underlying physics model, and will change from their SM values in the presence of new terms in the true $\mathcal{H}_{\text{full}}$ found in nature. They are *process independent*, and so may be determined separately from many different measurements. If we can measure these coefficients, we can either discover or exclude *entire classes* of NP, as classified by the underlying gauge structure of each corresponding operator. This makes the OPE treatment of B decays extremely powerful for making model independent tests of the SM.

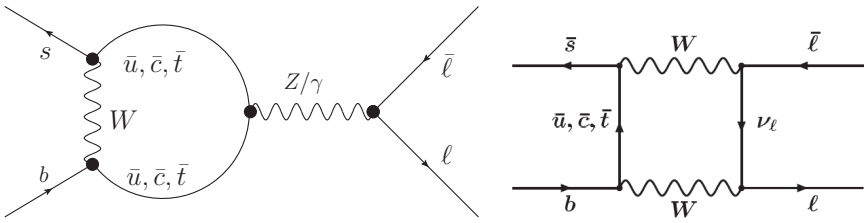

Figure 1.6: Contributions to $b \to s\ell^+\ell^-$ corresponding to $\mathcal{O}_9$ and $\mathcal{O}_{10}$. Figures from Ref. [30].

The effective Hamiltonian relevant for this thesis is given in Eq. (1.38) and describes the inclusive transition $b \to s\ell^+\ell^-$:

$$\mathcal{H}_{\text{eff}} = -\frac{4\,G_F}{\sqrt{2}}\lambda_t \left(\mathcal{C}_1\mathcal{O}_1^c + \mathcal{C}_2\mathcal{O}_2^c + \sum_{i=3}^{6} \mathcal{C}_i\mathcal{O}_i + \sum_j (\mathcal{C}_j\mathcal{O}_j + \mathcal{C}'_j\mathcal{O}'_j) \right), \tag{1.38}$$

where $j = 7, 8, 9, 10, P, S$ and $\lambda_t = V_{tb}V_{ts}^*$ – a combination of the relevant CKM matrix elements. The most important contributions are given in the SM by the operators $\mathcal{O}_{7,9,10}$, defined in Eqs (1.39), (1.41), and (1.42) (e.g. Refs [54–56]).

$$\mathcal{O}_7 = \frac{e}{g^2}\bar{m}_b(\bar{s}\sigma_{\mu\nu}P_R b)F^{\mu\nu}, \qquad \mathcal{O}'_7 = \frac{e}{g^2}\bar{m}_b(\bar{s}\sigma_{\mu\nu}P_L b)F^{\mu\nu}, \tag{1.39}$$

$$\mathcal{O}_8 = \frac{1}{g}\bar{m}_b(\bar{s}\sigma_{\mu\nu}T^a P_R b)G^{\mu\nu\,a}, \qquad \mathcal{O}'_8 = \frac{1}{g}\bar{m}_b(\bar{s}\sigma_{\mu\nu}T^a P_L b)G^{\mu\nu\,a}, \tag{1.40}$$

$$\mathcal{O}_9 = \frac{e^2}{g^2}(\bar{s}\gamma_\mu P_L b)(\bar{\ell}\gamma^\mu \ell), \qquad \mathcal{O}'_9 = \frac{e^2}{g^2}(\bar{s}\gamma_\mu P_R b)(\bar{\ell}\gamma^\mu \ell), \tag{1.41}$$

$$\mathcal{O}_{10} = \frac{e^2}{g^2}(\bar{s}\gamma_\mu P_L b)(\bar{\ell}\gamma^\mu\gamma_5 \ell), \qquad \mathcal{O}'_{10} = \frac{e^2}{g^2}(\bar{s}\gamma_\mu P_R b)(\bar{\ell}\gamma^\mu\gamma_5 \ell). \tag{1.42}$$

$\mathcal{O}_7$ corresponds to the SM diagrams shown in Fig. 1.4 and describes the emission of a photon during the $b \to s$ transition; the photon undergoes leptonic pair production to produce the $\ell^+\ell^-$ pair seen in the final state. A gluonic version of this operator, $\mathcal{O}_8$, also contributes, but is much suppressed in the SM, and considered unpromising for NP. There are also the vector, $\mathcal{O}_9$, and axial, $\mathcal{O}_{10}$, operators, contributions to which are shown in Fig. 1.6.

The operators all have right-handed partners, denoted with a prime, that are suppressed by a factor of m_s/m_b in the SM. The contributions of $\mathcal{O}'_i$ for $1 \leq i \leq 6$ are normally neglected as their impact is either heavily constrained or generically very small. $\mathcal{O}'_{7-10}$ can be greatly enhanced by NP and are of particular interest (e.g. Ref. [57]). For $\mathcal{C}'_{7,8}$, both the helicity suppressed and non-suppressed terms can be included as

$$\mathcal{C}'_{7,8} = \frac{m_s}{m_b}(\mathcal{C}_{7,8}{}^{\text{SM}} + \mathcal{C}_{7,8}^{\text{NP}}) + \mathcal{C}'_{7,8}{}^{\text{NP}}. \tag{1.43}$$

This may lead to large effects in the case where NP contributes to both right-

and left-handed Wilson coefficients.

It is also possible to include scalar and pseudoscalar operators, $\mathcal{O}_{S,P}$, and their primed equivalents which vanish in the SM, but may arise in certain NP scenarios such as the MSSM, due to scalar or pseudoscalar particles in the loops. These are:

$$\mathcal{O}_S = \frac{e^2}{16\pi^2} m_b (\bar{s} P_R b)(\bar{\mu}\mu), \qquad \mathcal{O}'_S = \frac{e^2}{16\pi^2} m_b (\bar{s} P_L b)(\bar{\mu}\mu), \tag{1.44}$$

$$\mathcal{O}_P = \frac{e^2}{16\pi^2} m_b (\bar{s} P_R b)(\bar{\mu}\gamma_5\mu), \qquad \mathcal{O}'_P = \frac{e^2}{16\pi^2} m_b (\bar{s} P_L b)(\bar{\mu}\gamma_5\mu). \tag{1.45}$$

For convenience, the following combinations of Wilson coefficients are defined:

$$\begin{aligned}
C_7^{\text{eff}} &= \frac{4\pi}{\alpha_s}\mathcal{C}_7 - \frac{1}{3}\mathcal{C}_3 - \frac{4}{9}\mathcal{C}_4 - \frac{20}{3}\mathcal{C}_5 - \frac{80}{9}\mathcal{C}_6, \\
C_8^{\text{eff}} &= \frac{4\pi}{\alpha_s}\mathcal{C}_8 + \mathcal{C}_3 - \frac{1}{6}\mathcal{C}_4 + 20\mathcal{C}_5 - \frac{10}{3}\mathcal{C}_6, \\
C_9^{\text{eff}} &= \frac{4\pi}{\alpha_s}\mathcal{C}_9 + Y(q^2), \\
C_{10}^{\text{eff}} &= \frac{4\pi}{\alpha_s}\mathcal{C}_{10} \\
C_{7,8,9,10}^{\prime\,\text{eff}} &= \frac{4\pi}{\alpha_s}\mathcal{C}'_{7,8,9,10}\,,
\end{aligned} \tag{1.46}$$

where the function $Y(q^2)$ is as given in Ref. [54] and includes the doubly-Cabibbo suppressed contributions which lead to *CP*-violation in the SM. If NP was discovered at the LHC, making measurements of the Wilson coefficients in $b \to s\ell^+\ell^-$ would allow its underlying gauge structure to be probed, giving guidance to model builders as they work to replace the SM.

The Wilson coefficients parametrize effects from particles with masses higher than μ; to describe physics at the m_b scale, they must be *evolved* down from the matching scale, m_W. As the scale is brought downwards, the effects of more particles are integrated out from the local operators and into the Wilson coefficients, making the coefficients dependent on μ. This evolution is implemented by requiring that

$$\mu\frac{d}{d\mu}\langle f|\mathcal{H}_{\text{eff}}|i\rangle = 0, \tag{1.47}$$

and solving the Renormalisation Group equations. This requires the calculation of an *anomalous dimension* matrix, γ, such as found in Ref. [58]. This will induce *mixing* between the operators introduced and other $b \to s$ operators[8]. An example of this is shown in Fig. 1.7. These mixing effects are included in the anomalous dimension matrix, however truncation of the perturbative expansions used will

[8] A very extensive review of these issues can be found in Ref. [59].

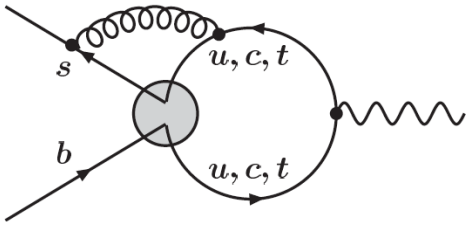

Figure 1.7: An example of operator mixing between $\mathcal{O}_7$ and $\mathcal{O}_2$. $\mathcal{O}_2$ is a four-quark operator defined as e.g. $\mathcal{O}_2 = (\bar{c}_{L,i}\gamma_\mu b_{L,j})(\bar{s}_{L,j}\gamma_\mu c_{L,i})$, mediated by a gluon. In the diagram, a higher order correction to $\mathcal{O}_7$, where an additional gluon loop is included, leads to the embedding of $\mathcal{O}_2$ in $\mathcal{O}_7$. Figures from Ref. [30].

introduce some residual scale dependence that must be included in theoretical uncertainty estimates.

1.3.2 Quantum Chromodynamics and HQET

The strong force is described using the $SU(3)_C$ theory of QCD[9]. This is a locally gauge invariant quantum field theory (QFT) in which the quarks and gluons carry *colour* charge. Physical states must, however, remain colour neutral, leading to the formation of mesons, $q_a\bar{q}^a$, and baryons, $\epsilon^{abc}q_a q_b q_c$. The presence of non-Abelian terms in the QCD field strength tensor, and the size of its running coupling constant, α_s, make perturbative calculations challenging for many processes. The study of approximate symmetries of the QCD Lagrangian is then particularly important, as they allow for calculations to be made outside of the perturbative regime.

The running of α_s naturally leads to a division in QCD between processes operating at short (*hard*) and long (*soft*) ranges. The self-coupling of the gluon fields and the confinement of colour lead to a competition between screening and anti-screening effects. At short ranges, anti-screening effects, from integrating over a spatially separated colour field, do not significantly contribute; a quark can be approximated as a colour point charge. At these ranges, α_s is small and perturbative methods may be used. At longer ranges, when the energy scale is greater than $\sim \Lambda_{\rm QCD}$, anti-screening effects dominate; α_s is large and non-perturbative methods must be used.

In the case of mesons containing a heavy quark, such as a b quark, we may consider the limit where $m_q \to \infty$. Unlike the case where $m_q \to 0$, this is not a formal limit of the QCD Lagrangian and an effective field theory must be constructed which allows for this limit to be explicitly considered. This is the heavy quark effective theory (HQET) [61, 62]. In this limit, the heavy quark is

[9]The following section is based on Refs [34, 35, 60].

stationary in the rest frame of the meson, and provides a central source of colour charge, much like a proton provides electric charge in the hydrogen atom. In this colour potential sits a complex array of light $q\bar{q}$ pairs and gluons, termed *brown muck* by Isgur (e.g. [63]). This sea of coloured objects is non-perturbative, and hard to treat from first principles. The second valence quark (the *light* quark) in the meson couples to the brown muck, rather than directly to the heavy quark, through the emission and absorption of soft gluons; the underlying properties of the heavy quark, such as its flavour, mass and spin, are unimportant. This is analogous to the invariance of the properties of atoms under a change in the isotope being considered; it leads to additional approximate symmetries which may be exploited to simplify calculations [61]. Put exactly, the configuration of the light quark in a meson should remain unchanged if the heavy quark, $Q(s, v)$, with spin s and velocity v, is replaced by another heavy quark, $Q'(s', v)$, with different spin or flavour but the same velocity. This allows, for example, for universal form factors to be calculated which will be valid for any heavy quark coupling to a particular light quark. In reality, the heavy quarks do not have infinite mass and there will be symmetry breaking corrections to this picture; these will be of order $\Lambda_{\mathrm{QCD}}/m_q$ and arise due to the motion of the heavy quark inside the meson.

These approximations are not enough to the treat *heavy-to-light* form factors of interest in this thesis; additional constraints must be introduced. In the case where the energy of the light hadron is large, an additional expansion in powers of $1/E$ can be performed, using large energy effective theory (LEET) [64]. In the limit where $E \to \infty$, the formation of the light hadron is mediated by soft-gluon exchange; hard spectator effects can be neglected. When the light hadron energy is large but finite, the hard spectator effects are suppressed by a factor of $1/E$. This separates the two different regimes, simplifying calculations. The LEET must be modified to include the effects of collinear gluons in order to reproduce the correct infrared behaviour of QCD. This theory is known as soft-collinear effective theory (SCET) and has been used extensively in the theoretical treatment of B decays [65–67].

1.4 $\overline{B}_d \to \overline{K}^{*0}\mu^+\mu^-$

$\overline{B}_d \to \overline{K}^{*0}\mu^+\mu^-$[10] is a FCNC $b \to s$ decay that proceeds via penguin and box diagrams such as those shown in Fig. 1.8.

[10]We deal with the $\overline{B}_d$ as this contains the b quark. The formalism can be applied equally to the B_d with appropriate redefinitions which will be indicated explicitly in the text.

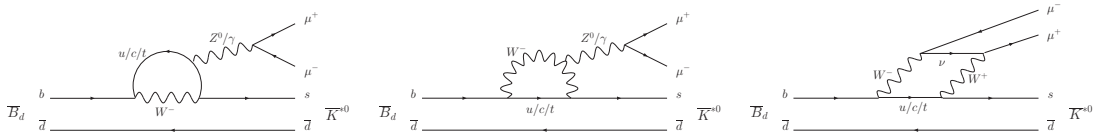

(a) Quark Penguin (b) W Penguin (c) W Box

Figure 1.8: SM Feynman diagrams for the $\overline{B}_d \to \overline{K}^{*0}\mu^+\mu^-$ decay.

It was first observed at BELLE [68] and has a branching ratio of $(1.10^{+\ 0.29}_{-\ 0.26}) \times 10^{-6}$ [41]. The decay is sensitive to NP contributions through the addition of new diagrams where charged or neutral NP particles run in the loop [57, 69–71] and can be described with Eq. (1.38). Studies show that the decay can be selected using the LHCb detector, giving 6200 $^{+1700}_{-1500}$ $\overline{B}_d \to \overline{K}^{*0}\mu^+\mu^-$ signal events with 1550 ± 310 signal-like background events per nominal year of running [72, 73].

As with $\mathcal{B}(b \to s\gamma)$, introduced in Sec. 1.3, $\mathcal{B}(\overline{B}_d \to \overline{K}^{*0}\mu^+\mu^-)$ is sensitive to NP effects; however, the value measured is very compatible with SM predictions[11]. However, as discussed in following chapters of this thesis, the four body final state of $\overline{B}_d \to \overline{K}^{*0}\mu^+\mu^-$ can be used to access *angular observables* with complementary sensitivity to the branching fraction. The kinematics of the decay are introduced in Sec. 3.1, and various angular observables are defined in Sec. 3.4.

Two of these observables, $A_{\rm FB}$ and $F_{\rm L}$, have been measured by *BABAR*, BELLE, and CDF, and are shown in Fig. 1.9 for the kinematic region for which theoretical calculations can be made [75–81]. It can be seen that these measurements are also in good agreement with the SM; however, the clustering of the central values, as well as larger than expected isospin asymmetries, has led to some suggestions that NP effects are present, e.g. Ref. [82]. As shown in Sec. 6.6, speculations of this sort are perhaps premature (see also Ref. [83]). The large increases in signal statistics expected at LHCb should be able to clarify this situation considerably.

[11] In the region where theoretical predictions can be made, Ref. [74] predicts $\mathcal{B}(\overline{B}_d \to \overline{K}^{*0}\mu^+\mu^-)_{1-6\,{\rm GeV}^2} = (1.2 \pm 0.4) \times 10^{-7}$, while the BELLE collaboration measures $(1.49\ ^{+0.45}_{-0.40} \pm 0.12) \times 10^{-7}$ [75].

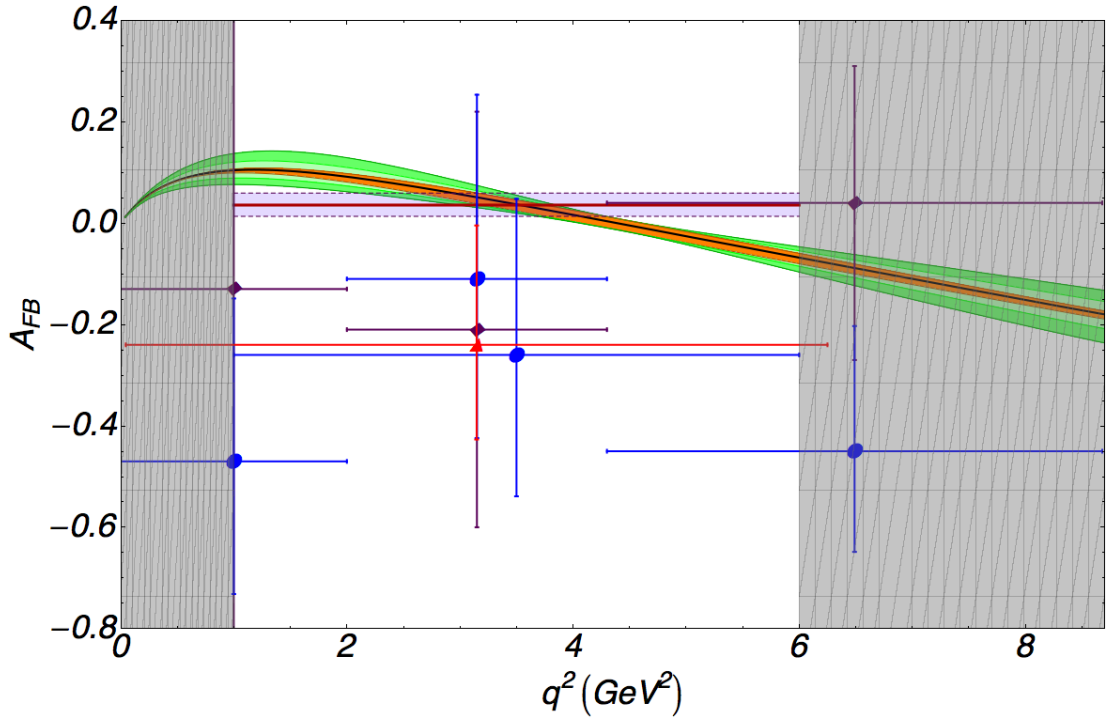

(a)

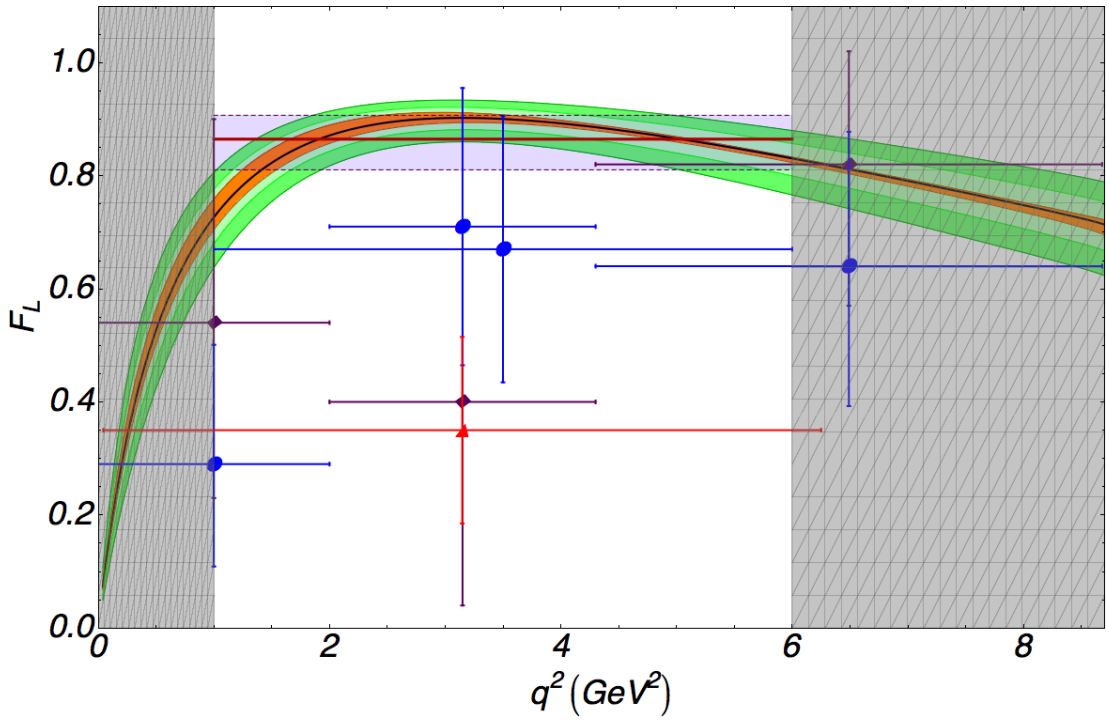

(b)

Figure 1.9: Recent results from *BABAR* (red triangles), Belle (blue circles) and CDF (purple squares) for (a) $A_{\rm FB}$, and (b) $F_{\rm L}$, re-drawn from Ref. [75, 77, 81]. SM theoretical predictions are shown; the orange, light green, and dark green bands show the parametric and estimated 5% and 10% contributions from unknown higher order terms in the $1/m_b$ expansion, known as Λ/m_b corrections [1]. The light purple bands show the rate-weighted SM average in the region $q^2 \in [1\,{\rm GeV}^2, 6\,{\rm GeV}^2]$, with all uncertainties.

Chapter 2

The LHC*b* detector

2.1 The Large Hadron Collider

The Large Hadron Collider (LHC) is a particle accelerator currently being commissioned at the Organisation Européenne pour la Recherche Nucléaire (CERN)[18]. It is designed to collide protons with a center-of-mass energy ($\sqrt{s}$) of 14 TeV and an unprecedented luminosity of $10^{34}\,\mathrm{cm}^{-2}\mathrm{s}^{-1}$. It will also be used to collide heavy ions; for lead nuclei the energy per nucleon is expected to be 2.8 TeV with a peak luminosity of $10^{27}\,\mathrm{cm}^{-2}\mathrm{s}^{-1}$. For protons, $\sqrt{s}$ will be a factor of approximately seven greater than the previous record holder, the TeVatron at Fermilab in Illinois, which collides $p\bar{p}$ at 1.96 TeV.

The LHC is the latest addition to the CERN accelerator complex and makes use of previously installed accelerators. The full chain can be seen in Fig. 2.1. Considering only protons, the beam begins its journey as hydrogen gas that is then ionized and fed into the Linac2. The beam is accelerated to 50 MeV per proton before being injected into the Proton Synchrotron Booster (PSB), which takes its energy to 1.4 GeV. The PSB feeds into the Proton Synchrotron (PS) (25 GeV) from which the protons enter the Super Proton Synchrotron (SPS) (450 GeV) and finally the LHC (7 TeV) via two injection lines, TI2 and TI8. The LHC features two counter-rotating beams that can be brought into collision at interaction points (IPs) around the ring. The beams are accelerated with a system of superconducting radio frequency (RF) cavities, operating at a nominal frequency of 408 MHz. Bending and focusing of the beams is handled using a system of superconducting dipole and quadrupole magnets, along with a large number of smaller beam correcting magnets. A cross-section through a LHC dipole magnet can be seen in Fig. 2.2, where the dual-beam design is visible.

There are four main detectors at the LHC, two of which are general purpose – ATLAS [85] and CMS [86]. These have been designed to probe the high-

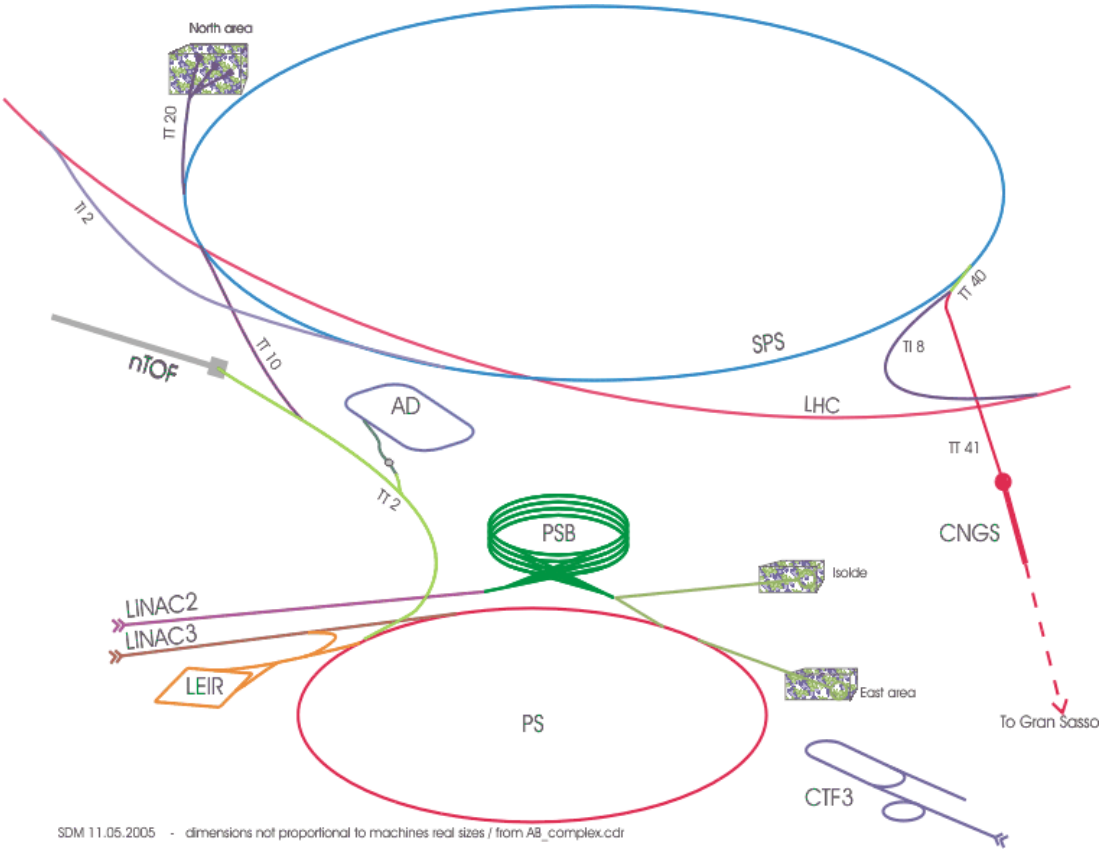

Figure 2.1: The CERN accelerator complex showing the full chain required to inject particles into the LHC [84].

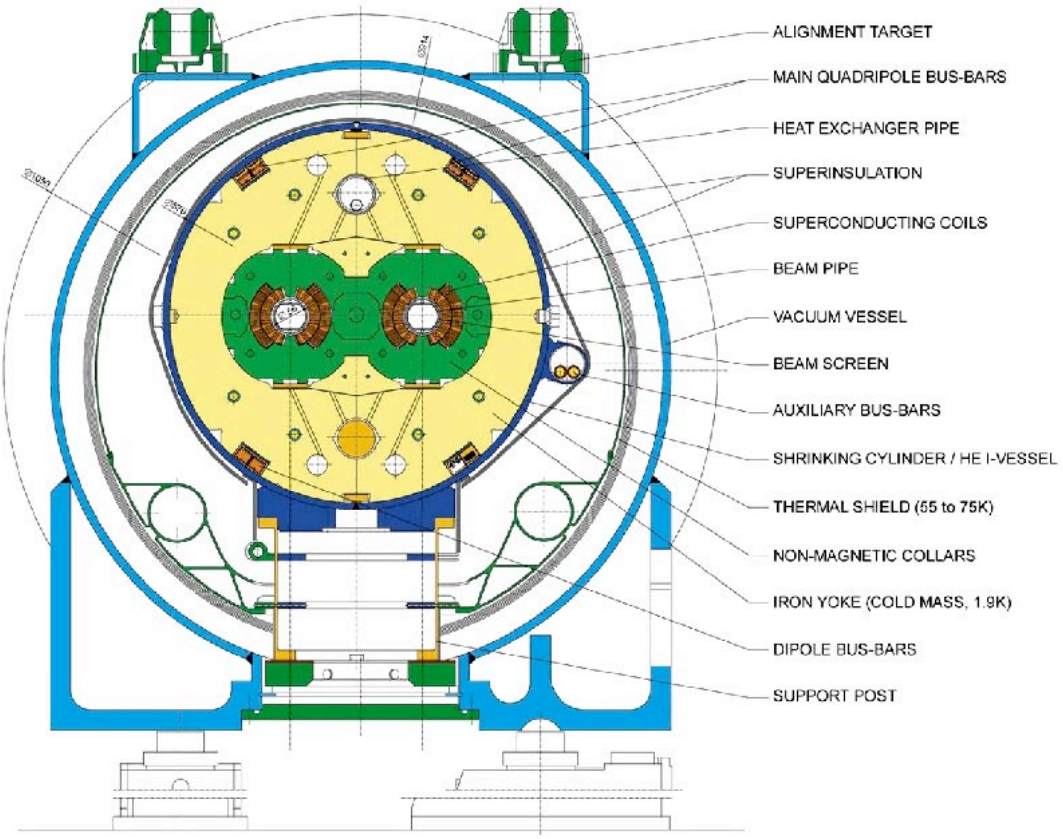

Figure 2.2: A cross-section through an LHC dipole magnet. The two beam pipes can be seen. Fig. from [18]

energy frontier directly and are optimized to select objects with large transverse momentum (p_T). The other two detectors are LHCb, to be discussed in detail in the next section, and ALICE, a heavy ion experiment that aims to study QCD in the asymptotically free regime [87].

At the time of writing[1], the LHC had restarted operation in November 2009, following almost a year of repairs after an abortive 2008 run. The previous energy record for a proton beam was broken on the 29$^{\text{th}}$ of November 2009; some fifty thousand proton-proton collisions were induced at a $\sqrt{s}$ of 2.36 TeV a few weeks later. The machine was then stopped for a short winter shutdown and is scheduled to restart in March 2010. It will then run at 3.5 TeV per beam for 18-24 months before a longer shutdown, required to make the upgrades necessary for 7 TeV per beam operation.

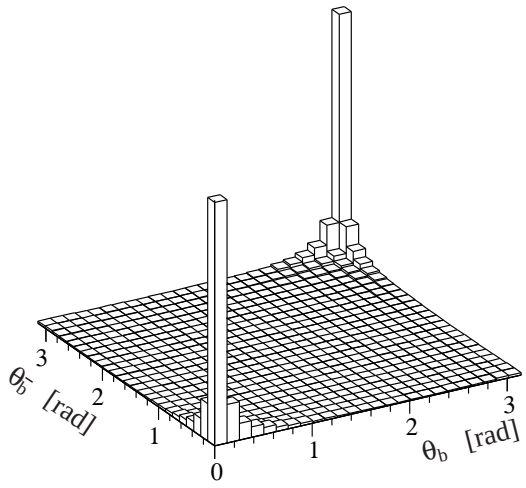

Figure 2.3: Angular correlations in the production of $b\bar{b}$ pairs where $\theta_{b,\bar{b}}$ is the angle defined with respect to the beam axis in the pp centre-of-mass frame. Fig. from [47].

2.2 LHC*b*

LHCb is the experiment at the LHC optimized for the study of CP violation and rare decays in the B meson system [89]. The proposed physics programme requires large data samples and a precision detector in order to study the flavour sector in the high-energy frontier. However, the b-quark production section at 14 TeV will be huge, $\sim 500\,\mu$b, meaning that for a modest luminosity of $2 \times 10^{32}\,\mathrm{cm}^{-2}\mathrm{s}^{-1}$, 10^{12} $b\bar{b}$ pairs should be produced in 10^7 s of running [47]. This corresponds to a nominal year of data-taking. At Leading Order (LO), b quark production at the LHC is via $gg, q\overline{q} \to b\bar{b}$ where the former is dominant. The asymptotic nature of the g and, to a lesser extent, the light quark parton distribution functions (PDFs) mean that the $b\bar{b}$ system is more likely to be produced in the forward direction, due to the kinematical bias introduced by the $b\bar{b}$ mass. Fig. 2.3 shows this angular correlation explicitly. In order to access these $b\bar{b}$ pairs, LHCb has been designed to instrument the forward region with the detector covering from 10 to 300 (250) mrad in the bending (non-bending) plane. A diagram of LHCb is shown in Fig. 2.4a, where the right-handed coordinate system can also be seen. A photograph of the cavern just before the 2009 run is shown in Fig. 2.4b for comparison.

In order to make the best use of the existing Intersection Point 8 (IP8) cavern, which previously housed the DELPHI detector, the IP of the two LHC beams is displaced to one side of the cavern (the right-hand side of Fig. 2.4b) using a modification to the general LHC optics. This allows for a very long detector (~ 20 m) to be installed, from the IP until almost the end of the cavern, as shown

[1]This section was written on the 16$^{\text{th}}$ of February, 2010. Updates can be found in Ref. [88].

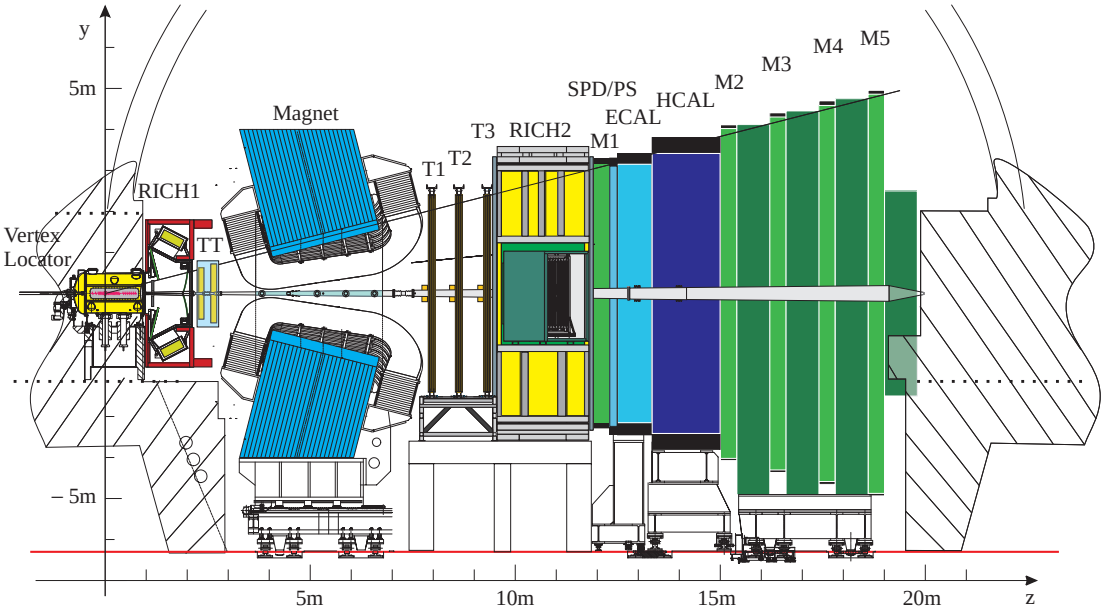

(a) A cross-section of LHC*b*

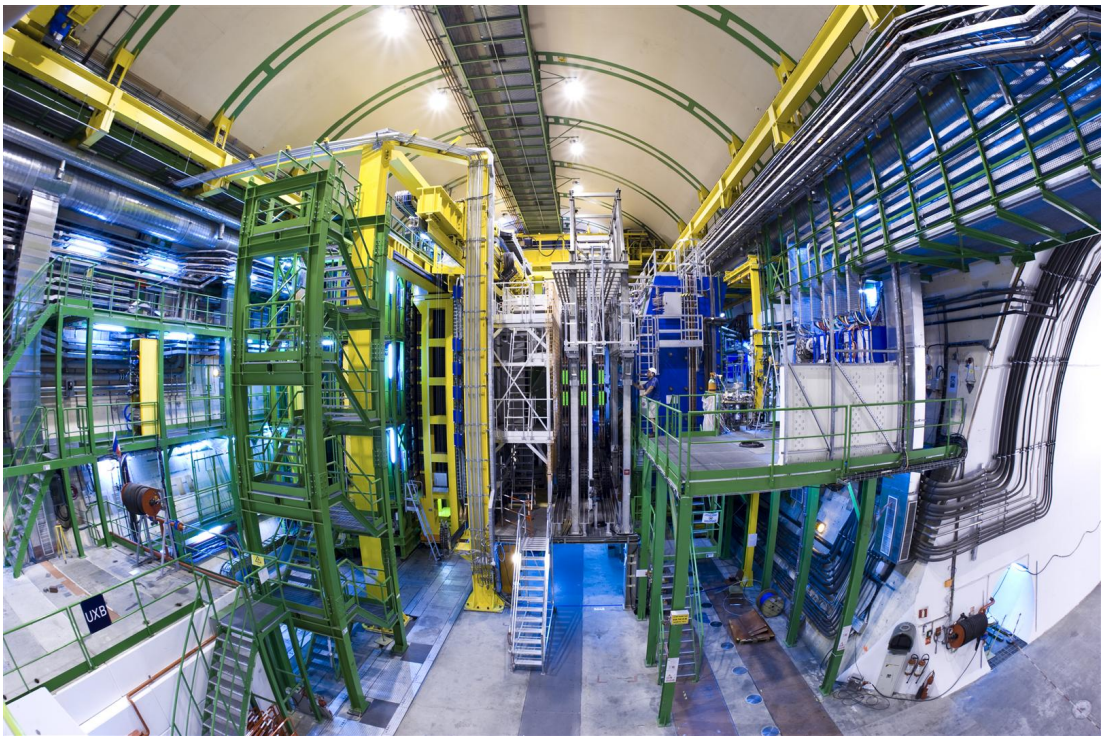

(b) The LHC*b* cavern

Figure 2.4: Fig. (a): A cross-section of the LHC*b* detector, from [89]. The projective layout used for the sub-detectors is illustrated in the diagram. Fig. (b): The LHC*b* cavern in August 2009. The interaction point is at the right edge of the picture; the view is from the opposite side of the detector to that seen in (a).

in Fig. 2.4a. Excellent spatial resolutions can be achieved for tracks, which is of great importance for many B-physics measurements. In order to reduce the material budget, to keep detector services out of the acceptance, and to allow access for maintenance, a slice architecture has been adopted, with sub-detectors separated with empty space where possible. A warm dipole magnet, shown in Fig. 2.4, provides bending in the horizontal plane, allowing for the momentum of charged objects to be found with high precision. A 10 m track will experience an integrated field of 4 Tm over its length.

The forward region will contain a large contribution from soft QCD processes, collinear with the beam direction. Including particle identification (PID) capabilities in the detector will help suppress soft pions and allow the study of final states where the hadron type is important – K, π, and p hadrons should all be distinguishable with high efficiency.

In nominal conditions, it is expected that reconstructible interactions will occur within LHCb at a rate of 10 MHz. This must be reduced to 2 kHz if the detector readout is to be stored and processed effectively. This will require very fast and effective triggering, so that b decays can be selected with high efficiency.

In the following sections, the individual subsystems will be reviewed to illustrate how LHCb is designed to deal with the harsh environment of the LHC. The rare decay $\overline{B}_d \to \overline{K}^{*0}\mu^+\mu^-$ will be used as an example, following the off-line selection given in Refs [72, 90] and the discussion of trigger strategies found in Ref. [8].

2.2.1 The tracking system

The tracking system is very important for LHCb. As discussed in Sec. 1.3, the relatively long lifetime of the B meson combined with the large boosts seen in the forward direction mean that the decay vertex is displaced from the IP by distances of $\mathcal{O}(1\,\text{mm})$. Measuring this displacement via an *impact parameter* allows for the unambiguous tagging of B meson decays and forms an important part of many LHCb selections [8]. Having excellent vertex resolution also allows for particle lifetimes to be measured with high precision.

High tracking efficiency is vital for the success of the experiment. Detector technologies must be chosen that are very sensitive to the passing of charged particles, while keeping the signal-to-noise ratio high; noise hits can generate ghost tracks which obscure the physics processes of interest.

The off-line selection of $\overline{B}_d \to \overline{K}^{*0}\mu^+\mu^-$ makes very tight requirements on the quality of the B vertex as well as the individual $K\pi$ and $\mu\mu$ vertices. The B vertex is also required to be significantly displaced from the interaction point. The decay

features four charged tracks that are found by fitting a smoothly varying line to the collection of detector hits. The quality of each track in this fit is also required to be good. These quantities can be used to select the decay without biasing the angular distribution, and so particularly stringent requirements are made [8].

The Vertex Locator

The Vertex Locator (VELO) detector is a silicon vertex detector, responsible for providing high precision tracking information close to the primary IP. The active area of the detector is made up of twenty-one discs of silicon, each divided into two equal and partially overlapping segments. These segments are held in a vacuum tank mounted at the LHC interaction point (see Fig. 2.4a), and separated from the LHC beam by 200 μm thick corrugated aluminium foil. They are parted while the LHC beams are injected into the machine and then brought together once stable conditions have been reached. This allows for the sensors to be placed only 8 mm away from the beam axis providing the best possible resolution for vertex position measurements by reducing the distances over which tracks must be extrapolated. The harsh radiation environment at this distance means that the silicon technology used must be extremely radiation hard if detector performance is to be sustained over many years; the modules are held at a temperature between -10° and 0° to slow ageing. The individual segments follow an $R-\phi$ layout, shown in Fig. 2.5a: the R strips are laid out in concentric semi-circles centring on the beam axis; these are sub-divided into 45° segments to reduce capacitance. The ϕ sensors are implanted on the other face of the segment, and laid out radially so that position information on silicon hits anywhere in the disc can be found by combining the two faces. The segments are aligned so that segment faces of the same type face one another, but with a relative offset in direction of the ϕ sensors to improve stereo resolution. This *stereo angle* is shown in Fig. 2.5a. A picture of the lower segments, mounted in the VELO vacuum tank, can be seen in Fig. 2.5b.

There are a further two sensors mounted upstream of the beam collision point, known as the *pile-up veto* system. As LHCb is intended for making precision measurements, the design luminosity is significantly reduced, compared to the LHC design luminosity, by focusing the beams relatively less before collision than for the other LHC experiments. At this luminosity, most beam crossings will have zero or one proton-proton interactions, however some events will have more than this. As discussed in Sec. 2.2.5, beam crossings with multiple interactions can be vetoed in the Level-0 (L$\emptyset$) trigger; these events will be rejected with 80% efficiency while correctly accepting 95% of single interaction events.

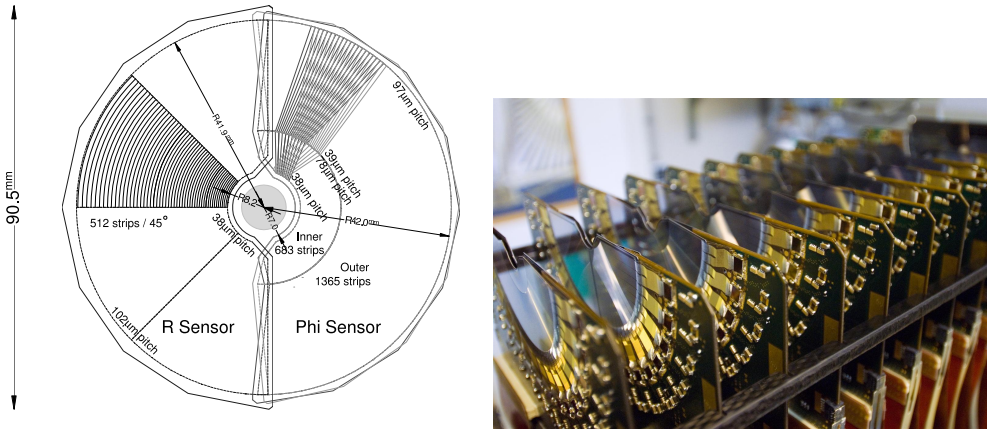

(a) The $R - \phi$ geometry (b) VELO modules

Figure 2.5: The VELO detector [89].

The Silicon Tracker

The Silicon Tracker (ST) is made up of two sub-detectors, the Tracker Turicensis (TT) and the Inner Tracker (IT).

The Tracker Turicensis The TT is 150 cm wide and 130 cm high. It is located upstream of the LHC*b* dipole magnet and covers the full acceptance of the experiment, as shown in Fig. 2.4a. It is made up of four layers of silicon micro-strip detector with the first and third layers rotated by a stereo angle of 5°. The detector has an active area of 8.4 m^2 with 143360 readout strips of up to 38 cm in length. Each layer is made of overlapping tiles with the required cooling and readout electronics located outside of the active area. The TT is positioned to provide hit information between the RICH1 detector and the magnet while keeping the material budget to a minimum.

The Inner Tracker The IT covers a 120 cm by 40 cm region in the centre of the three tracking stations, T1, T2, and T3. As shown in Fig. 2.4a, it is positioned downstream of the magnet. The same silicon micro-strip technology is used as the TT to provide 50 μm spatial resolutions in the central region, which will have the highest occupancies. These resolutions are required throughout the ST so that the track momentum resolution is dominated by multiple scattering effects over the majority of particle momentum ranges. The IT has an active area of 4.0 m^2 with 129024 readout strips of either 11 cm or 22 cm in length. In both the TT and the IT, the strip lengths were chosen to keep occupancies to a few percent while minimizing the number of readout channels required.

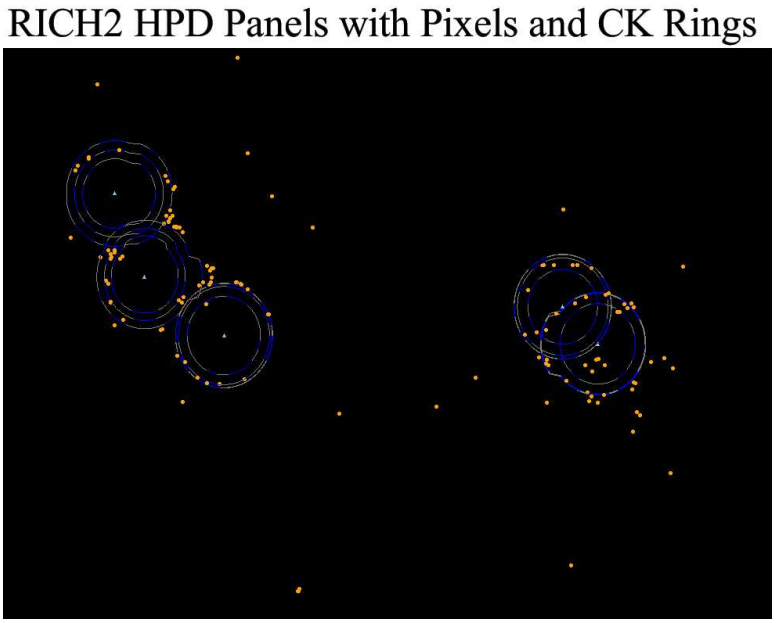

Figure 2.6: CF_4 rings in RICH 2, produced during proton-proton collisions at 450 GeV per beam on the 6$^{\text{th}}$ of December 2009 [91].

The Outer Tracker

The final pieces of the tracking system are provided by the Outer Tracker (OT), marked as T1, T2, and T3 in Fig. 2.4a. This covers the areas in these tracking stations, further away from the beam pipe, that are not within the acceptance of the IT. The three tracking stations are located after the magnet, and so of particular importance for making precision momentum measurements. The active regions are made from gas-tight straws containing Argon (70%) and CO_2 (30%), providing drift times of below 50 ns while keeping drift-coordinate resolutions at about 200 μm. Each tracking station is made up of four layers of straws making a total active area of $5971 \times 4850\,\text{mm}^2$ per station. The straws in the first and fourth layers are orientated vertically, with the second and third offset by $\pm 5^\circ$ with respect to the vertical. The relative areas of IT and OT were chosen so that the occupancy of the OT is always less than 10% per straw.

2.2.2 The particle identification system

PID is very important at LHCb. The background in the forward direction will be dominated by soft pions from collinear QCD effects. While these can often be removed with momentum cuts, this can be problematic for measurements of the $\overline{B}_d \to \overline{K}^{*0}\mu^+\mu^-$ angular distribution, where they produce systematic distortion effects. The two Ring-Imaging Čerenkov (RICH) detectors are used to separate kaons and pions, which will be useful e.g. for the study of charmless B decays, as described in Ref. [8], and for some of the measurements studied in this thesis.

RICH1

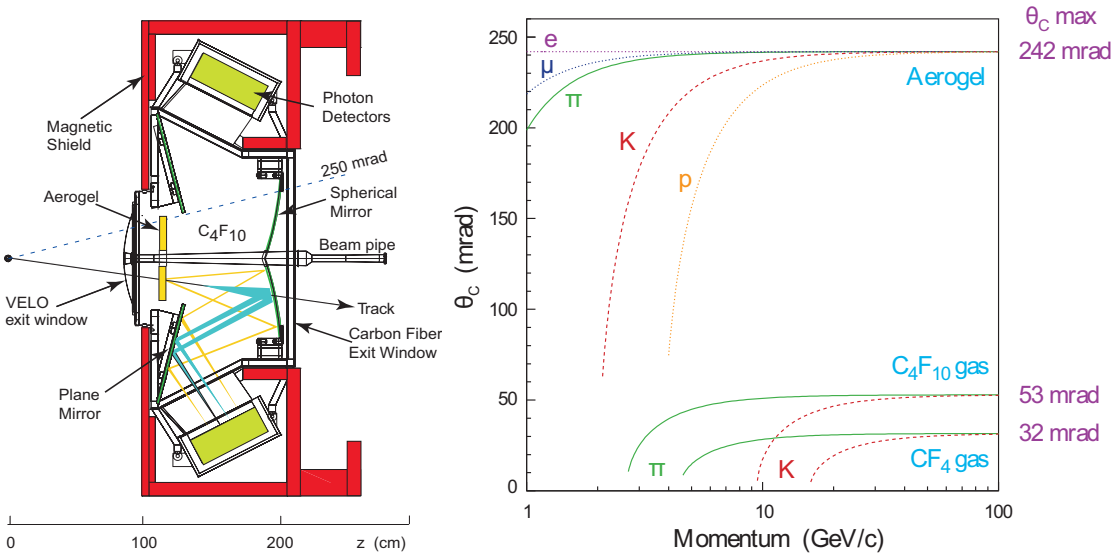

(a) The RICH1 geometry (b) RICH Radiators

Figure 2.7: The geometry and construction of RICH1 and the momentum dependence of the Čherenkov radiators used [89].

The RICH1 detector sits in between the VELO and the TT in an iron box that shields its sensitive Hybrid Photon Detectors (HPDs) from the magnetic field. Its position can be seen in Fig. 2.4a, and a schematic diagram of its layout is shown in Fig. 2.7a. It uses both aerogel and C_4F_{10} as Čherenkov radiators and then focuses the light produced on a close-packed array of 196 HPDs using a system of flat and spherical mirrors. As a particle passes through the radiator, light is emitted by the material at an acute angle, θ_c, to the particle's direction of travel. This light forms a cone, producing a ring such as those shown in Fig. 2.6 when it is projected onto the HPD plane. For a given radiator, θ_c is a function of the momentum of the particle travelling through the medium and its type; this is illustrated in Fig. 2.7b. By combining information from the tracking system with the radius of the ring seen, an identification of the particle type can be made. Several radiators are used so that the entire range of particle momenta is covered. The necessity of this can again be seen in Fig. 2.7b.

RICH2

The RICH2 detector is significantly larger than RICH1, and is located between the last of the tracking stations and the first muon station. It uses CF_4 gas as a radiator to provide PID for particles with momenta from 15 to 150 GeV. The momentum dependence of the Čherenkov angle for this gas is shown in Fig. 2.7b. The detector again uses a system of large flat and spherical glass mirrors to focus

the Čherenkov light on to an array of 288 HPDs. The support box is built to keep the HPDs and all the support structure outside of the detector acceptance. An example of rings found during 900 GeV proton-proton collisions is shown in Fig. 2.6. The individual pixel hits can be seen, as can the ring centre as found from the tracking system.

2.2.3 Calorimetry

The calorimetry system of LHC*b* consists of the three sub-detectors: the scintillator-pad detector/pre-shower (SPD/PS); an electromagnetic calorimeter (ECAL); and an hadronic calorimeter (HCAL). Together these detectors perform several functions. They can be used to detect high transverse energy (E_T) objects for the trigger. This can be done fast enough for them to enter at L$\emptyset$. They provide identification of electrons, photons, and hadrons and will help measure their position and energies. These detectors are not heavily used in the selection of $\overline{B}_d \to \overline{K}^{*0}\mu^+\mu^-$, where the majority of events are triggered at L$\emptyset$ in the muon lines; however they will be essential for studying other rare decays such as $B_s \to \phi\gamma$.

The technology used in all three detectors is similar; they are sampling calorimeters featuring lead plates separated by sheets of plastic scintillator. If a shower forms, the energy of any ionizing particles is deposited in the scintillator and re-emitted as light. This is then transmitted to photomultiplier tubes (PMTs) outside the detector acceptance. The intensity of the light output gives a measure of the real deposited energy once careful calibrations have been made.

The SPD/PS

The SPD/PS detector provides pre-shower information before particles enter the ECAL. It consists of a 15 mm (2.5 X_0) thick plate of lead sandwiched in between two high granularity planes of segmented scintillator. The segments are arranged to correspond with those of the ECAL; a total of 12032 read-out channels are employed. The detectors main purpose is to provide a π^0 veto for the electron and photon identification algorithms used with the ECAL.

The electromagnetic calorimeter

The ECAL is responsible for identifying events which contain high-E_T objects for the L$\emptyset$ trigger, as well as providing energy deposition and location information for later analysis. The detector has enough energy resolution to give a B mass resolution on photon penguin decays like $B_s \to \phi\gamma$ of 65 MeV. It is segmented into modules: each is made up of alternating layers of 2 mm thick lead plates, 120 μm thick reflecting paper and 4 mm thick compressed polystyrene scintillating tiles.

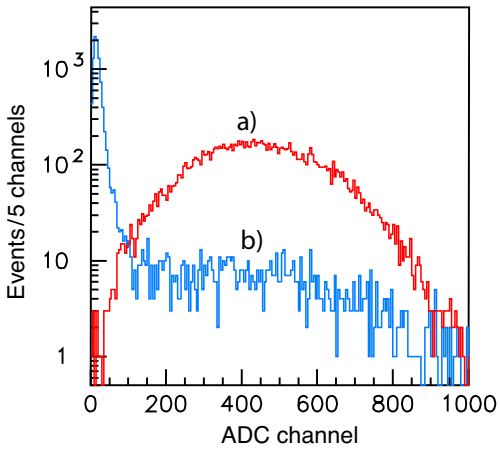

Figure 2.8: Energy deposition of a ECAL module in (a) 50 GeV electrons and (b) pions, produced by the PS.

A total of sixty-six layers are used giving a combined thickness of 42 cm (25 X_0). Electrons and pions can be distinguished by looking at the profile of the shower as it progresses; the differing detector responses are shown from test beam data in Fig. 2.8.

The hadronic calorimeter

The HCAL is a sampling calorimeter, made up of alternating layers of scintillating tiles and iron plates. Hadrons passing though the iron plates interact with the material, producing a shower of charged particles that then induce light to be radiated in the scintillator. This light is collected with optical fibres and read out with PMTs located outside of the detector acceptance. The detector is segmented into square cells with 131.3 mm length sides in the inner section of the detector and 262.6 mm in the outer section. Information from the HCAL is available to the L$\emptyset$ trigger in order to identify events containing high-E_T hadrons.

2.2.4 The muon system

The study of decays with muons in the final state is key for many measurements at LHCb [8]. Muons also play an important part in the LHCb triggering and flavour tagging strategies. There are five muon stations, M1-M5, placed from before the SPD/PS system to the cavern wall. Their positions may be seen in Fig. 2.9 (left). M2-M5 are separated by 80 cm thick blocks of iron absorber that stop the majority of particles before they reach M5. In order to select highly-penetrating muons, hits are required in all five muon stations by the LHCb reconstruction algorithms; the minimum momentum for a muon to traverse the entire system is about 6 GeV/c. Muons with momenta down to 3 GeV/c can be

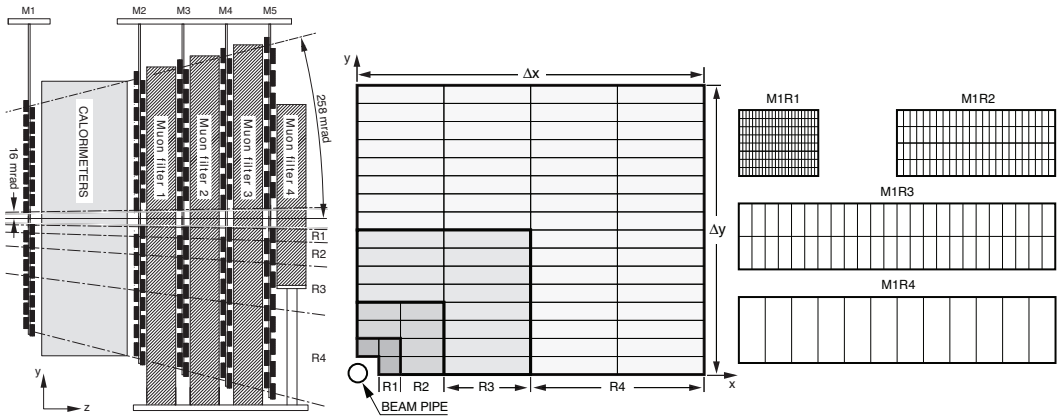

Figure 2.9: The layout of the LHCb muon system.

found by reducing the required number of stations hit. These low-momentum muons are important in the selection of $\overline{B}_d \to \overline{K}^{*0}\mu^+\mu^-$, as the systematic failure to reconstruct events with one hard and one soft muon leads to a distortion of the full-angular distribution [8]. An example of a proton-proton collision containing at least one muon can be seen in Fig. 2.10; the associated tracks are shown in green.

Each muon station is split into regions, shown in Fig. 2.9 (left). Each region is then segmented into *logical pads*, which provide binary hit information to the L$\emptyset$ trigger. The granularity of the segments decreases from region one to region five to maintain a constant occupancy, as shown in Fig. 2.9 (centre and right). M1-M3 have high spatial resolutions in the bending plane, and provide the track direction and momentum resolution. M4 and M5 are much more coarsely segmented, and are mainly for identifying penetrating particles. MWPCs are used for all segments apart from R1 of M1, where gas electron multiplier (GEM) detectors are instead used due to their superior radiation hardness and granularity. These detector technologies provide the very high efficiencies and fast response times required for a five-coincidence (i.e. ϵ^5) trigger operating at 40 MHz. The off-line muon identification efficiency is expected to be better than ninety percent for a few percent mis-identification rate over a large range of muon momenta, from 3-200 GeV/c [92, 93].

2.2.5 The trigger

Building an efficient trigger is of utmost importance in a hadronic environment. The huge data rates available at the LHC will make the filtering of interesting events essential. The LHC bunch-crossing rate is 40 MHz. The lower operating luminosity of $2 \times 10^{32}\,\mathrm{cm}^{-2}\mathrm{s}^{-1}$ chosen for LHCb means that the actual rate of events which contain at least one collision visible in the detector should be about

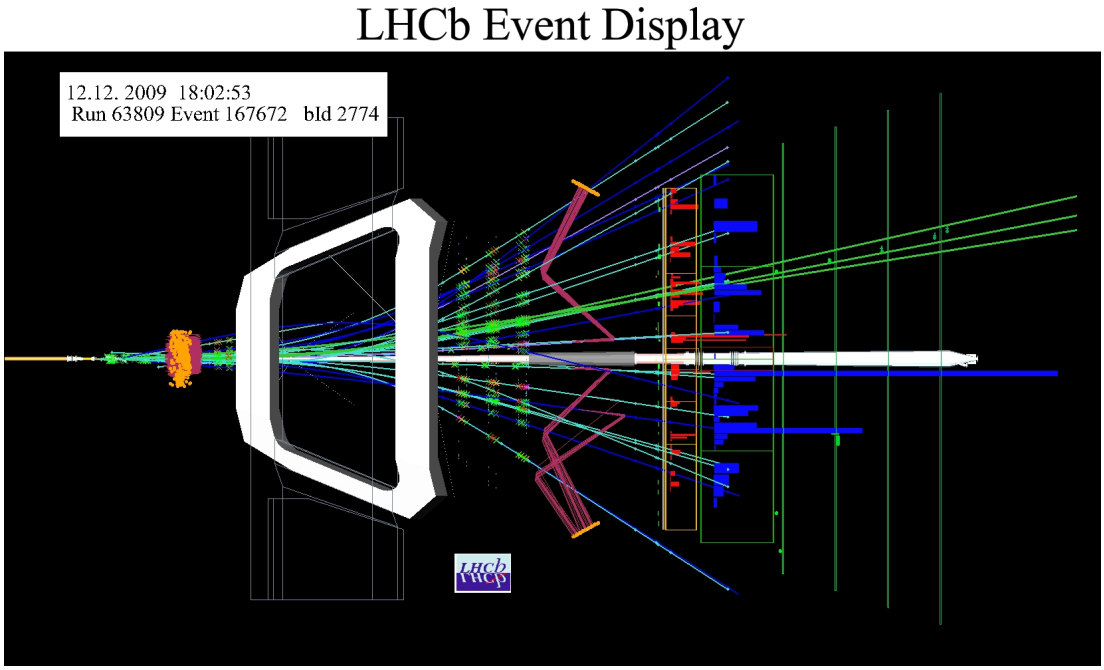

Figure 2.10: A proton-proton collision at 450 GeV per beam recorded during stable LHC running on the 12$^{\text{th}}$ of December 2009. A large number of particles are seen, including three muons tracks (shown in green) [91].

10 MHz; about one percent of these will contain a $b\bar{b}$ pair. This gives a $b\bar{b}$ rate of about 100 kHz, however, only fifteen percent of these pairs will produce at least one B meson with its decay products in the detector acceptance. The rate of B decays that can be analysed should then be about 15 kHz.

The LHCb computing model allows for a final data rate from the detector of 2 kHz, which will be stored and processed off-line. This rate is very high compared to the general purpose detectors at the LHC [85, 86] and is made possible by the relatively small number of read-out channels in LHCb (leading to small data files, $\mathcal{O}$(40kb) per event). To make the final reduction from 15 kHz to 2 kHz, the most interesting events must be selected from those which are poorly reconstructed or unlikely to be of physics interest. The level to which this is possible will directly affect the statistical uncertainties available for the physics observables under study at LHCb. However, throwing away events that *were* of physics interest risks that new discoveries are missed. This is the nightmare scenario at the LHC.

The LHCb trigger is made up of two basic levels: a L$\emptyset$ trigger implemented in hardware that runs synchronously with the machine, and a software High-Level Trigger (HLT) that runs asynchronously on a dedicated computing farm. The basic structure and inputs to the trigger are shown in Fig. 2.11a. The L$\emptyset$ trigger must be very fast to throw events away while still maintaining high efficiency for signal events. The HLT should confirm the L$\emptyset$ decision once the full detector

Level-0 Line	Signal Selection Efficiency (%)	Rate (kHz)
Single muon	89.9 ± 0.2	230
Di-muon	62.9 ± 0.3	40
Hadron	27.0 ± 0.3	720
Total	93.1 ± 0.2	$\sim$1000

Table 2.1: Estimated Level-0 efficiencies and rates for $\overline{B}_d \to \overline{K}^{*0}\mu^+\mu^-$. The efficiencies shown are relative to off-line selected signal events [8].

readout is available and then filter out those events which are most likely to be of physics interest.

Level 0

The architecture of the L$\emptyset$ trigger is shown in Fig. 2.11b. Due to the large mass of the B meson, the decay products often feature high-p_T and E_T objects that can be identified via the calorimeter and muon systems. These are described in Secs 2.2.3 and 2.2.4 respectively. The L$\emptyset$ trigger attempts to find the largest E_T hadron, electron, and photon clusters in the calorimeters, and the two highest p_T candidates in the muon system. Events with multiple interactions in the same bunch-crossing can be vetoed with the pile-up system. The trigger is made up of three sub-systems, described below, that are then combined in the L$\emptyset$ decision unit with the OR logical operation.

For $\overline{B}_d \to \overline{K}^{*0}\mu^+\mu^-$, the majority of signal events come through the single and di-muon lines at L$\emptyset$. However, a non-negligible fraction are from the hadronic trigger also, due to the $\overline{K}^{*0}$ decay. A summary of the L$\emptyset$ efficiencies for $\overline{B}_d \to \overline{K}^{*0}\mu^+\mu^-$ is shown in Tab. 2.1.

The calorimeter trigger The calorimeter trigger looks for high E_T hadrons, electrons, or photons. It forms clusters by considering 2×2 cells, and then selecting the clusters with the largest E_T. Simple PID is achieved by considering whether clusters appear in the SPD/PS, ECAL, or the HCAL. The E_T of all HCAL cells is summed in order to reject events outside the detector acceptance and muons from LHC beam halo interactions. A hierarchical structure is adopted where neighbouring sections of the calorimeter are read out and the highest E_T clusters in each section found using twenty-eight custom validation cards, located close to the detector. Each card takes eight input-channels from the three detectors and finds the highest E_T electron, photon, and hadron. The output from these cards are then fed into the L$\emptyset$ decision unit, where $E_T > 3.5\,\text{GeV}$ in the HCAL gives a hadron trigger, and $E_T > 3.5\,\text{GeV}$ in the ECAL gives a photon or

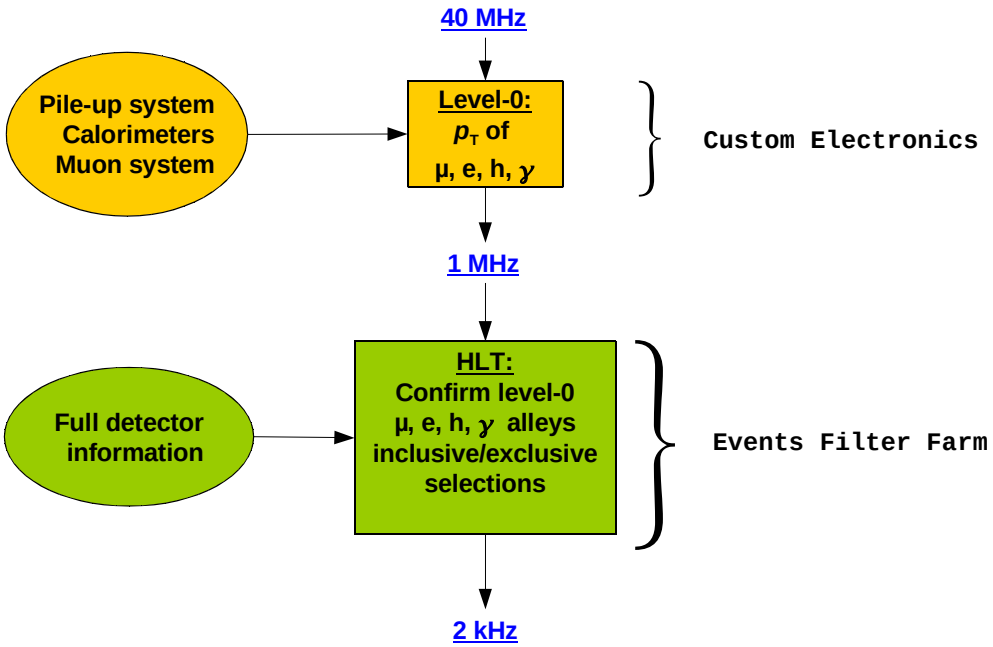

(a) Overview of the LHCb trigger

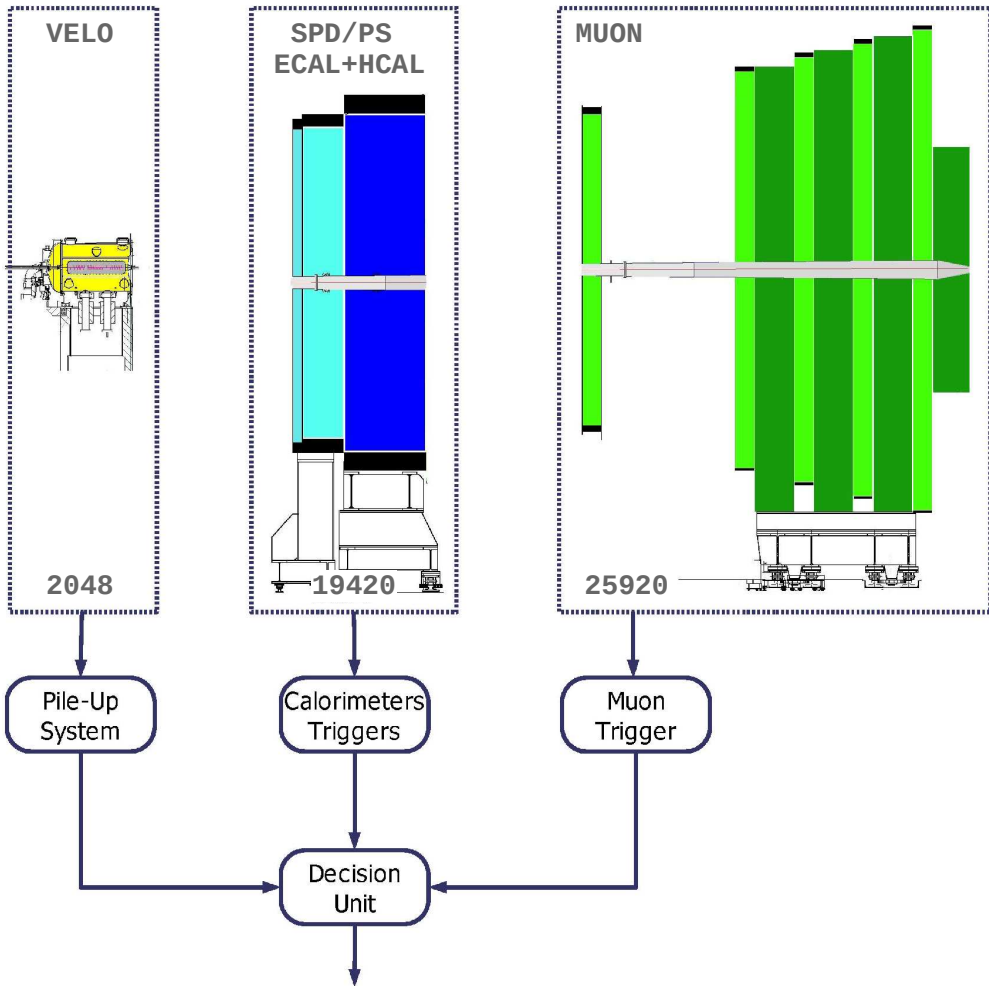

(b) The L∅ trigger architecture

Figure 2.11: The LHCb trigger: (a) shows the overall architecture while (b) shows the inputs used in the L∅ trigger.

electron trigger, depending on the hits seen in the SPD/PS.

The muon trigger The muon trigger uses stand-alone tracking from the muon system to produce p_T estimates with a resolution of $\sim 20\%$. The two highest p_T muon candidates in the detector are then selected. Straight-line track finding is used by combining hits in the five muon stations to form vectors pointing towards the interaction point, starting from seed hits in M3. Hits in the other muon stations are then added to the track until there are five points lying on an approximately straight line. The track is marked as a muon track for further use and the p_T measured.

As described in Sec. 2.2.4, each muon station is subdivided into regions, R1-R4, which are then subdivided into towers (forty-eight per quadrant), spread over the five stations. The output from each tower is read into a processing element. In order to deal with the borders between towers, fast communication between neighbouring elements is essential. Each processing element is able to run up to ninety-six track-finding algorithms in parallel – one for every M3 seed within the tower. This massively parallel architecture is made possible by the use of large field-programmable gate arrays (FPGAs), which allow many copies of the same algorithm to be implemented in low-level logic. The processing elements for nearby parts of the detector are collected in groups of four on a processing board. A fifth FPGA selects the two highest p_T tracks from the board, which are then passed to a chain of controller boards that finally find the two highest p_T muon tracks in the detector. These are used in the L$\emptyset$ decision unit, giving the single and di-muon trigger channels. The current configuration triggers for muon candidates with $p_T > 1.5\,\mathrm{GeV}/c$ (single-muon) or $|{p_T}^1| + |{p_T}^2| > 1.5\,\mathrm{GeV}/c$ (di-muon) [94].

The pile-up system This consists of two R-geometry discs before the VELO (see Sec. 2.2.1 and Fig. 2.5a) to measure the radial distance of hits from the beam line. As the magnetic field at this point in the detector is negligible, coincident pairs of hits in the two discs can be used to find the position on the z-axis (shown in Fig. 2.4a) from where the track originated. Due to radiation hardness requirements, the sensitive areas are formed in strips, which give coverage to a 45° arc in the $x - y$ plane. As many pairs of hits are produced, their corresponding z-axis co-ordinates can be histogrammed; each primary interaction point will produce multiple tracks and so a peak in the histogram. Bunch-crossings with multiple interactions will produce multiple peaks in this histogram and can be vetoed. This is primarily of use for the hadronic trigger lines; the veto is currently not included in the muon trigger.

The High-Level Trigger

The HLT is implemented in C++, and runs on a dedicated computing cluster (the event filtering farm), located underground at IP8. It is designed to use the full detector readout progressively so that events may be discarded quickly. It is subdivided into two levels – HLT1 and HLT2. Each trigger is made up of multiple alleys, the function of which will be detailed below. As the HLT is software based, its algorithms and architecture may be refined as experience with the LHC environment is gained.

HLT1 The objects in the detector that led to the L∅ trigger are used as seeds for a partial reconstruction of the event. Hits in the tracking stations and VELO are matched to the L∅ track in order to improve the p_T resolution and add impact parameter information. Secondary vertexes are also identified, so that loose invariant mass constraints can be applied. The main trigger alleys are[2]:

- **Hadron:** The L∅ hadron candidate is confirmed if its p_T it greater than $2.5\,\mathrm{GeV}/c$ and its impact parameter is above $150\,\mu$m. The candidate can also be accepted if a secondary vertex is found along with a track [95].

- **Muon:** The L∅ muon and di-muon candidates are confirmed in a similar way to the hadrons. Single muons tracks are accepted if they have an impact parameter of 8 mm or greater and a p_T greater than $1.3\,\mathrm{GeV/c}$. Candidates with $p_T > 6\,\mathrm{GeV}/c$ are accepted without the impact parameter requirement. Di-muon candidates are confirmed if the distance of closest approach between the two muon tracks is less than 0.5 mm and $M_{\mu\mu} > 2.5\,\mathrm{GeV}/c^2$ or they have an impact parameter greater than 0.15 mm and $M_{\mu\mu} > 0.5\,\mathrm{GeV}/c^2$ [96].

- **Muon + track:** The L∅ confirmed muon candidate is required to form a vertex with another track; the combined invariant mass must be greater than $0.8\,\mathrm{GeV}/c^2$. In addition, we require $p_T(\mu, \mathrm{track}) > (1, 0.8)\,\mathrm{GeV}/c$ and $\mathrm{IP}(\mu, track) > (25, 50)\,\mu$m [97]. This alley is the most efficient for triggering $\overline{B}_d \to \overline{K}^{*0}\mu^+\mu^-$ events; a selection efficiency of $87.2 \pm 0.2\%$ relative to off-line and L∅ selected events is expected [8].

- **Electromagnetic:** Electron and photon candidates are confirmed by considering clustering in the ECAL and then vetoing merged π^0s using shower shape variables. Tracking from the VELO is used to identify at least one

[2]The cuts presented in this section are particularly liable to change as the LHCb trigger is commissioned. They are intended to be representative, however, different strategies are used in different regions of phase space.

track with impact parameter greater than 0.15 mm and p_T greater than 2.8 GeV/c [98]. This trigger line has been carefully optimized so that $b \to s\gamma$ decays can be identified.

It is envisaged that there will be also be a small number of inclusive HLT1 selections to identify, for example, D^*, $D_s^{\pm}$ and ϕ decays.

HLT2 The HLT2 uses the full detector readout and event reconstruction to analyse events. In addition to many exclusive selections implemented with custom algorithms, there are inclusive algorithms such as:

- **Topological:** This attempts to identify the decays of b and c quarks by looking for displaced vertexes and by making constraints on the invariant mass of the system.

- **Leptonic:** The single-muon, di-muon and muon+track triggers found in HLT1 are all present. The improved mass, impact parameter, and momentum resolutions means that more stringent constraints can be used to reduce the rates from background events. For $\overline{B}_d \to \overline{K}^{*0}\mu^+\mu^-$, the muon+track alley dominates as in HLT1. The overall trigger efficiency is expected to be about 87%, once all of the contributing lines have been combined.

2.2.6 Detector summary

Performing B-physics measurements at the LHC will be challenging. The LHCb detector has been carefully designed to give excellent mass, momentum, and vertex resolutions, which will be essential for identifying events B decays with charged tracks in the final state. The detector also features dedicated calorimetry and PID to enable complex final states to be disentangled. The general design of the detector has been reviewed with emphasis on the selection of the rare decay $\overline{B}_d \to \overline{K}^{*0}\mu^+\mu^-$. The overall selection efficiency for this decay is expected to be about one percent [8], meaning that many thousands of signal events will be selected each year. Commissioning of the detector is currently taking place; the author looks forward to the first publications analysing proton-proton collision data at the LHC from LHCb.

Chapter 3

The full-angular distribution of $\overline{B}_d \to \overline{K}^{*0}\mu^+\mu^-$

3.1 Angular distribution

We assume that the $\overline{K}^{*0}$ always decays on its mass shell to a K^- and a π^+, explicitly ignoring any non-resonant $\overline{B}_d \to K^-\pi^+\mu^+\mu^-$ contributions[1]. In this approximation, known as the *narrow width* approximation, the decay is completely kinematically constrained by three decay angles, θ_ℓ, θ_{K^*}, and ϕ, and by the invariant mass of the muon pair, q^2. This allows for a manifestly covariant expansion to be made, see Eqs 3.12-3.14, while still explicitly conserving energy and momentum. The angles are defined in the intervals

$$0 \leq \theta_\ell \leq \pi\,, \quad 0 \leq \theta_{K^*} \leq \pi\,, \quad -\pi \leq \phi < \pi\,, \tag{3.1}$$

where only the ϕ angle is signed. The decay kinematics are shown in Fig. 3.1 and the definitions of the angles are given in the caption. We can derive a simplified differential decay width for the $\overline{B}_d$, where a sum over final state particle spins has been included. The distribution for the $\overline{B}_d$ is

$$\frac{d^4\Gamma_{\overline{B}_d}}{dq^2\, d\theta_\ell\, d\theta_{K^*}\, d\phi} = \frac{9}{32\pi} I(q^2, \theta_\ell, \theta_{K^*}, \phi) \sin\theta_\ell \sin\theta_{K^*}\,, \tag{3.2}$$

[1]The size of these non-resonant contributions is currently unknown, but expected to be small. These contributions will affect the angular distribution, as it no-longer fully Pseudoscalar→ VectorVector, but may give additional NP sensitivity [99].

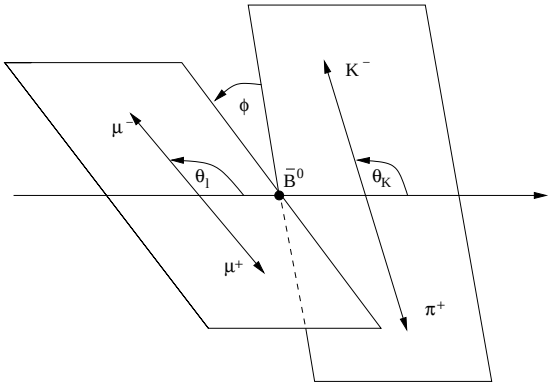

Figure 3.1: The angles used to describe the decay $\overline{B}_d \to \overline{K}^{*0}\mu^+\mu^-$. The z-axis is the direction in which the $\overline{B}$ meson flies in the rest frame of the $\mu^+\mu^-$. θ_ℓ is the angle between the μ^- and the z-axis in the $\mu^+\mu^-$ rest frame, θ_{K^*} is the angle between the K^- and the z-axis in the $\overline{K}^*$ rest frame, and ϕ is the angle between the normals to the $\mu^+\mu^-$ and $K\pi$ decay planes in the $\overline{B}$ rest frame. For the B, the angles θ_ℓ and θ_{K^*} are defined relative to the μ^+ and K^+ respectively.

where the physical region of phase space is $4m_l^2 \leq q^2 \leq (m_B - m_{K^*})^2$ and

$$\begin{aligned} I(q^2, \theta_\ell, \theta_{K^*}, \phi) = \; & I_1^s \sin^2\theta_{K^*} + I_1^c \cos^2\theta_{K^*} + \left(I_2^s \sin^2\theta_{K^*} + I_2^c \cos^2\theta_{K^*}\right)\cos 2\theta_\ell \\ & + I_3 \sin^2\theta_{K^*}\sin^2\theta_\ell \cos 2\phi + I_4 \sin 2\theta_{K^*}\sin 2\theta_\ell \cos\phi \\ & + I_5 \sin 2\theta_{K^*}\sin\theta_\ell \cos\phi + I_6^s \sin^2\theta_{K^*} \\ & + I_7 \sin 2\theta_{K^*}\sin\theta_\ell \sin\phi + I_8 \sin 2\theta_{K^*}\sin 2\theta_\ell \sin\phi \\ & + I_9 \sin^2\theta_{K^*}\sin^2\theta_\ell \sin 2\phi. \end{aligned} \tag{3.3}$$

For the B_d

$$\frac{d^4\Gamma_{B_d}}{dq^2\, d\theta_\ell\, d\theta_{K^*}\, d\phi} = \frac{9}{32\pi}\overline{I}(q^2, \theta_\ell, \theta_{K^*}, \phi)\sin\theta_\ell \sin\theta_{K^*}\,, \tag{3.4}$$

and if CP conservation is assumed, we have

$$I_{1,2,3,4,6,7} = \overline{I}_{1,2,3,4,6,7}\,, \tag{3.5a}$$

$$I_{5,8,9} = -\overline{I}_{5,8,9}\,. \tag{3.5b}$$

The functions I_{1-9} in Eq. (3.3) can be written in terms of K^{*0} spin amplitudes, A_t, A_0, $A_\parallel$, $A_\perp$[2]; the latter three have both left- and right-handed components and all are functions of q^2. A_t corresponds to the scalar component of the virtual $\overline{K}^{*0}$, which is negligible if the individual lepton masses are small in comparison

[2]These amplitudes are linear combinations of the relevant helicity amplitudes – $A_{\perp,\parallel} = (H_{+1} \mp H_{-1})/\sqrt{2}$, $A_0 = H_0$, $A_t = H_t$ [55].

to the mass of the lepton pair. For $m_l = 0$, we find,

$$
\begin{aligned}
I_1^s &= \frac{3}{4}\left[|A_{\perp L}|^2 + |A_{\parallel L}|^2 + (L \to R)\right] && \text{(3.6a)}\\
I_1^c &= \left[|A_{0L}|^2 + |A_{0R}|^2\right] && \text{(3.6b)}\\
I_2^s &= \frac{1}{4}\left[|A_{\perp L}|^2 + |A_{\parallel L}|^2 + (L \to R)\right], && \text{(3.6c)}\\
I_2^c &= -\left[|A_{0L}|^2 + |A_{0R}|^2\right] && \text{(3.6d)}\\
I_3 &= \frac{1}{2}\Big[(|A_{\perp L}|^2 - |A_{\parallel L}|^2) + (L \to R)\Big], && \text{(3.6e)}\\
I_4 &= \frac{1}{\sqrt{2}}\Big[\mathrm{Re}(A_{0L}A_{\parallel L}^*) + (L \to R)\Big], && \text{(3.6f)}\\
I_5 &= \sqrt{2}\Big[\mathrm{Re}(A_{0L}A_{\perp L}^*) - (L \to R)\Big], && \text{(3.6g)}\\
I_6^s &= 2\Big[\mathrm{Re}(A_{\parallel L}A_{\perp L}^*) - (L \to R)\Big], && \text{(3.6h)}\\
I_7 &= \sqrt{2}\Big[\mathrm{Im}(A_{0L}A_{\parallel L}^*) - (L \to R)\Big], && \text{(3.6i)}\\
I_8 &= \frac{1}{\sqrt{2}}\Big[\mathrm{Im}(A_{0L}A_{\perp L}^*) + (L \to R)\Big], && \text{(3.6j)}\\
I_9 &= \Big[\mathrm{Im}(A_{\parallel L}^*A_{\perp L}) + (L \to R)\Big]. && \text{(3.6k)}
\end{aligned}
$$

The $(L \to R)$ terms above represent a repeat of the previous terms with the left-handed amplitudes exchanged for right-handed. Note that $I_1^s = 3I_2^s$ and $I_1^c = -I_2^c$. It is by extracting the values of the K^{*0} spin amplitudes that we can detect the effects of physics beyond the SM acting on the underlying Wilson coefficients.

3.2 Symmetries

The angular distribution has four independent global symmetries in the $m_l = 0$ limit. In this case there is no interference between right- and left-handed amplitudes, the distribution is invariant under both L and R global phase transformations,

$$A'_{\perp L} = e^{i\phi_L}A_{\perp L},\ A'_{\parallel L} = e^{i\phi_L}A_{\parallel L},\ A'_{0L} = e^{i\phi_L}A_{0L} \tag{3.7}$$

and

$$A'_{\perp R} = e^{i\phi_R}A_{\perp R},\ A'_{\parallel R} = e^{i\phi_R}A_{\parallel R},\ A'_{0R} = e^{i\phi_R}A_{0R}\ . \tag{3.8}$$

There is a global symmetry under continuous $L \leftrightarrow R$ rotations,

$$\begin{aligned}
A^{'}_{\perp L} &= +\cos\theta A_{\perp L} + \sin\theta A^{*}_{\perp R} \\
A^{'}_{\perp R} &= -\sin\theta A^{*}_{\perp L} + \cos\theta A_{\perp R} \\
A^{'}_{0L} &= +\cos\theta A_{0L} - \sin\theta A^{*}_{0R} \\
A^{'}_{0R} &= +\sin\theta A^{*}_{0L} + \cos\theta A_{0R} \\
A^{'}_{\parallel L} &= +\cos\theta A_{\parallel L} - \sin\theta A^{*}_{\parallel R} \\
A^{'}_{\parallel R} &= +\sin\theta A^{*}_{\parallel L} + \cos\theta A_{\parallel R}.
\end{aligned} \tag{3.9}$$

One consequence of this is that the L and R labels are actually arbitrary, as L amplitudes can be rotated to R amplitudes and *vice-versa*. Finally there is a fourth global continuous symmetry which was unknown at the time of writing Ref. [1],

$$\begin{aligned}
A^{''}_{\perp L} &= +\cosh i\phi A_{\perp L} + \sinh i\phi A^{*}_{\perp R} \\
A^{''}_{\perp R} &= +\sinh i\phi A^{*}_{\perp L} + \cosh i\phi A_{\perp R} \\
A^{''}_{0L} &= +\cosh i\phi A_{0L} - \sinh i\phi A^{*}_{0R} \\
A^{''}_{0R} &= -\sinh i\phi A^{*}_{0L} + \cosh i\phi A_{0R} \\
A^{''}_{\parallel L} &= +\cosh i\phi A_{\parallel L} - \sinh i\phi A^{*}_{\parallel R} \\
A^{''}_{\parallel R} &= -\sinh i\phi A^{*}_{\parallel L} + \cosh i\phi A_{\parallel R}.
\end{aligned} \tag{3.10}$$

These relations must be taken into account when constructing both angular observables and the full-angular fit.

3.3 Theoretical cleanliness

As discussed in Chap. 5, the framework of QCD factorization (QCDf) can be used to separate physics effects operating at different energy scales so that they can be considered independently. Starting from the effective $b \to s l^+ l^-$ Hamiltonian, the matrix element for $\overline{B}_d \to \overline{K}^{*0}(\to K\pi)\mu^+\mu^-$ can be written as [55],

$$\begin{aligned}
\mathcal{M} = &\frac{G_F \alpha_s}{\sqrt{2}\pi} V_{\rm tb} V^*_{\rm ts} \Bigg\{ \Bigg[C_9^{\rm eff} \langle K\pi | \bar{s}\gamma^\mu P_L b | B\rangle \\
&- \frac{2m_b}{q^2} C_7^{\rm eff} \langle K\pi | \bar{s} i\sigma^{\mu\nu} q_\nu P_R b | B\rangle \Bigg] (\bar{l}\gamma_\mu l) \\
&+ C_{10}^{\rm eff} \langle K\pi | \bar{s}\gamma^\mu P_L b | B\rangle (\bar{l}\gamma_\mu\gamma_5 l) \Bigg\},
\end{aligned} \tag{3.11}$$

where the helicity suppressed contributions have been neglected and non-standard symbols are defined in Chap. 5 or below. The hadronic part of the matrix element describes the $B \to K\pi$ decay. It can be parametrized in terms of form factors by finding the most general expansion which is invariant under the Lorentz group using an approximation (see for example [100]) where the width of the K^{*0} is neglected. The form factors are scalar functions which give the relative contribution of each possible term. For $\overline{B}_d \to \overline{K}^{*0}\mu^+\mu^-$, there are seven form factors and they are functions of q^2. Conceptually they parametrize the q^2 dependence of the K^{*0} formation and are defined in the following way [55]:

$$\begin{aligned}\langle K^*(p_{K^*})|\bar{s}\gamma_\mu P_{L,R} b|B(p)\rangle = i\epsilon_{\mu\nu\alpha\beta}\epsilon^{\nu *}p^\alpha q^\beta \frac{\boldsymbol{V(q^2)}}{m_B + m_{K^*}} \\ \mp\frac{1}{2}\Bigg\{\epsilon^*_\mu(m_B + m_{K^*})\boldsymbol{A_1(q^2)} - (\epsilon^* \cdot q)(2p-q)_\mu \frac{\boldsymbol{A_2(q^2)}}{m_B + m_{K^*}} \\ -\frac{2m_{K^*}}{q^2}(\epsilon^* \cdot q)[A_3(q^2) - \boldsymbol{A_0(q^2)}]q_\mu\Bigg\},\end{aligned} \tag{3.12}$$

where

$$A_3(q^2) = \frac{m_B + m_{K^*}}{2m_{K^*}}\boldsymbol{A_1(q^2)} - \frac{m_B - m_{K^*}}{2m_{K^*}}\boldsymbol{A_2(q^2)}\,, \tag{3.13}$$

and

$$\begin{aligned}\langle K^*(p_{K^*})|\bar{s}i\sigma_{\mu\nu}q^\nu P_{R,L} b|B(p)\rangle = -i\epsilon_{\mu\nu\alpha\beta}\epsilon^{\nu *}p^\alpha q^\beta \boldsymbol{T_1(q^2)} \\ \pm\frac{1}{2}\Bigg\{[\epsilon^*_\mu(m_B^2 - m_{K^*}^2) - (\epsilon^* \cdot q)(2p-q)_\mu]\boldsymbol{T_2(q^2)} \\ +(\epsilon^* \cdot q)\left[q_\mu - \frac{q^2}{m_B^2 - m_{K^*}^2}(2p-q)_\mu\right]\boldsymbol{T_3(q^2)}\Bigg\}.\end{aligned} \tag{3.14}$$

In the above, ϵ^μ is the K^* polarization vector, and $P_{L,R} = \frac{1}{2}(1 \mp \gamma_5)$ is a projection operator. The seven form factors are shown in bold. In the limit where the B hadron is heavy and the K^{*0} has a large energy, $E_{K^{*0}}$, they can be reduced to two *heavy-to-light transition* form factors, $\xi_{\perp,\parallel}$, the so called *soft* form factors[3]. A double perturbative expansion in $\Lambda_{\rm QCD}/m_b$ and $\Lambda_{\rm QCD}/E_{K^{*0}}$ is employed to make this reduction [64, 101–103] that induces symmetry-breaking corrections of order α_s and $1/m_b$. The α_s corrections are known to Next-to-Leading Order (NLO) [54], but the $\Lambda_{\rm QCD}/m_b$ corrections are not. While there are other approaches available [56], the one described above is most commonly used in the literature.

The seven form factors are *a priori* independent and unknown. They are low-energy quantities which must be calculated within some non-perturbative

[3]These form factors are calculated in the *large recoil* limit where the b and s quarks in the initial and final states are assumed to interact with the spectator quark via the exchange of *soft* gluons.

framework such as in Ref. [104]. Once the reduction is made we are left with only two unknown form factors. Some constraints on these can be set by looking at $B \to K^{*0}\gamma$ decays [54, 74], but they still lead to large theoretical uncertainties on e.g. $\mathcal{B}(B_d \to K^{*0}\mu^+\mu^-)$ [69]. This is a particular problem for NP searches, where robust SM predictions are required.

Once the form factor reductions have been made, at LO we can write the K^{*0} spin amplitudes as [55]:

$$A_{\perp L,R} = \sqrt{2}Nm_B(1-\hat{s})\left[(C_9^{\text{eff}} \mp C_{10}^{\text{eff}}) + \frac{2\hat{m}_b}{\hat{s}}(C_7^{\text{eff}} + C_7'^{\text{eff}})\right]\xi_\perp(E_{K^*}), \quad (3.15a)$$

$$A_{\parallel L,R} = -\sqrt{2}Nm_B(1-\hat{s})\left[(C_9^{\text{eff}} \mp C_{10}^{\text{eff}}) + \frac{2\hat{m}_b}{\hat{s}}(C_7^{\text{eff}} - C_7'^{\text{eff}})\right]\xi_\perp(E_{K^*}), \quad (3.15b)$$

$$A_{0L,R} = -\frac{Nm_B}{2\hat{m}_{K^*}\sqrt{\hat{s}}}(1-\hat{s})^2\left[(C_9^{\text{eff}} \mp C_{10}^{\text{eff}}) + 2\hat{m}_b(C_7^{\text{eff}} - C_7'^{\text{eff}})\right]\xi_\parallel(E_{K^*}), \quad (3.15c)$$

with $\hat{s} = q^2/m_B^2$, $\hat{m}_i = m_i/m_B$, and neglecting A_t. The chirality-flipped operators $\mathcal{O}'_{9,10} = \mathcal{O}_{9,10}(P_L \to P_R)$ may be included by making the substitutions $C_{9,10}^{\text{eff}} \to (C_{9,10}^{\text{eff}} + C_{9,10}'^{\text{eff}})$ in Eq. (3.15a) and $C_{9,10}^{\text{eff}} \to (C_{9,10}^{\text{eff}} - C_{9,10}'^{\text{eff}})$ in Eqs (3.15b) and (3.15c) [55]. It is then possible to find observables which use ratios of these amplitudes to cancel the soft form factor contributions at LO by taking specific combinations of $\xi_{\perp,\parallel}$ [1, 55, 105]. We refer to these observables as being *theoretically clean*. Outside of the $q^2 \in [1,6]\,\text{GeV}^2/c^4$ range these cancellations cannot be made as the assumptions used are no longer valid. This leads to uncontrolled theoretical uncertainties on the observables. It is an important requirement that any observable is invariant under the symmetries presented in Sec. 3.2. This is not true for all observables in the literature including $A_T^{(1)}$ [55], whose extraction was the initial motivation of the analysis presented in the next chapter.

3.4 Observables

We would like to use the angular distribution of $\overline{B}_d \to \overline{K}^{*0}\mu^+\mu^-$ to gain sensitivity to the underlying Wilson coefficients and so to any NP contributions present. This can be done in several ways:

- The angular distribution can be expressed in terms of the Wilson coefficients and a fit made to the observed distribution. Due to the large uncertainty in the form factors introduced by perturbative QCD, this approach would leave us with a large theoretical uncertainty on the extracted Wilson coefficients and correlations between the form factors and Wilson coefficients in the fit.

- For a set of NP models one could compute the full-angular distribution and compare it to the observed angular distribution. On a *model-by-model* basis it would then be possible to exclude them as being incompatible with the observations. This approach is obviously not model independent and would make it very difficult to use the quoted results to exclude models that were not considered at the time of publication.

- One can derive a set of observables that can be extracted directly from the observed angular distribution but at the same time have the advantage that theoretical uncertainties cancel out as discussed in Sec. 3.3. In this way the model independence can be retained while also reducing the theoretical uncertainty in the quoted results. For any new theory these new observables can be calculated at a later date.

We have chosen to investigate the last of these approaches. The observables are carefully constructed combinations of the spin amplitudes, which are themselves functions of the Wilson coefficients and form factors as shown in Eq. (3.15). We need to find observables with good sensitivity to any NP operators, small theoretical uncertainties and finally good experimental resolutions.

The angular observables to be investigated are listed below, where theoretically clean observables are shown in bold:

$$A_{\rm FB} = \frac{3}{2}\frac{\mathrm{Re}(A_{\parallel L}A^*_{\perp L}) - \mathrm{Re}(A_{\parallel R}A^*_{\perp R})}{\Gamma'}; \tag{3.16}$$

$$A_{\rm Im} = \frac{\mathrm{Im}(A_{\perp L}A^*_{\parallel L}) + \mathrm{Im}(A_{\perp R}A^*_{\parallel R})}{\Gamma'}; \tag{3.17}$$

$$\boldsymbol{A_T^{(2)}} = \frac{\boldsymbol{|A_\perp|^2 - |A_\parallel|^2}}{\boldsymbol{|A_\perp|^2 + |A_\parallel|^2}}; \tag{3.18}$$

$$\boldsymbol{A_T^{(3)}} = \frac{\boldsymbol{|A_{0L}A^*_{\parallel L} + A^*_{0R}A_{\parallel R}|}}{\boldsymbol{\sqrt{|A_0|^2|A_\perp|^2}}}; \tag{3.19}$$

$$\boldsymbol{A_T^{(4)}} = \frac{\boldsymbol{|A_{0L}A^*_{\perp L} - A^*_{0R}A_{\perp R}|}}{\boldsymbol{|A^*_{0L}A_{\parallel L} + A_{0R}A^*_{\parallel R}|}}; \tag{3.20}$$

$$F_{\rm L} = \frac{|A_0|^2}{\Gamma'}; \tag{3.21}$$

where

$$A_iA^*_j \equiv A_{iL}(q^2)A^*_{jL}(q^2) + A_{iR}(q^2)A^*_{jR}(q^2) \quad (i,j = 0, \parallel, \perp), \tag{3.22}$$

and

$$\Gamma' = \frac{\mathrm{d}\Gamma}{\mathrm{d}q^2} = \left(|A_{0L}|^2 + |A_{\perp L}|^2 + |A_{\parallel L}|^2 + (L \to R)\right). \tag{3.23}$$

The NP sensitivity provided by each of these observables is model and parameter space dependent, however they have been studied for models with non-SM contributions to $C_7'^{\text{eff}}$ in [1, 55, 57]. In the SM, A_{FB} has a *zero-crossing point*, where $A_{\text{FB}}(q^2)$ vanishes. At this point the soft form factors cancel at LO; the value of q^2 at which this occurs is also theoretically clean. We define this point as $q_0^2(A_{\text{FB}})$. There are no such cancellations found for F_{L} or A_{Im}. Further theoretical discussions of the observables will be left to Ref. [1].

In addition to these constructed observables, it is possible to consider the angular coefficients I_{1-9}. These are generally not theoretically clean but are more directly linked with the angular distribution. Chap. 6 looks in more detail at this as a way of finding NP effects in the angular distribution in the first few years of LHCb data-taking.

3.5 Estimating Λ_{QCD}/m_b corrections

The theoretically clean observables highlighted in Sec. 3.4 are expected to have reduced theoretical uncertainties due to the cancellation of the soft form factors. However the relations used to make these cancellations are only valid at LO in the Λ/m_b expansion, and corrections to higher orders are not known. For these theoretically clean observables to be useful, the impact of these corrections on the observables must be robustly bounded. If NP is to be discovered in $\overline{B}_d \to \overline{K}^{*0}\mu^+\mu^-$, it must be possible to demonstrate that any effect seen is indeed NP and not just the effect of an unknown SM correction. Various solutions to this problem are evaluated.

3.5.1 Ensemble method

One relatively conservative approach to this is to parametrize each of the K^{*0} spin-amplitudes with some unknown linear correction,

$$A_i' = A_i^0(1 + C_i e^{i\theta_i}). \tag{3.24}$$

C_i gives the size of the correction relative to the full NLO amplitude A_i^0 and θ_i is an associated strong phase. If we vary C_i and θ_i within their chosen ranges, an estimate for the theoretical uncertainty due to these unknown parameters can be found. In order to make this parametrization generic, however, extra terms must be introduced. In principle the effective Hamiltonian which controls the decay has three terms,

$$\mathcal{H}_{\text{eff}} = \mathcal{H}_{\text{eff}}^{(u)\text{SM}} + \mathcal{H}_{\text{eff}}^{(t)\text{SM}} + \mathcal{H}_{\text{eff}}^{(t)\text{NP}}. \tag{3.25}$$

The first term is very small, arising from doubly-Cabibbo suppressed penguin diagrams, but is responsible for all the SM *CP*-violation in the decay. It is neglected for most purposes in this thesis. The second term is responsible for the decay in the SM while the third adds possible NP contributions. The fourth possible term $\mathcal{H}_{\rm eff}^{(u)\rm NP}$ generically does not contribute to the model independent amplitudes and is neglected. Each of these contributions is generated by different sets of diagrams and so in principle can have different values of C_i and θ_i. The amplitude parametrization must be modified so that each of the three possible sub-amplitudes is treated separately [6],

$$\begin{aligned} A = &\left[(A_{\rm SM}(\lambda_u \neq 0) - A_{\rm SM}(\lambda_u = 0)) \times (1 + C_1 e^{i\theta_1})\right] + \\ &\left[A_{\rm SM}(\lambda_u = 0) \times (1 + C_2 e^{i\theta_2})\right] + \\ &\left[(A_{\rm Full}(\lambda_u \neq 0) - A_{\rm SM}(\lambda_u \neq 0)) \times (1 + C_3 e^{i\theta_3})\right]. \end{aligned} \tag{3.26}$$

The full amplitude $A_{\rm Full}(\lambda_u \neq 0)$ includes all NP and SM contributions, however it is assumed that only one NP operator is active so as not to introduce extra terms. The sub-amplitudes can then be extracted from the full amplitude calculation by applying Eq. (3.26) to the SM amplitudes with ($\lambda_u \neq 0$) and without ($\lambda_u = 0$) the *CP*-violating contributions; λ_u is the product of the $b \to d$ CKM elements $V_{\rm ub}V_{\rm us}^*/V_{\rm tb}V_{\rm ts}^*$.

An estimate of the theoretical uncertainty arising from the unknown Λ/m_b corrections and strong phases can now be made using a randomly selected ensemble. For each member of the ensemble, values of C_{1-3} and θ_{1-3} are chosen in the ranges $C_i \in [-0.1, 0.1]$ or $C_i \in [-0.05, 0.05]$ and $\theta_i \in [-\pi, \pi]$ using the random uniform distribution. This is done for the seven K^{*0} spin-amplitudes, A_t, $A_{0L,R}$, $A_{\parallel L,R}$, $A_{\perp L,R}$, to provide a complete description of the decay, $\mathcal{M}_i$, using the full distribution with $m_l = m_\mu$. It is assumed that the corrections and phases are not functions of q^2, although in practise they may actually be. Any (unknown) correlations are also ignored. While these effects could lead to an underestimate of the theoretical envelope, it is thought that this method allows for a conservative estimate of the theoretical uncertainties to be made [6]. An ensemble of these amplitudes was created, $\{\mathcal{M}_i\}^{500}$.

To estimate the contribution to the theoretical uncertainties from Λ/m_b corrections for a particular observable, each element in the ensemble was used to calculate the value of that observable at a fixed value of q^2. This gave five hundred values of the observable, which were then sorted. The size of the theoretical envelope could be estimated by selecting the values closest to the one σ contour. This was done for both $C_i \in [-0.05, 0.05]$ and $C_i \in [-0.1, 0.1]$ to illustrate the effects of five and ten percent corrections. By repeating this process for different

values of q^2, bands can be built up. These show the likely range of values that the observable will have in the presence of a small and approximately linear correction and strong phase. In principle, this method could be extended to other forms of theoretical uncertainties to improve the statistical validity of, e.g., scale dependence and parametric uncertainties. However, computational constraints make this difficult for calculations implemented in MATHEMATICA.

3.5.2 Quadrature method

The method presented above must be contrasted to that used in Ref. [1]. In that case a similar parametrization was made,

$$A_i' = A_i^0(1 + C_i), \tag{3.27}$$

and *CP*-violatating effects were neglected. To calculate the theoretical uncertainties from Λ/m_b corrections for a particular observable at a fixed value of q^2, each amplitude was varied in turn while keeping the others at their central values. The seven differences in the observable were then added in quadrature to produce a total estimate of the theoretical uncertainty. This process was repeated for all values of q^2 and with C_i set to 0.05 and 0.1. This procedure is however statistically dubious. There is no reason to expect all amplitudes to receive the maximum possible correction, even if we assume that a ten percent correction is genuinely the largest allowed. Adding the differences in quadrature is also unlikely to produce a correct estimate, as there are few normally distributed quantities present. It will be shown that the quadrature method provides an over-estimate of the probable contribution from Λ/m_b corrections. This is obviously significant when it comes to comparing theoretical and experimental results at LHCb.

3.5.3 Results

The full QCDf amplitudes were used as input to the two methods described above. Those used with the quadrature method are detailed in Ref. [1], while those for the ensemble method were updated versions from [6]. We choose to compare the observable $A_T^{(2)}$, whose central value is approximately zero in both treatments. Any differences in the size of the estimated Λ/m_b uncertainties should then be due to the difference in methods used. This can be seen in Fig. 3.2. The corrections estimated using the quadrature are over twice the size of those found using the ensemble. While there are assumptions in either approach, it is thought that the ensemble approach produces a more realistic estimate of the contribution of unknown Λ/m_b corrections to the overall theoretical uncertainty. This will have

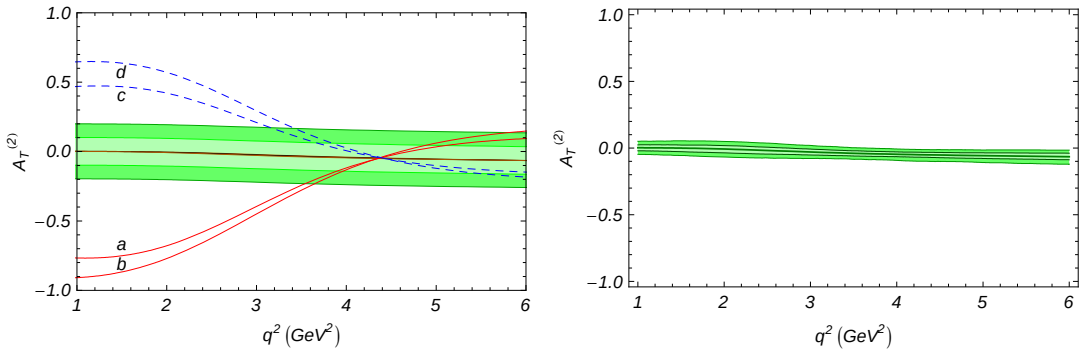

(a) Quadrature (b) Ensemble

Figure 3.2: Fig. (a) shows the effect of unknown five (light band) and ten (dark band) percent Λ/m_b corrections on $A_T^{(2)}$ [1]. These were produced with the quadrature method described in Sec. 3.5.2. Four NP models, described in Ref. [57], are shown for comparison. The small dark (orange) band shows the contribution from the soft form factors, as well as parametric and scale uncertainties to the final error. Fig. (b) shows the same thing, but using the ensemble method described in Sec. 3.5.1. However, only the Λ/m_b bands are shown.

implications when considering the overall theoretical uncertainty estimate.

3.5.4 Adding new physics

The methods presented above can be used to estimate the effects of Λ/m_b corrections in the presence of NP. The model independent amplitudes described in Ref. [6] include both real and imaginary NP contributions to the Wilson coefficients C_9^{eff}, C_{10}^{eff}, and $\mathcal{C}_{S,P}^{(\prime)}$ including all NLO QCD effects. When evaluating observables, it is useful to see whether they provide enough sensitivity to NP once all theoretical uncertainties have been taken into account. If they are in principle distinguishable theoretically, it then becomes interesting to know whether they are distinguishable experimentally. This will be dealt with in the next chapter. Fig. 3.3 shows the distributions of the theoretically clean observables $A_T^{(2)}$, $A_T^{(3)}$, and $A_T^{(4)}$ in the presence of NP contributions to C_9^{eff} and $C_{10}^{(\prime)\,\text{eff}}$. It can be seen that there is considerable sensitivity to NP effects in these Wilson coefficients, particularly in $A_T^{(3)}$ and $A_T^{(4)}$. The variation in $A_T^{(2)}$ is less extreme, but it has been optimized for sensitivity to $C_7^{\prime\,\text{eff}}$ [57], which was not changed here. The magnitudes and phases of the NP contribution to each Wilson coefficient should be compared to the currently allowed parameter space presented in Chap. 6.

The impact of Λ/m_b corrections on observables sensitive to *CP*-violation can also be studied. In Ref. [106] it is shown that their effect is negligible on the available *CP* asymmetries, the exact definitions of which will be left until Chap. 6 (Eq. (6.2)). As explained in Sec. 3.5.1, the *CP*-violation coming from the CKM

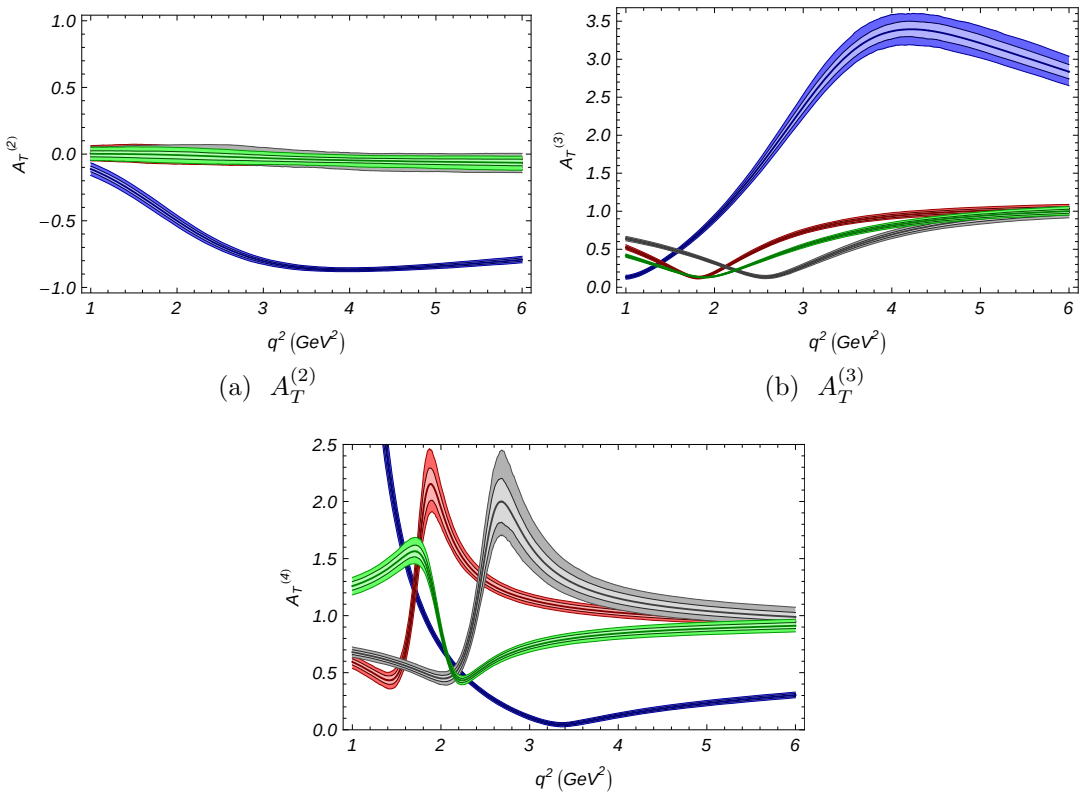

(a) $A_T^{(2)}$ (b) $A_T^{(3)}$

(c) $A_T^{(4)}$

Figure 3.3: The effect of unknown five (light band) and ten (dark band) percent Λ/m_b corrections, estimated using the ensemble method, on the theoretically clean observables $A_T^{(2)}$, $A_T^{(3)}$, and $A_T^{(4)}$ in the presence of NP. In each case, the green bands show the SM distribution, while the red, grey and blue bands show $C_9^{\text{eff NP}} = 2e^{i\frac{\pi}{8}}$, $C_{10}^{\text{eff NP}} = 1.5e^{i\frac{\pi}{8}}$, and $C_{10}'^{\text{eff}} = 2e^{i\frac{\pi}{8}}$ respectively.

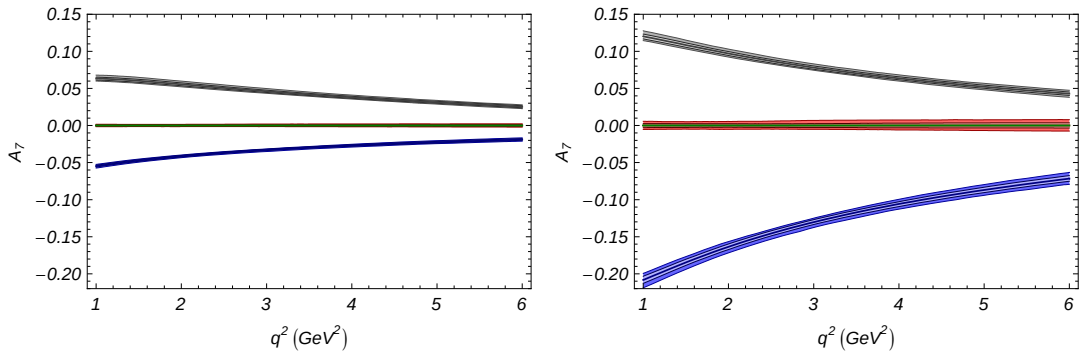

(a) $\frac{\pi}{8}$ (b) $\frac{\pi}{2}$

Figure 3.4: The effect of unknown five and ten percent Λ/m_b corrections on the *CP* asymmetry A_7 for two different values of the NP phase. The colour coding is the same as in Fig. 3.3, but in Fig. (a) the NP phase is $\frac{\pi}{8}$ while in Fig. (b) it is $\frac{\pi}{2}$.

matrix is very small. Any significant *CP*-violation would have to come from a mechanism beyond this. This is included by allowing the Wilson coefficients to acquire new weak phases. Fig. 3.4 shows estimates for the Λ/m_b related uncertainties for the *CP* asymmetry A_7, the rate averaged asymmetry of I_7. As shown in Ref. [56], this asymmetry can become quite large in the presence of NP. However it can be seen from the figure that the Λ/m_b uncertainties scale with the value of the observable. The assumption that these corrections can be neglected for the *CP* asymmetries is probably not valid. These uncertainties must be included when making comparisons to the SM.

3.6 Summary

In this chapter the basic properties of the $\overline{B}_d \to \overline{K}^{*0}\mu^+\mu^-$ angular distribution relevant to making an experimental analysis have been presented. It has been shown that the angular distribution is subject to four continuous global symmetries. These will be of particular importance when it comes to constructing a full-angular analysis. A selection of observables that are both invariant under these symmetries and theoretically clean have been presented. These use specific combinations of the K^{*0} spin amplitudes to cancel the dependence on two universal heavy-to-light form factors $\xi_{\perp,\parallel}$ at LO. They are however then dependent on unknown Λ/m_b corrections, arising from reducing the number of form factors from seven to two. A simple parametrization was presented that can be used to investigate the likely impact of these corrections on the theoretically clean observables. It was shown that for *CP*-conserving observables such as $A_T^{(2)}$, the expected Λ/m_b corrections are smaller than previously thought. It was also shown that the opposite is true for the *CP* asymmetries. This will be particularly useful once

LHCb data sets become large enough to perform a full-angular analysis, which is the subject of the next chapter.

Chapter 4

Performing the full-angular analysis of $\overline{B}_d \to \overline{K}^{*0}\mu^+\mu^-$

The rare decay $\overline{B}_d \to \overline{K}^{*0}(\to K\pi)\mu^+\mu^-$ can be used to probe the inner workings of the $b \to s$ quark transition by studying its angular distribution. This provides information beyond that available from $\mathcal{B}(b \to s\gamma)$ measurements alone. In addition to the $\mathcal{O}_7^{(\prime)}$ operators active in those decays, $\mathcal{O}_{9,10}^{(\prime)}$ can also make significant contributions away from the photon pole (see Sec. 5.2.6). The angular dependence of each term active in the distribution (see Eq. (3.2)) means that the contributions of the different operators can be disentangled. There are enough independent angular observables available to fully constrain the operators expected to play a significant role in the decay, allowing both the magnitude and phase of each of the relevant Wilson coefficients to be measured. This could allow for physics beyond the SM to be discovered. However, it also offers the opportunity to learn something of the underlying gauge structure of the NP if discovered elsewhere. The huge statistics at LHCb should make the full-angular analysis of this decay possible for the first time. There will be other interesting measurements on the way (see for example Chap. 6), but it is the full-angular analysis which offers the chance to extract all of the available information from the decay. This has the potential to be one of the most exciting measurements made by LHCb.

In the previous chapter, the properties of the angular distribution were introduced, as were a set of observables with reduced theoretical uncertainties. While $A_T^{(2)}$ is available with poor resolution using a counting experiment or one-dimensional fit, $A_T^{(3)}$ and $A_T^{(4)}$ are only available via the full-angular analysis [107]. It was for this reason that a fit was developed, leading to Refs [1, 2]. At the time of their publication, the symmetry shown in the previous chapter as Eq. (3.10) was not known. Many of the results shown in this chapter were produced without this symmetry. The implications of this will be dealt with in Sec. 4.6.

4.1 Sensitivity at LHC*b*

Theoretical treatments of $\overline{B}_d \to \overline{K}^{*0}\mu^+\mu^-$ at NLO normally make use of the QCD factorization (QCDf) framework [65, 66, 108] as described in Ref. [54]. These calculations are involved and while it is now possible to perform a Monte Carlo (MC) simulation of the decay using a full treatment, as described in Chap. 5, this was not the case when the bulk of the work presented in this chapter was undertaken. Instead a toy MC approach was used where the results of the full calculation from Ref. [1] are used as input to a toy model. This allows the generation of toy LHC*b* data sets which can then be used to verify the fitting methods presented in the next sections and assess their relative merits.

4.1.1 A toy model of $\overline{B}_d \to \overline{K}^{*0}\mu^+\mu^-$

A toy Monte Carlo model of the decay was created within the RooFit framework [109] using Eq. (3.2) as a probability density function (PDF). The function $I(q^2, \theta_\ell, \theta_{K^*}, \phi)$ is parametrized in terms of the real and imaginary parts of the spin amplitudes, $A_{\perp L,R}$, $A_{\parallel L,R}$, and $A_{0L,R}$, giving twelve parameters for each point in q^2. It was assumed that $m_l = 0$ and A_t was neglected as explained in the previous chapter.

The symmetry relations introduced in Sec. 3.2 can be exploited to reduce the number of free parameters in the system. Eq. (3.7) is used to make A_{0L} real by setting $\phi_L = -\arg(A_{0L})$ and similarly for A_{0R} with Eq. (3.8). Eq. (3.9) can then be used to remove A_{0R} completely by setting $\theta = \arctan(-A_{0R}/A_{0L})$. This leaves nine free parameters at each point in q^2. One more parameter can be eliminated by recognizing that the angular observables are not sensitive to the absolute normalization which cancels in each case. Sensitivity can be gained to the relative normalization, Γ', by performing an explicit normalization at some fixed value of q^2, here denoted X_0. We divide all spin amplitudes by the value of $\mathrm{Re}(A_{0L})$ at $X_0 = 3.5\,\mathrm{GeV}^2/c^4$. This leaves the eight degrees of freedom. The effect of adding the fourth available symmetry constraint will be assessed in Sec. 4.6.

Following Ref. [107], the signal is assumed to have a Gaussian distribution in m_B with a width of $14\,\mathrm{MeV}/c^2$ in a window of $m_B \pm 50\,\mathrm{MeV}/c^2$ and a Breit-Wigner in $m_{K\pi}$ with width $48\,\mathrm{MeV}/c^2$ in a window of $m_{K^{*0}} \pm 100\,\mathrm{MeV}/c^2$. A simplified background model is included. This is uniformly distributed in all angles, effectively treating all background as combinatorial, but follows the q^2 distribution of the signal. Acceptance effects have been studied in Ref. [8], where it is shown that the detector's geometric acceptance produces the main effect, with the trigger and offline selection having little extra impact. A data-driven acceptance correction is being investigated, and so these effects are neglected in this study. *CP* violation

effects are also neglected, allowing us to treat $\overline{B}_d \to \overline{K}^{*0}\mu^+\mu^-$ and its charge conjugate simultaneously. Contributions from non-resonant $\overline{B}_d \to K^-\pi^+\mu^+\mu^-$ events are not included, as they can not normally be treated within QCDf.

4.1.2 Generation of toy data

The model described in the last section allows the probability of a particular set of observables (θ_ℓ, θ_{K^*}, ϕ and q^2) occurring to be calculated. The overall normalization of the PDF is not known *a priori*, however it could be determined numerically by integrating Γ', defined in Eq. (3.23), over the allowed q^2 range. This is done explicitly using the GNU Scientific Library (GSL) [110]. An accept/reject algorithm can then be used to generate a data set of events with the correct distributions. The q^2 dependence of the spin amplitudes is included by generating many sub-data sets in $0.05\,\mathrm{GeV}^2/c^4$ q^2 bins and then combining them, so avoiding the q^2 parametrization introduced in the next section. In each sub-bin, Γ' weighted mean spin amplitudes, found using values taken from Ref. [1], were used when calculating $I(q^2, \theta_\ell, \theta_{K^*}, \phi)$. The number of events for a given q^2 sub-bin is

$$n_{s,b} = N_0^{s,b} \frac{\int_{q_{\min}}^{q_{\max}} \Gamma'}{\int_{4\,\mathrm{m}_\mu^2}^{9\,\mathrm{GeV}^2/c^4} \Gamma'}\,, \tag{4.1}$$

where N_0^s is the number of signal events expected in $2\,\mathrm{fb}^{-1}$ for $q^2 \in [4\mu^2, 9]\,\mathrm{GeV}^2/c^4$ ($N_0^s = 4032$, giving a total selection efficiency of approximately 1%.) [72] and Γ' is derived from the input amplitude calculation. As $\mathcal{H}_{\mathrm{eff}}^{(u)\mathrm{SM}}$ is neglected, the B and $\overline{B}$ contributions for each sample can be generated together. The number of background events was calculated in the same way with the value of N_0^b taken from the same full simulation study ($N_0^b = 1168$). In both cases the value of $n_{s,b}$ is Poisson fluctuated so that not all toy data sets are of the same size. For 10 and $100\,\mathrm{fb}^{-1}$ samples N_0^s and N_0^s were scaled linearly. NP models were dealt with by supplying input spin amplitude values, again from [1], for a particular NP model.

4.1.3 Fitting of data to extract sensitivities

As discussed in Sec. 4.1.1, the decay PDF has eight unconstrained spin amplitudes at each point in q^2, which can be extracted from data using a fit. The q^2 dependence of these amplitudes must be taken into account. We can explicitly parametrize this dependence or divide the experimental data into a small number of q^2 bins (ideally a single 1-6 GeV/c^2 bin) and perform an independent fit in each bin, making the assumption that the q^2 dependence can be neglected. The latter approach allows for fewer parameters to be used, assuming the number of bins

is ≤ 3, but produces significant systematic fit biases if the q^2 dependence across the bin is non-linear and the effect ignored. These biases arise from the differing q^2 dependence of each of the spin amplitude components and appear even if the fit is properly convergent[1]. It was found that the biases could not be eliminated while preserving enough statistics in each bin to perform the fit reliably. Instead an unbinned approach was used where the q^2 dependence of each spin amplitude component is parametrized as a 2^{nd} order polynomial, the coefficients of which are then extracted.

The parametrization is as follows. For $\text{Re}(A_{0L})$ we use a standard polynomial

$$f_p(q^2) = A_p(q^2 - X_0)^2 + B_p(q^2 - X_0) + C_p, \tag{4.2}$$

where A_p, B_p, and C_p are constant coefficients and X_0 is defined below. This form allows a normalization choice, made at the point $f_p(X_0)$, to directly constrain C_p. For the other amplitude components we use a Chebyshev polynomial,

$$f_c(q^2) = A_c(2(q^2 - X_0)^2 - 1) + B_c(q^2 - X_0) + C_c, \tag{4.3}$$

to improve fit stability. In this parameterization, the polynomials corresponding to the amplitude components $\text{Re}(A_{0R})$, $\text{Im}(A_{0L})$, and $\text{Im}(A_{0R})$ are $f_c^{\text{Re}(A_{0R})} = f_c^{\text{Im}(A_{0L})} = f_c^{\text{Im}(A_{0R})} = 0$ for all q^2, while the constant term of the polynomial parameterizing $\text{Re}(A_{0L})$, $C_p^{\text{Re}(A_{0L})}$, is set to one once the symmetry transforms and normalization, introduced in Sec. 4.1.1, have been applied. Making a measurement in this framework requires that the polynomial ansatz be satisfied for all spin amplitude components in the range $q^2_{\text{min}} - q^2_{\text{max}}$. Fig. A.1 in Appendix A shows an example data set, generated following Sec. 4.1.2, where numerical projections of the final polynomial PDF for each of the experimental observables can be seen. The background component is also shown separately. The agreement between the binned generation PDF and the unbinned fitting PDF is excellent.

By generating an ensemble of toy-LHCb data sets and then fitting them with the polynomial model, the experimental sensitivities for a given integrated luminosity can be estimated and any biases introduced by the method can be found. The fit was well behaved but could be sensitive to the initial values chosen for the fit parameters. To deal with this, the fit was run repeatedly with randomly chosen initial values until an accurate covariance matrix was found[2]. Each refit was initialized from scratch so that each refit result was independent of the last.

[1] If it was possible to integrate Eq. (3.2) over q^2 then these problems could be avoided. However it is not possible to do this in a model independent way as the q^2 dependence of the spin amplitudes must be explicitly known.

[2] Signified by a `Minuit` covariance quality of three.

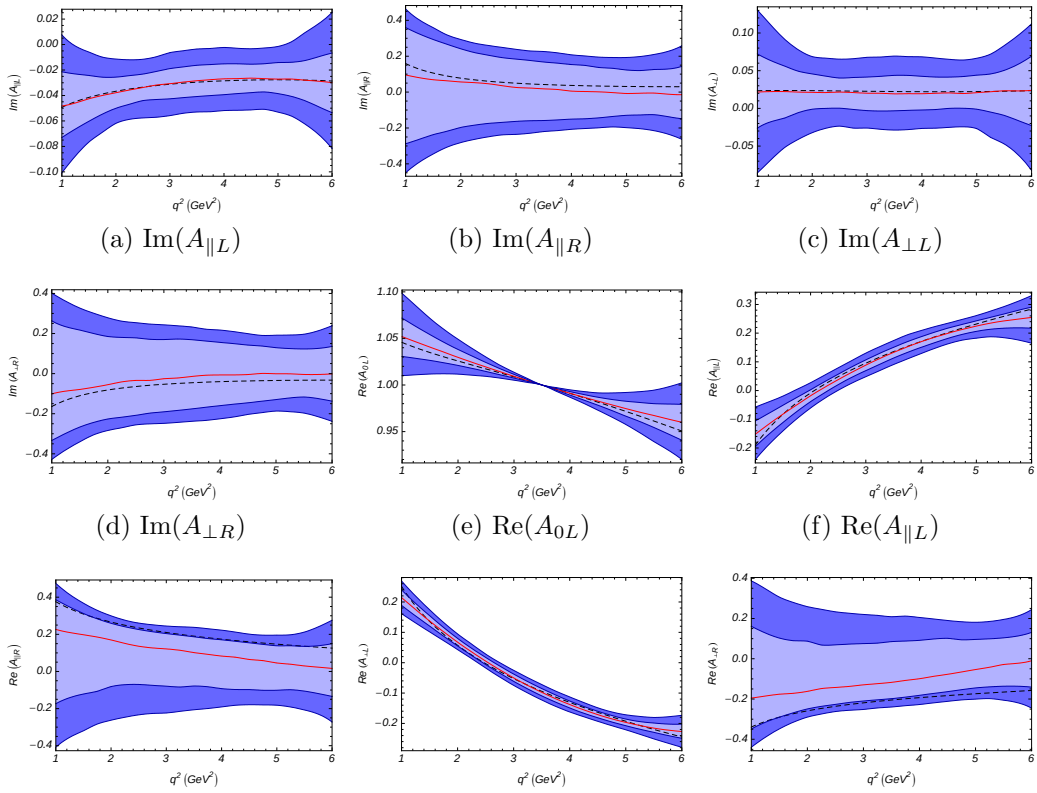

(a) $\mathrm{Im}(A_{\parallel L})$ (b) $\mathrm{Im}(A_{\parallel R})$ (c) $\mathrm{Im}(A_{\perp L})$

(d) $\mathrm{Im}(A_{\perp R})$ (e) $\mathrm{Re}(A_{0L})$ (f) $\mathrm{Re}(A_{\parallel L})$

(g) $\mathrm{Re}(A_{\parallel R})$ (h) $\mathrm{Re}(A_{\perp L})$ (i) $\mathrm{Re}(A_{\perp R})$

Figure 4.1: Sensitivity bands for the individual spin amplitude components as a function of q^2 for $10\,\mathrm{fb}^{-1}$ of SM data. The dashed black line is the SM input distribution. The solid red line shows the median result over an ensemble of a thousand toy experiments, while the light and dark bands show the one and two σ confidence levels. The effect of the normalization at $q^2 = X_0 = 3.5\,\mathrm{GeV}^2/c^4$ can be seen on $\mathrm{Re}(A_{0L})$, as can the strong anti-correlation between $\mathrm{Re}(A_{\parallel R})$ and $\mathrm{Re}(A_{\perp R})$.

For an ensemble of 1076 $10\,\mathrm{fb}^{-1}$ experiments, each of which assumed the SM, the mean number of refits required was 2.97, and the maximum was 103. For 1006 $2\,\mathrm{fb}^{-1}$ SM data sets the mean increased to 6.81 and 0.7% of experiments failed to converge at all[3]. It was verified that the final fit results were independent of the starting values by performing several refits of each data set. Any variation on the output of repeated successful refits was seen to be small compared to the errors on the fit parameters.

There were significant correlations between parameters in some of the experiments. The constant terms of $\mathrm{Re}(A_{\parallel R})$ and $\mathrm{Re}(A_{\perp R})$ and to a lesser extent those of $\mathrm{Im}(A_{\parallel R})$ and $\mathrm{Im}(A_{\perp R})$ were anti-correlated, leading to significant biases on these parameters. The biases were not seen in the angular observables, but are

[3]The maximum number of allowed refits was fixed at 1600 in order to limit the amount of Grid resources used. This number could be dramatically increased if required when the real measurement was made.

obvious in the individual amplitude components shown in Fig. 4.1. This is symptomatic of an extra symmetry in the angular distribution and eventually aided its discovery [6].

4.2 Results

The methods described in Sec. 4.1 were used to generate and fit ensembles of experiments for three different LHCb integrated luminosities; 2, 10, and 100 fb^{-1}. These are the expected data set sizes for a nominal year of data-taking, at the end of LHCb data-taking and at the end of a run with an upgraded SuperLHCb detector respectively. The results for 10 fb^{-1} will be presented here, while those for the other integrated luminosities are available in Appendix A.

Fig. 4.2a shows the experimental sensitivity to A_{FB} in the SM as derived from the ensemble of 10 fb^{-1} experiments. The median value is shown as the solid (red) line while the light and dark (blue) regions mark the contours of one and two σ significance at their external boundaries. These are calculated, as in Chap. 3, by ordering the ensemble of results and then selecting 33% and 47.5% of experiments either side of the median at any given q^2 value.

Fig. 4.2b shows explicitly the ensemble of A_{FB} zero-crossing point results[4]. By comparing the dashed black SM and median lines in both figures, the agreement between input and output distributions can be seen. The fit fails to reproduce the input exactly, but the discrepancy is small compared to the overall experimental uncertainty. These discrepancies seem to be due to the failure of the polynomial ansatz, and are particularly significant at the edges of the q^2 region under consideration as seen by the deviation of the solid red (input) and dashed black (median fit result) lines in the figure.

Figs. 4.3a and 4.3b show the sensitivity bands for the new observables $A_T^{(3)}$ and $A_T^{(4)}$. The limitations of the polynomial ansatz can again be seen, but the overall shape is well reproduced, and the deviation is small compared to the statistical errors. Figs. 4.4a, 4.4b and 4.4c show respectively the sensitivity bands for A_{Im}, $A_T^{(2)}$ and F_{L}. Like A_{FB}, these observables are also accessible by making projection fits as discussed in Sec. 4.3. Finally Fig. 4.4d shows the sensitivity band for Γ' relative to the point $X_0 = 3.5\,\text{GeV}^2/c^4$, the midpoint of the q^2 range.

[4]One of the thousand toy experiments did not have a zero-crossing point and so is excluded from the distribution.

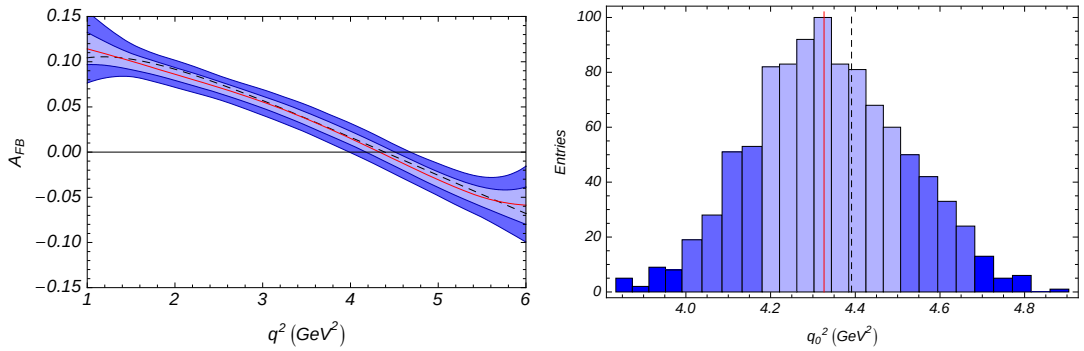

(a) $A_{\rm FB}$ (b) $A_{\rm FB}$ zero-crossing

Figure 4.2: (a) The estimated experimental sensitivity to $A_{\rm FB}$ as a function of q^2 for a $10\,{\rm fb}^{-1}$ sample of LHCb data, assuming the SM. (b) The ensemble of $A_{\rm FB}$ zero-crossing points found from each experiment, giving an estimated value of $4.33^{+0.15}_{-0.18}\,{\rm GeV}^2/c^4$. The colour scheme is the same as in Fig. 4.1, but zero-crossings outside the ninety-five percent confidence are also shown in the outer, dark blue, regions.

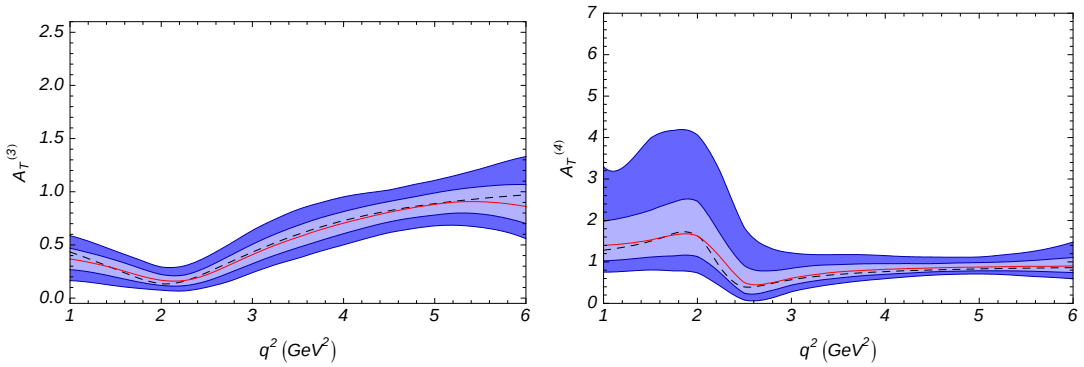

(a) $A_T^{(3)}$ (b) $A_T^{(4)}$

Figure 4.3: Estimated experimental sensitivities to (a) $A_T^{(3)}$ and (b) $A_T^{(4)}$ as a function of q^2 for $10\,{\rm fb}^{-1}$ of LHCb data assuming the SM. The colour scheme is the same as in Fig. 4.1.

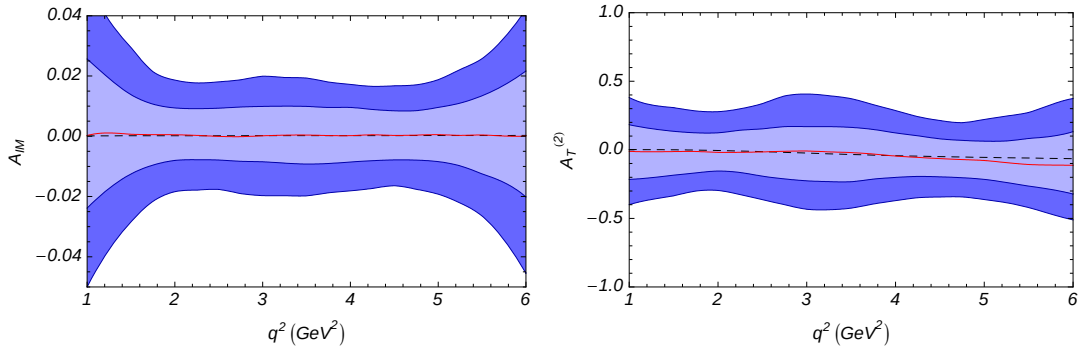

(a) $A_{\rm Im}$ (b) $A_T^{(2)}$

(c) $F_{\rm L}$ (d) Γ'

Figure 4.4: Estimated experimental sensitivities to (a) $A_{\rm Im}$, (b) $A_T^{(2)}$, (c) $F_{\rm L}$ and (d) Γ', as a function of q^2 for $10\,{\rm fb}^{-1}$ of LHCb data assuming the SM. The colour scheme is the same as in Fig. 4.1.

4.3 Comparison with a simultaneous projection fit

4.3.1 $A_{\rm FB}$, $A_{\rm Im}$, $A_T^{(2)}$ and $F_{\rm L}$

In Ref. [107], angular projections over Eq. (3.2) were used to extract the parameters $A_{\rm FB}$, $A_{\rm Im}$, $A_T^{(2)}$ and $F_{\rm L}$ in bins of q^2. For the $\overline{B}_d$ decay:

$$\frac{d\Gamma'}{d\phi} = \frac{\Gamma'}{2\pi}\left(1 + \frac{1}{2}(1-F_{\rm L})A_T^{(2)}\cos 2\phi + A_{\rm Im}\sin 2\phi\right) \tag{4.4a}$$

$$\frac{d\Gamma'}{d\theta_\ell} = \Gamma'\left(\frac{3}{4}F_{\rm L}\sin^2\theta_\ell + \frac{3}{8}(1-F_{\rm L})(1+\cos^2\theta_\ell) + A_{\rm FB}\cos\theta_\ell\right)\sin\theta_\ell \tag{4.4b}$$

$$\frac{d\Gamma'}{d\theta_{K^*}} = \frac{3\Gamma'}{4}\sin\theta_{K^*}\left(2F_{\rm L}\cos^2\theta_{K^*} + (1-F_{\rm L})\sin^2\theta_{K^*}\right) \tag{4.4c}$$

These differential widths were used as PDFs in the construction of three new RooFit models with the same physics and background treatment as that described in Sec. 4.1.1. Simultaneous fits to the three decay angles were performed in single bins of q^2 from $1-6\,{\rm GeV}^2/c^4$ to find rate weighted averages of each observable across the bin. Input data sets were generated as in Sec. 4.1.2. A reasonable comparison can be made between the full-angular and projection fit approaches by explicitly calculating the rate average over the q^2 range for each observable, A, using

$$\langle A\rangle = \frac{\int_{q^2_{\rm min}}^{q^2_{\rm max}} \frac{{\rm d}\Gamma}{{\rm d}q^2} A(q^2)}{\int_{q^2_{\rm min}}^{q^2_{\rm max}} \frac{{\rm d}\Gamma}{{\rm d}q^2}}, \tag{4.5}$$

where ${\rm d}\Gamma/{\rm d}q^2$ is extracted directly from the fit, as shown in Fig. 4.4d.

In Tab. 4.1 resolution estimates from an ensemble of a thousand fits are shown for both full-angular and projection fits. It can be seen that the full-angular approach provides a significant increase in experimental resolution for all observables considered. The difference in resolutions between the full-angular and projection fit approaches, shown in the table, is particularly significant for $A_T^{(2)}$. This arises from the $(1-F_{\rm L})$ suppression in Eq. (4.4a) where $F_{\rm L}$ is 0.86 ± 0.05 in the SM[5]. In contrast, $F_{\rm L}$ is well constrained in the projections and the full-angular fits do not significantly improve the resolutions attainable.

[5]Value from Ref. [1]. This can be contrasted with 0.76 ± 0.08 from Chap. 5, $0.73\,^{+0.08}_{-0.10}$ from Ref. [106], and 0.73 ± 0.12 from Ref. [111].

	Input	Projection		Full Angular		$\frac{(\hat{\sigma}_{\rm F}-\sigma_{\rm P})}{\sigma_{\rm P}}$
	$\langle A\rangle_{\rm I}$	$\langle A\rangle_{\rm P}$	$\sigma_{\rm P}$	$\langle A\rangle_{\rm F}$	$\sigma_{\rm F}$	%
$A_{\rm FB}$	0.036	0.0325	$\pm$0.0078	0.0344	$^{+0.0047}_{-0.0050}$	38
$A_{\rm Im}$	0.000	0.000	$\pm$0.015	0.0004	$^{+0.0060}_{-0.0057}$	61
$A_T^{(2)}$	-0.030	-0.03	$\pm$0.26	-0.043	$^{+0.095}_{-0.094}$	64
$F_{\rm L}$	0.865	0.8799	$\pm$0.0064	0.8582	$^{+0.0052}_{-0.0058}$	14

Table 4.1: Comparison between integrated values for the angular observables $A_{\rm FB}$, $A_{\rm Im}$, $A_T^{(2)}$ and $F_{\rm L}$ in the range $1 \leq q^2 \leq 6\,{\rm GeV}^2/c^4$ from an ensemble of a thousand $10\,{\rm fb}^{-1}$ LHCb data sets with averaged input values $\langle A\rangle_{\rm I}$. $\langle A\rangle_{\rm P,F}$ are the median values of the averages as calculated using Eq. (4.5), while $\sigma_{\rm P,F}$ are estimates of the 1σ uncertainty for both methods. The percentage resolution improvement offered by the full-angular analysis relative to the projection fit method is shown in the last column, where $\hat{\sigma}_{\rm F}$ is the mean of the asymmetric uncertainties for each observable.

4.3.2 The $A_{\rm FB}$ zero-crossing point

A comparison of the sensitivity to the $A_{\rm FB}$ zero-crossing point can also be found by following the methods of Ref. [112], but fitting the three angles simultaneously. In this case a thousand $10\,{\rm fb}^{-1}$ data sets were binned into five q^2 bins in the range $1 \leq q^2 \leq 6\,{\rm GeV}^2/c^4$, each with width of $1\,{\rm GeV}^2/c^4$. For each data set an independent simultaneous projection fit was performed in each of the q^2 bins and the resulting points fit to a straight line in the range $2 \leq q^2 \leq 6\,{\rm GeV}^2/c^4$ to extract the zero-crossing point. An example of this is shown in Fig. 4.5. The median zero-crossing found was $4.35^{+0.23}_{-0.24}\,{\rm GeV}^2/c^4$ for an input value of $4.39\,{\rm GeV}^2/c^4$. The quoted sensitivity is in reasonable agreement with that found in Ref. [112], although the two results are not directly comparable. Comparing now with the full-angular fit, we see a 28% improvement in the resolution relative to the projections result.

The value of $A_{\rm FB}$ at a given q^2 value is a quadratic function of the universal form factor $\xi_\perp$ [54], introduced in Sec. 3.4. Again, following [54], the q^2 dependence of the form factor can be parametrized as

$$\xi_\perp(q^2) = \xi_\perp(0)\left(\frac{1}{1-q^2/M_B^2}\right)^2, \tag{4.6}$$

where M_B is the mass of the $\overline{B}_d$ and $\xi_\perp(0)$ gives the normalization at $q^2 = 0$. This can be extracted from experiment by performing a fit to $\overline{B}_d \to \overline{K}^{*0}\gamma$ measurements or from QCD [54, 113]. At the zero-crossing point, these form factors cancel at LO, however the *particular* value of $\xi_\perp(0)$ used to generate the

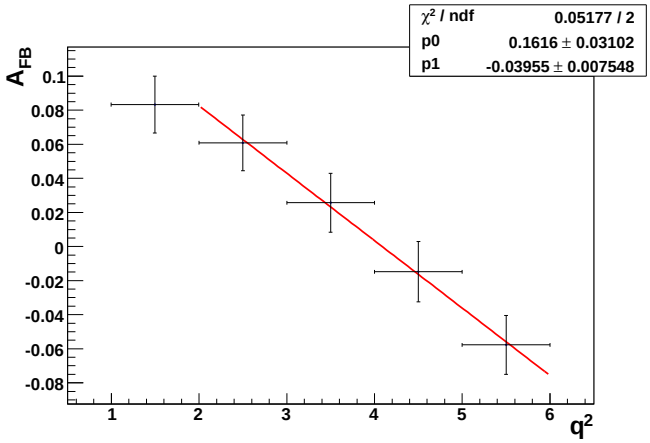

Figure 4.5: An example toy experiment in which an $A_{\rm FB}$ value has been extracted in five independent $1\,{\rm GeV}^2/c^4$ q^2 bins using a simultaneous projection fit to the three decay angles. The points show the $A_{\rm FB}$ value found for each q^2 bin and its error. The x error bar shows the width of the q^2 bin. The solid red line shows a fit to the linear function $y = p1\,x + p0$ in the range $2 \leq q^2 \leq 6\,{\rm GeV}^2/c^4$ as used in [112]. This allows a zero-crossing point of $q_0^2 = 4.09 \pm 0.21\,{\rm GeV}^2/c^4$ to be extracted for this particular experiment.

$A_{\rm FB}$ spectrum will affect the gradient of $A_{\rm FB}$ going through the zero-crossing point quadratically.

The experimental sensitivity for the zero-crossing point should be an approximately linear function of the $A_{\rm FB}$ gradient, so the value of $\xi_\perp(0)$, both in this study and in nature, strongly affects the experimental sensitivity to the zero-crossing point. The zero-crossing sensitivities we quote are extracted from toy input data where $\xi_\perp(0) = 0.26$, based on the updated value from [74]. This should be contrasted with the model used in [112] and based upon [69], which uses a value of $\xi_\perp(0) = 0.34$. If this value had instead been used in this study then an improvement in the zero-crossing resolution by a factor two would be expected. The observables $A_T^{(2-4)}$ are constructed to have no sensitivity to the form factors over the complete q^2 range under study and so no major change in their resolutions is expected as we vary $\xi_\perp(0)$.

4.4 New physics model discrimination

In this section the methods in Sec. 4.1 will be applied to a generic NP model with right-handed currents in order to demonstrate the discriminating power of the angular observables. Sensitivities to the observables introduced in Sec. 3.4 are extracted and compared to the SM theoretical distributions.

The NP model to be examined, SUSY-b, is a non-minimal flavour changing version of the MSSM with R-parity conservation, where the gluino mass is large,

$m_{\tilde{g}} = 1\,\text{TeV}$, the down squark mass is $m_{\tilde{d}} = 250\,\text{GeV}$ and there is a low value of $\tan\beta = 5$ [57]. In addition, there is a single insertion in the down squark mass matrix, parametrized by $(\delta^d_{LR})_{32} = 0.036$, which generates right-handed currents. The flavour diagonal parameters are fixed at $\mu = M_1 = M_2 = M_{H^+} = m_{\tilde{u}} = 1\,\text{TeV}$. It has been recently re-verified that this scenario is within current experimental and theoretical bounds [1].

This model has been chosen as it generates non-SM values of $C_7'^{\text{eff}}$; $(C_7^{\text{eff}}, C_7'^{\text{eff}}) = (-0.32, 0.24)$ which should be compared with the SM values of $(-0.31, 0.00)$. The observables A_{Im}, A_{FB} (and its zero-crossing) and F_{L} are not very sensitive to deviations in $C_7'^{\text{eff}}$ and so offer little discrimination power. However, $A_T^{(2)}$, $A_T^{(3)}$ and $A_T^{(4)}$ have been constructed in such as way as to maximize the sensitivity to this Wilson coefficient and hence allow better discrimination between SUSY-b and the SM.

Fig. 4.6 shows the comparison between the estimated sensitivities to SUSY-b, as extracted from an ensemble of a thousand $10\,\text{fb}^{-1}$ LHCb data sets and the SM theoretical distribution from Ref. [1] for $A_T^{(2)}$, $A_T^{(3)}$, $A_T^{(4)}$. The power of these observables is clear for observing non-SM values of $C_7'^{\text{eff}}$, particularly in the low q^2 region where the operator $\mathcal{O}_7^{(\prime)}$ dominates. Consideration of Fig. 3.3 suggests that a similar conclusion would be reached if a NP scenario with contributions in C_9^{eff} or $C_{10}^{(\prime)\,\text{eff}}$ had been studied. Due to the correlations along the band for both the theory and experimental curves, careful thought is needed to turn these measurements into a confidence level that the SM could be rejected if indeed nature turned out to be supersymmetric in the way modelled by SUSY-b. However, it seems clear that such a measurement could be of great interest if NP is discovered at the LHC.

Fig. 4.7 shows the same comparison for the angular observables A_{FB}, F_{L}, and A_{Im}. As expected, these observables offer poor sensitivity to C_7' across the entire q^2 range. F_{L} looks more promising than A_{FB} for this particular NP scenario, but is hindered by the large theoretical uncertainties on the SM prediction.

4.5 *CP*-violation

$\overline{B}_d \to \overline{K}^{*0}(\to K\pi)\mu^+\mu^-$ will be reconstructed in LHCb via charged decays of the $\overline{K}^{*0}$, allowing the flavour of the B meson to be identified using the sign of the K [8, 72]. Decays of this sort are known as self-tagging. As shown in Chap. 6, the phases of the Wilson coefficients are almost completely unconstrained by current experimental data. Any measurement of the CP-violation in $\overline{B}_d \to \overline{K}^{*0}\mu^+\mu^-$ would therefore reduce the parameter space available for NP, or provide a clear signal for it. The improved sensitivity that was shown for the full-angular analysis

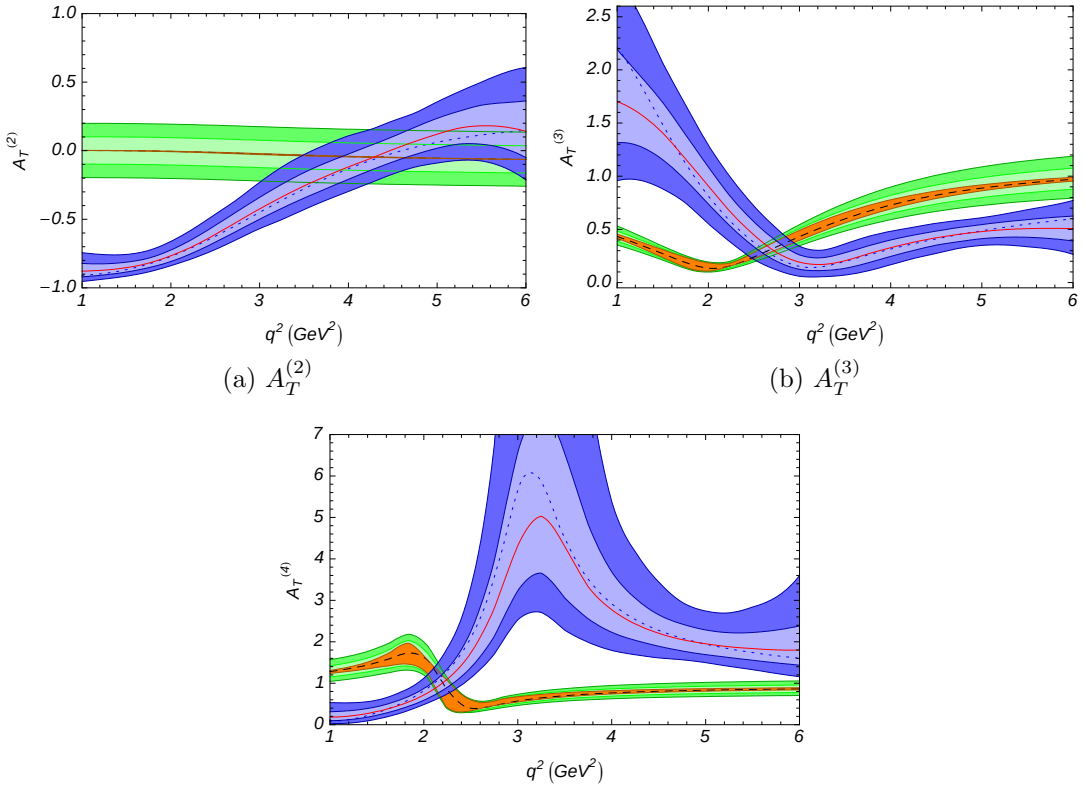

(a) $A_T^{(2)}$ (b) $A_T^{(3)}$

(c) $A_T^{(4)}$

Figure 4.6: Comparison between the estimated experimental sensitivities to $A_T^{(2)}$, $A_T^{(3)}$, $A_T^{(4)}$ and the theoretical SM distribution. The solid red line shows the median of values extracted from an ensemble of a thousand $10\,\mathrm{fb}^{-1}$ LHCb data sets where SUSY-b was used as the input model, shown as the dark-blue dotted line. The (light and dark blue) bands either side of the median show asymmetric 1 and 2 σ confidence levels as in Fig. 4.1. The SM theory bands are explained in more detail in Ref. [1]. The dashed (black) line is the SM central value, while the surrounding bands (orange, light green, dark green), are respectively the theoretical uncertainties excluding $\mathcal{O}(\Lambda/m_b)$ corrections, and those including 5% and 10% Λ/m_b corrections.

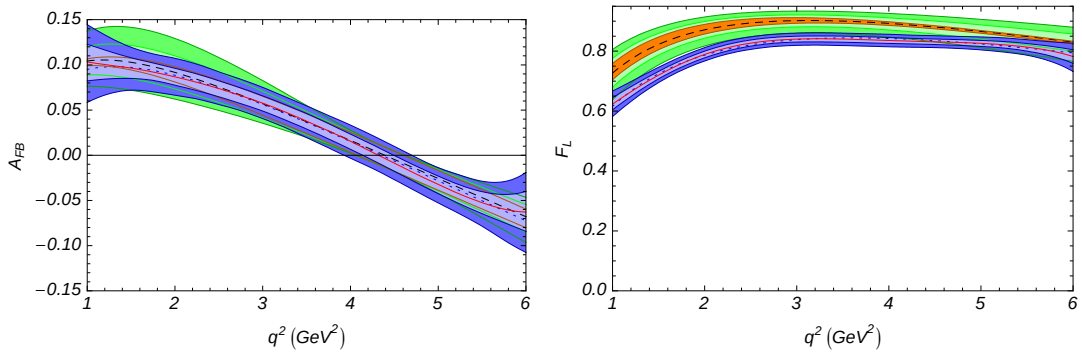

(a) A_{FB} (b) F_{L}

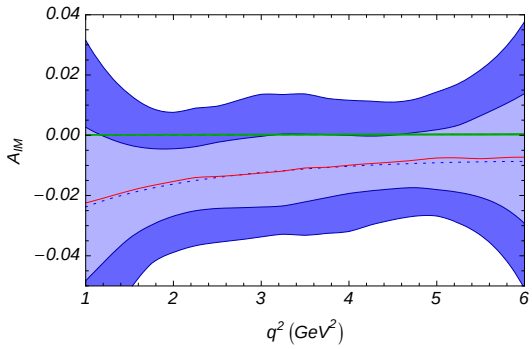

(c) A_{Im}

Figure 4.7: Comparison between the estimated experimental sensitivities to A_{FB}, F_{L}, and A_{Im} and the theoretical SM distribution. The colour scheme used is the same as in Fig. 4.6.

in Sec. 4.3 means that it could contribute to this programme significantly.

The methods described in Sec. 4.1 can be applied to get an estimate of the sensitivities to the *CP* asymmetries introduced in Sec. 3.5.4. The mis-identification of a $\overline{B}$ as a B in this channel will be very rare as it requires that both the K and π are reconstructed incorrectly. A full simulation study of the selection and backgrounds confirms this conclusion [8], although a specific mass veto must be employed to remove $B_s \to \phi\mu\mu$ decays. Thus, mis-id effects are neglected in this study. The SM amplitudes used for the toy model generation do not include the tiny *CP* violating contribution from $b \to d$ penguin decays so the *CP* asymmetries vanish in the MC. An ensemble of $\overline{B}$-only data sets was produced as in Sec. 4.1.2 for $10\,\text{fb}^{-1}$ of LHCb data, assuming the SM. Each data set was generated to have, on average, half the contents of those used in Sec. 4.1. A full-angular fit was then performed for each data set in the ensemble. An ensemble of B fits was also produced in the same way. These two statistically independent ensembles were then combined. The fits are only sensitive to the normalization of the spin amplitudes relative to the value of $\text{Re}(A_{0L})$ at X_0. When combining a B and a $\overline{B}$ fit result, the B result was re-normalized to correct for any differences between the two reference points.

Results are shown for the *CP*-asymmetries A_7 and A_9 in Fig. 4.8 for $10\,\text{fb}^{-1}$ of LHCb data, assuming the SM, but neglecting the *CP* violating terms [6]. A_7 and A_9 are respectively the rate weighted *CP* asymmetries of I_7 and I_9. The sensitivities found are good when compared to $A_T^{(2-4)}$ and suggest that large NP effects could be detected with these observables. A selection of NP distributions for A_7 are shown in Fig. 3.4. Full estimates of the theoretical uncertainties can be found in Refs [6, 56, 106], however the figure indicates the level of variation attainable. It is interesting to compare Fig. 4.8b with Fig. 4.4a, which shows the expected sensitivity to A_{Im}. This is the *CP*-average of I_9, and so is sensitive to the same terms in the full-angular distribution as A_9. Due to the self-tagging nature of the decay, the penalty required to extract *CP*-asymmetries rather than *CP*-averages is relatively small in this case. However, these measurements are unlikely to provide enough resolution for anything other than a SM null-test to be performed unless the NP phases are large.

4.6 The fourth symmetry

In order to extend this work to include the massive lepton terms in the angular distribution needed to gain sensitivity to scalar and pseudoscalar NP contributions, a more systematic analysis of Eq. (3.2) was undertaken [6]. This revealed the presence of a fourth symmetry in the massless leptons distribution unknown

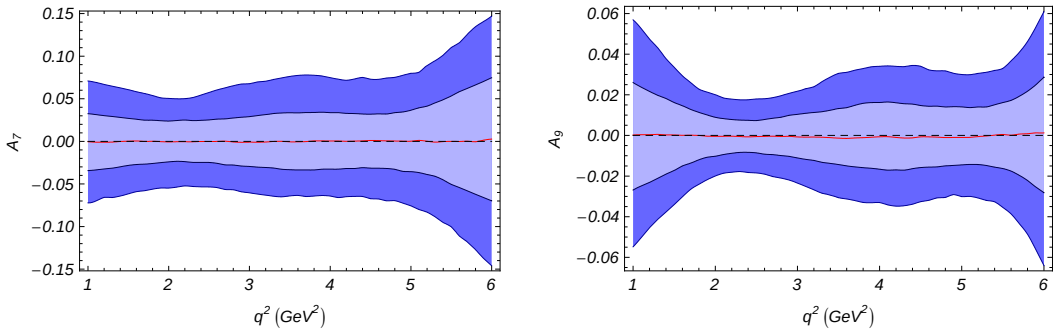

(a) A_7 (b) A_9

Figure 4.8: Estimated experimental sensitivities to the *CP* asymmetries A_7 and A_9 using a full-angular analysis with $10\,\text{fb}^{-1}$ of LHCb data. The SM is assumed, but the tiny $b \to d$ penguin contributions have been neglected. The colour scheme is the same as in Fig. 4.1.

at the time of writing Refs [1, 2][6]. This symmetry was first identified numerically and then Eq. (3.10) found. This implies that the constraint counting done in Sec. 4.1.1 was *incorrect*; there are only eight free parameters at each value of q^2, or seven once the normalization has been taken into account.

The rotation choices made in Sec. 4.1.1, along with the specific form of the symmetries, lead to the spin amplitude correlations seen in Fig. 4.1. The observables presented in Sec. 3.4 are invariant under all four symmetries meaning that the bias seen on the amplitudes does not lead to a bias on the observables. The fit, although *in principle* under-constrained, is able to converge due to the polynomial parametrization employed. Ignoring the normalization for a moment, we have four independent rotations which can be made at every point in q^2. Fixing the value of three spin amplitude components means that three of the rotation angles are also effectively fixed. The fourth rotation angle is free to vary. The negative log-likelihood (NLL) that each signal event contributes is conceptually invariant under changes in this angle. However, the q^2 dependent shape of each spin amplitude component is not. The polynomial ansatz requires that each amplitude must be smoothly varying. The fit then selects the value of the fourth rotation angle for each signal event which produces the most polynomial-like distribution, as this will have the smallest NLL. The minimizer is able to find a genuine minimum and converges properly. This leads to the prediction that adding the extra constraint implied by Eq. (3.10) should not significantly improve the experimental resolutions, but should reduce the degree of correlation seen in the fits.

[6]On which this chapter is based.

4.6.1 The polynomial ansatz re-examined

A key assumption of the fitting approach taken in Sec. 4.1 is that the spin amplitude components are smoothly varying functions in the range $q^2 \in [1, 6]\,\mathrm{GeV}^2/c^4$. It was found that when all four symmetries of the massless angular distribution are taken into account, this assumption *no longer holds*. The shape of the spin amplitude components is not invariant under the four symmetries; their shape can be distorted in such a way that they are no longer well described by 2^{nd} order polynomials. This can be understood qualitatively by considering the three symmetry case at a fixed q^2 value. A_{0R} is removed by setting $\theta = \arctan\left(-\mathrm{Re}(A_{0R})/\mathrm{Re}(A_{0L})\right)$, once their phases have been rotated away. This can be understood by substituting the trigonometric identities,

$$\sin(\arctan(\Theta)) = \frac{\Theta}{\sqrt{1+\Theta^2}}; \quad \cos(\arctan(\Theta)) = \frac{1}{\sqrt{1+\Theta^2}}. \tag{4.7}$$

into Eq. (3.9). This introduces a $[1 + (\mathrm{Re}(A_{0R})^2/\mathrm{Re}(A_{0L})^2)]^{-\frac{1}{2}}$ term into each non-zero amplitude component, which will not be well behaved as $A_{0L} \to 0$. For the three-symmetry fit, these problems can be avoided by taking $\mathrm{Re}(A_{0L})$ as the reference amplitude component, forcing it to be relatively large at X_0. To include the fourth symmetry constraint however, a more complicated form must be used in order to set four amplitude components simultaneously. A different value of each of the four rotation angles is required for every point in q^2 due to the changing spin amplitudes. There is no guarantee that a set of rotation angles can be found such that the unfixed spin amplitude components resemble smoothly varying polynomials for all q^2. The q^2 dependence of the SM input amplitude $\mathrm{Re}(A_{0L})$ is shown in Fig. 4.9 once the four symmetries have been applied to fix $\mathrm{Im}(A_{\parallel L})$, $\mathrm{Im}(A_{\parallel R})$, $\mathrm{Re}(A_{\parallel L})$, and $\mathrm{Im}(A_{\perp L})$ to zero, as required in the next section. This particular feature is caused by $\mathrm{Re}(A_{\parallel L}) \to 0$ at $q^2 \approx 2$, however other rotation choices led to similar features. The distribution can no longer be well described by a 2^{nd} order polynomial. It may be possible to find a choice of rotation parameters that preserve the polynomial features of the input spin amplitude components, however, there are no guarantee that a particular choice would work when faced with experimental data, particularly if we are looking for NP. Worse still, an incorrect choice will lead to biases in the case where the parametrization is a poor match for the underlying amplitudes. A more generic solution is required, but is beyond the scope of this thesis.

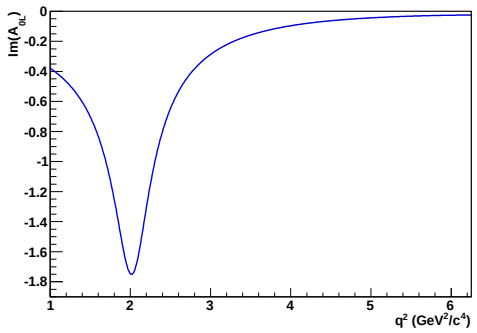

Figure 4.9: The q^2 dependence of $\mathrm{Im}(A_{0L})$ after using the four symmetries of the full-angular distribution to fix $\mathrm{Im}(A_{\parallel L})$, $\mathrm{Im}(A_{\parallel R})$, $\mathrm{Re}(A_{\parallel L})$, and $\mathrm{Im}(A_{\perp L})$ to zero.

4.6.2 Fit quality

The effect of adding the fourth symmetry constraint was tested, by comparing ensembles of three- and four-symmetry fits. The two ensembles were generated with the same random seed values so that the ensemble of input data sets was the same for the two approaches. To make the test more robust, the generation scheme described in Sec. 4.1.2 was modified so that data was produced with the full PDF, adding lepton mass effects. For completeness, doubly-Cabibbo penguin contributions and A_t were also included, and the signal and background estimates were updated to the most recent LHCb estimates [8]. To allow comparison with other parts of Ref. [6], the fixed spin amplitude components were chosen to be $\mathrm{Im}(A_{\parallel L})$, $\mathrm{Im}(A_{\parallel R})$, $\mathrm{Re}(A_{\parallel L})$, and in the case of the four symmetry fit also $\mathrm{Im}(A_{\perp L})$. The amplitudes were still normalized relative to $\mathrm{Re}(A_{0L})$ at $X_0 = 3.5\,\mathrm{GeV}^2/c^4$, however the fits were performed in the range $q^2 \in [2.5, 6]\,\mathrm{GeV}^2/c^4$ to avoid the non-polynomial features seen in the spin amplitude components, such as shown in Fig. 4.9.

The sensitivities found for the angular observables are much poorer than those presented in Sec. 4.1, due to the decreased signal statistics in the reduced q^2 window, however it is interesting to compare the performance of the two fitting methods. A histogram of the NLL of each fit is shown in Fig. 4.10a. The ensemble of three-symmetry fits (hatched) and four-symmetry fits (solid) can be seen. The ensemble of input data sets is slightly different in each case due to a small number of failed computing jobs, but the output distributions look very similar. This shows that the depth of the minima found is approximately the same for the three- and four-symmetry fits. We can also introduce a global correlation factor G_C, which is the unsigned mean of the individual global correlation coefficients calculated from the full covariance matrix. It takes values in the range $G_C \in [0, 1]$, where zero shows all variables as completely uncorrected, and one shows total fit

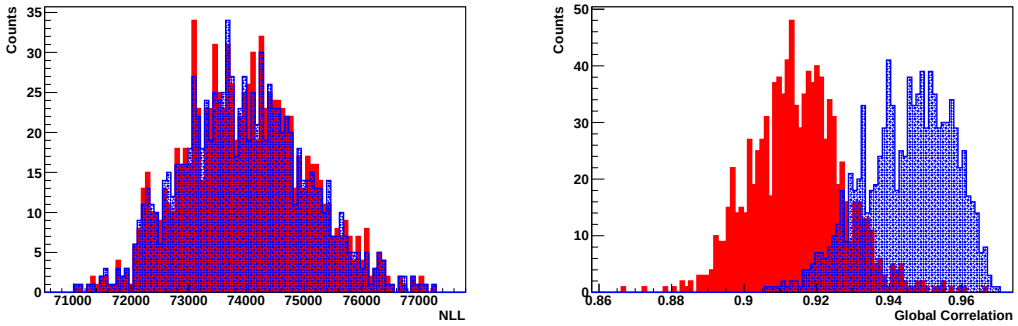

(a) NLL (b) G_C

Figure 4.10: The negative log-likelihood (a) and global correlation factor (b) for the three symmetry (blue hatched) and four symmetry (red solid) ensembles of fits to $10\,\text{fb}^{-1}$ toy data sets of LHCb data, assuming the SM and with $q^2 \in [2.5, 6]\,\text{GeV}^2/c^4$.

correlation. It can be seen that the mean correlation of the fit is reduced once the fourth symmetry is taken into account. There are less outliers at very low G_C and the distribution appears more Gaussian, indicating an increase in fit stability has been achieved. The mean number of refits required also fell from 6.9 ± 27.6 to 0.1 ± 1.4; the uncertainty quoted is the root-mean square (RMS) of the distribution.

Fig. 4.11 shows the estimated experimental sensitivities found for the theoretically clean observable $A_T^{(3)}$ in the range $q^2 \in [2.5, 6]\,\text{GeV}^2/c^4$, with and without the fourth symmetry constraint. The fits are for $10\,\text{fb}^{-1}$ of LHCb integrated luminosity assuming the SM. The quality metrics of these fits are shown in Fig. 4.10. As might be expected from Fig. 4.10a, there is little difference in the estimated experimental resolutions seen. The same conclusion is reached when inspecting other observables. We find that the three-symmetry fit presented in Sec. 4.1 probably provides a correct estimate of the statistical uncertainties that would be expected from a experimental analysis of $10\,\text{fb}^{-1}$ of LHCb data. However the discovery of the symmetry Eq. (3.10) and a re-analysis of Eq. (3.9) suggests that the fit must be reformulated if it is going to be robust in the presence of NP.

4.7 Summary and outlook

The full-angular fit for $\overline{B}_d \to \overline{K}^{*0}\mu^+\mu^-$ allows access to any arbitrary combination of the spin amplitudes as a function of q^2 in the region $1 \leq q^2 \leq 6\,\text{GeV}^2/c^4$. A set of angular observables can be constructed from these amplitudes which give LHCb great power to discover NP and to discriminate between models in a model independent way. In this chapter, several of these observables have been studied

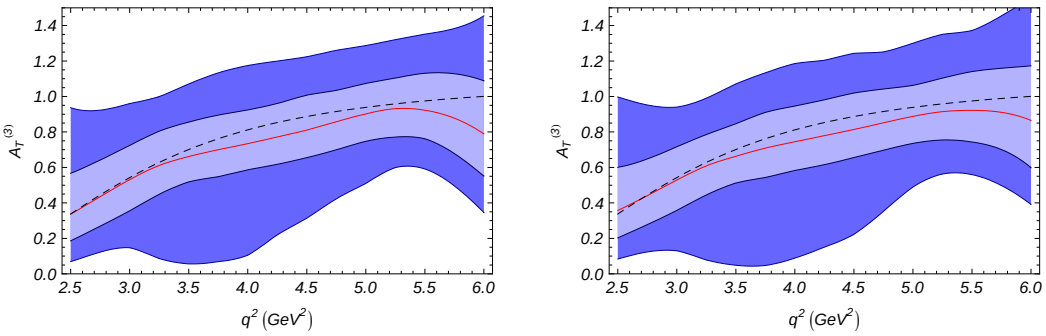

(a) 3 Symmetries (b) 4 Symmetries

Figure 4.11: One and two σ contours of estimated experimental sensitivity to the theoretically clean observable $A_T^{(3)}$ with full-angular fit to $10\,\text{fb}^{-1}$ of LHCb data assuming the SM. Fig. (a) has $\text{Im}(A_{\parallel L})$, $\text{Im}(A_{\parallel R})$, and $\text{Re}(A_{\parallel L})$ fixed at zero. In Fig. (b), the fourth symmetry is used to fix $\text{Im}(A_{\perp L})$ to zero also. The colour scheme is the same as in Fig. 4.1.

in order to estimate the experimental sensitivities at LHCb for 2, 10 and $100\,\text{fb}^{-1}$ data sets.

A full-angular analysis was constructed as a prototype for making the measurement. It has been shown that the analysis can both significantly improve the sensitivity to some observables assessable in other ways, as well as allow the determination of theoretically clean observables which can only be found via a full-angular analysis. A fit that was binned in q^2 was first tried, but found to be biased by the non-linear relationships between the K^{*0} spin amplitudes. This led to the development of a fit which used a polynomial parametrization to extract the q^2 dependence of the amplitudes. Despite correlations in the underlying amplitudes, unbiased measurements of the theoretically clean observables could be made. Estimated sensitivities for both the SM and a NP model were presented and it was shown that for larger integrated luminosities, these observables offer powerful discrimination in the case where $C_7'^{\text{eff}} \neq C_7'^{\text{eff SM}}$. The sensitivity to the CP-asymmetries A_7 and A_9 was also estimated. It was shown that there is scope to make an interesting and discriminating measurement if any NP found has large phases coming from outside of the CKM mechanism.

This work led to a systematic re-analysis of the $B_d \to K^{*0}\mu^+\mu^-$ angular distribution. A new symmetry was found, so demonstrating that the fits presented have been under-constrained in principle, although not in practise due to the polynomial parametrization. This extra symmetry constraint was incorporated into the fit and its implications studied. It was shown that the additional symmetry did little to improve fit quality, although it aided convergence. It did however warp the distribution of the spin amplitude components in such a way as to make the polynomial parametrization unworkable in the general case. A

new approach must be developed that incorporates the symmetry constraints in a more fundamental way. This will require study beyond the time-scale of this thesis.

Putting these methods into practise at LHCb will be a great technical challenge, and the success of the analysis will depend on our ability to understand the detector acceptance and the angular shapes of our backgrounds. This chapter has demonstrated that the sensitivity gained by performing the full angular analysis makes this a very interesting measurement to make at LHCb, and one that could potentially be done after a few years of stable running.

Chapter 5

A decay model of $B_d \to K^{*0}\mu^+\mu^-$

An important ingredient in most High Energy Physics (HEP) analyses is a detailed simulation of the detector response and underlying physics processes occurring during collisions. In this chapter, a new decay model of $B_d \to K^{*0}\mu^+\mu^-$ is presented [114]. The new model contains a state-of-the-art SM treatment as well as a model-independent parametrization of possible NP effects through its inclusion of operators suppressed or forbidden in the SM. Many more details may be found in Ref. [7].

5.1 Simulating physics events at the LHC

LHC events are complex, with many different particles present. A typical bunch-crossing simulation will start by determining the number and properties of the protons interacting by considering the beam parameters and machine optics. The individual interactions will then be simulated using a general purpose event generator such as those described in Refs [115, 116]. These generators are responsible for the production and decay of particles coming from the hard process as well as the treatment of the proton break-up. They use phenomenological models to reproduce the distributions observed in collider events, and are highly configurable.

The majority of particles produced in a simulated event are not the children of the particles created in the hard scatter but of quarks and gluons produced during the early stages of the interaction's evolution. These partons then hadronize to form the long-lived particles seen in detectors. Their production and hadronization is normally modelled using a parton shower. While many algorithms exist, the ones in common use today produce daughter particles which are kinematically but not spin correlated. Any interference effects seen in the decay of heavy

particles like b-quarks and τ-leptons are ignored. For a correct treatment of these effects we can turn to the dedicated decay simulator EvtGen [117, 118]. This can be used as a stand-alone generator or to handle the heavy particles created by the general purpose generators once a particular spin configuration has been chosen. The latter is the approach used within LHCb.

5.1.1 EvtGen

EvtGen is a framework for handling the decays of particles where the spin correlations are important. It provides a large library of generic matrix elements, while also supporting the inclusion of custom calculations for a particular decay. These calculations are known as decay models. It makes use of the spin-density framework (see Ref. [117]) in order to generate particle decays in a generic but relatively optimal way.

Particle decays are treated as a tree where each node is handled separately, however the correlations must still be propagated. The algorithm starts for example with a B meson of known momenta and energy. EvtGen has a large table listing all possible decays of each particle along with branching fractions for each mode. It can then choose at random which mode to use, or this can be specified by the user. As an example we take the decay $B \to D^*(\to D\pi)\tau(\to \pi\nu)\bar{\nu}$. The amplitude for this can be written as the spin-averaged product of the individual decays,

$$A = \sum_{\lambda_{D^*}\lambda_\tau} A^{B\to D^*\tau\bar{\nu}}_{\lambda_{D^*}\lambda_\tau} \times A^{D^*\to D\pi}_{\lambda_{D^*}} \times A^{\tau\to\pi\nu}_{\lambda_\tau}, \tag{5.1}$$

where λ_{τ,D^*} label the individual spin states of the τ and D^* and for example $A^{\tau\to\pi\nu}_{\lambda_\tau}$ gives the complex amplitude for the decay of $\tau \to \pi\nu$ for the spin state λ_τ. The algorithm treats each stage of the decay separately, starting from the B and working down the decay chain. A phase-space calculator is used to generate a random set of kinematics for the D^*, τ and $\bar{\nu}$. A semi-leptonic matrix element is used to calculate the amplitude $A^{B\to D^*\tau\bar{\nu}}$ for each D^* and τ spin configuration. The probability for a particular set of kinematics $\hat{x}$ is given by

$$P_B(\hat{x}) = \sum_{\lambda_{D^*}\lambda_\tau} |A^{B\to D^*\tau\bar{\nu}}_{\lambda_{D^*}\lambda_\tau}|^2. \tag{5.2}$$

$P_B(\hat{x})$ is rarely normalized to unity or easily integrable. In order to convert it into a normalized probability distribution an accept/reject algorithm is used. This requires that the maximum possible probability $P_B^{\max}$ can be found. $P_B(\hat{x})$ is then mapped on to the random uniform function, uniform$(0, 1)$. This is a PDF where the probability of drawing any value in the range $[0, 1]$ is equal, and zero

outside of this region. An event is accepted if $P_B(\hat{x})/\omega_{\rm ps} > P_B^{\rm max} \times \text{uniform}(0,1)$ and rejected otherwise. $\omega_{\rm ps}$ is used as a weight so that kinematically disfavoured events are kept more often, ensuring that these regions are still sampled.

Once a $B \to D^*\tau\bar{\nu}$ event has been accepted the momenta of the D^* and τ are known and the particles can be decayed, again starting from the relevant phase space distributions. The τ decay is performed with a specialized $\tau \to S\nu$ decay model where S is a scalar, while the D^* decay model is a generic vector to two scalar model which takes account of the quantum numbers of the system. The same `VSS` model is used to handle the $K^{*0} \to K\pi$ part of the decay of $B_d \to K^{*0}(\to K\pi)\mu^+\mu^-$.

The probabilities to be accepted or rejected must be weighted with the probability that the daughter particle is produced in a particular spin state. This is done with a spin-density matrix. Summing over the spin states of the τ we have for the D^*,

$$\rho^{D^*}_{\lambda_{D^*}\lambda'_{D^*}} = \sum_{\lambda_\tau} (A^{B\to D^*\tau\bar{\nu}}_{\lambda_{D^*}\lambda_\tau})(A^{B\to D^*\tau\bar{\nu}}_{\lambda'_{D^*}\lambda_\tau})^*, \tag{5.3}$$

the matrix of probability densities for each D^* spin state, labelled by λ_{D^*} and λ'_{D^*}. The probability to be used when accepting or rejecting a particular D^* momentum configuration is then

$$P^{D^*} = \frac{1}{\text{Tr}\rho^{D^*}} \sum_{\lambda_{D^*}\lambda'_{D^*}} \rho^{D^*}_{\lambda_{D^*}\lambda'_{D^*}} (A^{D^*\to D\pi}_{\lambda_{D^*}})(A^{D^*\to D\pi}_{\lambda'_{D^*}})^*, \tag{5.4}$$

where the trace term acts to re-normalize the probability without affecting the angular distribution.

Finally the τ has to be decayed. In order to get the spin correlations in the decay correct, spin-density matrices for both the $B \to D^*\tau\bar{\nu}$ and $D^* \to D\pi$ decay nodes must be considered. Combining these gives

$$\rho^{\tau}_{\lambda_\tau\lambda'_\tau} = \sum_{\lambda_{D^*}\lambda'_{D^*}} \left[(A^{D^*\to D\pi}_{\lambda_{D^*}})(A^{D^*\to D\pi}_{\lambda'_{D^*}})^*\right] \times \left[(A^{B\to D^*\tau\bar{\nu}}_{\lambda'_{D^*}\lambda_\tau})(A^{B\to D^*\tau\bar{\nu}}_{\lambda'_{D^*}\lambda_\tau})^*\right]. \tag{5.5}$$

The probability to be accepted or rejected can be easily obtained by making the replacement $D^* \to \tau$ in Eq. (5.4). This algorithm allows for efficient generation of large decay trees, as each node is accepted before the next one is considered. It also allows for many different decays to be simulated with a smaller set of models, as each one only needs to provide the spin-density matrix for one particular decay node, from which complex topologies can be built up.

5.2 The physics of $B_d \to K^{*0}\mu^+\mu^-$ decay

The EvtGen framework can be applied to simulate $B_d \to K^{*0}(\to K\pi)\mu^+\mu^-$ where a dedicated decay model is used to handle the $B_d \to K^{*0}\mu^+\mu^-$ part and the K^{*0} produced is then decayed separately. A decay model, `BTOSLLBALL`, based on Ref. [69] has been in use for some time at the B-factories and LHCb. This section describes the physics used in a replacement for this model, `BTOKSTARLLDURHAM07`. It is, to a close approximation, a complete implementation of Ref. [56]. A more complete theoretical description of the model may be found in Ref. [7].

5.2.1 Factorization

The decay $B_d \to K^{*0}\mu^+\mu^-$ is made possible by physics effects operating at the weak scale, where typical particle masses are $\mathcal{O}(m_W)$ and interaction times are very short. We expect any NP effects to be operating at these scales, however they must be detected via their effects on particles with masses far below this. Understanding the formation of these particles is then critical if robust predictions are to be made. It is this process to which QCDf is applied. In this framework, QCD effects arising from the decay of the heavy b quark are separated from those coming from other QCD processes. The former is dominated by hard gluons which may be treated with perturbative QCD, and the latter by soft collinear gluons which must be treated non-perturbatively. These two have distinct typical energy scales; the mass of the b quark, $m_b \sim 4.52\,\text{GeV}$, and the QCD scale $\Lambda_{\text{QCD}} \sim 0.22\,\text{GeV}$. This separation is broken by processes which operate at intermediate scales, however these can often be brought under theoretical control [64, 101, 102].

The $\overline{B}_d \to \overline{K}^{*0}\mu^+\mu^-$ decay proceeds via $b \to s$ quark loops such as the SM diagrams shown in Fig. 1.8. The treatment of this decay employed by all recent authors follows Refs [54, 74], however several updates have been made in Refs [55, 56] to include recent theoretical results and additional NP operators. A double expansion in the strong coupling constant, α_s, and the ratio Λ_{QCD}/m_b is used. This treatment is commonly classified as being NLO in α_s, as corrections proportional to α_s^2 are included, but only LO in $1/m_b$.

Starting from the effective Hamiltonian shown in Eq. (1.38), a decay amplitude may be derived. Schematically, this can be written as

$$\left\langle l^+l^-\overline{K}{}^{*0}_a|\mathcal{H}_{\text{eff}}|\overline{B}\right\rangle = \overbrace{\mathcal{C}_a^V\,\xi_a}^{\text{F}} + \underbrace{\Phi_B \otimes T_a \otimes \Phi_{K^{*0}}}_{\text{NF}} + \mathcal{O}(1/m_b), \tag{5.6}$$

where $a = \perp, \parallel$ labels the $\overline{K}^{*0}$ polarization as being transverse or longitudinal. The

symbol ξ_a refers to the *heavy-to-light* or *soft* form factors introduced in Chap. 3. These can be thought of as parameterizing the momentum dependence of the $\overline{K}^{*0}$ formation and are calculable using non-perturbative methods such as in Ref. [104]. They are, however, universal, low energy, and should be free from NP effects. These are weighted by a *hard vertex correction* factor, $\mathcal{C}_a^V = 1 + \mathcal{O}(\alpha_s)$. Together these determine the factorizable (F) contribution to the decay.

The second term is the non-factorizable part (NF), and groups those effects not included in the soft form factors. T_a is a process dependent hard-scattering kernel. This encodes the effects from short range, and so high mass scale, physics parametrized by the Wilson coefficients. However, other QCD effects must also be included. Finally, there are the process independent light-cone-distribution amplitudes Φ_B and $\Phi_{K^{*0}}$. These are non-perturbative, and control the probability of finding a valence quark in the $\overline{B}$ and K^{*0} with a given momentum fraction.

5.2.2 Wilson coefficients

The Wilson coefficients $\mathcal{C}_i(\mu)$ are process independent coupling constants for the basis of dimension-five effective vertices described by local operators $\mathcal{O}_i(\mu)$. They encode contributions to the effective vertices at scales above a particular renormalization scale μ. In the presence of NP their values will change from their SM values, and additional operators may become relevant. For more details see Chap. 1. Tab. 5.1 gives the values of the Wilson coefficients at $\mu = m_b$ in the SM, while Tab. 5.3 gives their modified values for a number of benchmark NP models included with the decay model.

The Wilson coefficients are calculated in the SM or other NP models by matching the full and effective theories at a matching scale m_W, the mass of the W boson. For the SM Wilson coefficients Next-to-Next-to-Leading Log (NNLL) accuracy is used, which requires the calculation of the matching conditions at $\mu = m_W$ to two-loop accuracy. This has been done in Ref. [53]. NP contributions are included to one-loop accuracy only; model independent corrections are not known but are expected to be small[1]. These coefficients must then be evolved down to the scale $\mu \sim m_b$. The evolution has been implemented using the full 10×10 anomalous dimension matrix following [58]. The primed operators are evolved as their unprimed equivalents, and the scalar and pseudoscalars do not require evolution as discussed in Ref. [56]. Finally, there is no sensitivity in either $\overline{B}_d \to \overline{K}^{*0}\mu^+\mu^-$ or any of the constraints considered in the next chapter to

[1]We know from experiment that the SM dominates. Any NP contribution is constrained to be small, and corrections to these contributions must be smaller still. A 10% correction on a 10% NP effect would normally be of negligible importance, unless very high precision experimental tests are available.

$\mathcal{C}_1(\mu)$	$\mathcal{C}_2(\mu)$	$\mathcal{C}_3(\mu)$	$\mathcal{C}_4(\mu)$	$\mathcal{C}_5(\mu)$	$\mathcal{C}_6(\mu)$	$C_7^{\text{eff}}(\mu)$	$C_8^{\text{eff}}(\mu)$	$\Delta C_9^{\text{eff}}(\mu)$	$C_{10}^{\text{eff}}(\mu)$
-0.135	1.054	0.012	-0.033	0.009	-0.039	-0.306	-0.159	4.220	-4.093

Table 5.1: SM Wilson coefficients at $\mu = m_{b,\text{PS}}(2\,\text{GeV}/c^2) = 4.52\,\text{GeV}/c^2$. $\Delta C_9^{\text{eff}}(\mu) \equiv C_9^{\text{eff}}(\mu) - Y(q^2)$.

separate $\mathcal{C}_{S,P}$ from $\mathcal{C}'_{S,P}$. They are combined as ($\mathcal{C}_S$-$\mathcal{C}'_S$) and ($\mathcal{C}_P$-$\mathcal{C}'_P$).

5.2.3 Decay amplitudes

EvtGen requires the calculation of the spin-amplitude $A^{\overline{B}_d \to \overline{K}^{*0}\mu^+\mu^-}$. For each allowed spin state, the amplitude to be calculated, following the notation in Refs [69, 119] for ease of comparison with the previous decay model, is

$$\mathcal{M} \propto \left[\mathcal{T}_\mu^1\,(\bar{\mu}\,\gamma^\mu\,\mu) + \mathcal{T}_\mu^2\,(\bar{\mu}\,\gamma^\mu\gamma_5\,\mu) + \mathcal{S}(\bar{\mu}\,\mu)\right] \tag{5.7a}$$

where

$$\mathcal{T}_\mu^1 = A(q^2)\epsilon_{\mu\rho\alpha\beta}\epsilon^{*\rho}\,\hat{p}_B^\alpha\,\hat{p}_{K^*}^\beta - iB(q^2)\,\epsilon_\mu^* + iC(q^2)(\epsilon^*\cdot\hat{p}_B)\,\hat{p}_\mu + iD(q^2)(\epsilon^*\cdot\hat{p}_B)\,\hat{q}_\mu \tag{5.7b}$$

$$\mathcal{T}_\mu^2 = E(q^2)\epsilon_{\mu\rho\alpha\beta}\,\epsilon^{*\rho}\hat{p}_B^\alpha\,\hat{p}_{K^*}^\beta - iF(q^2)\,\epsilon_\mu^* + iG(q^2)(\epsilon^*\cdot\hat{p}_B)\,\hat{p}_\mu + iH(q^2)(\epsilon^*\cdot\hat{p}_B)\,\hat{q}_\mu \tag{5.7c}$$

and

$$\mathcal{S} = i2\hat{m}_{K^*}(\epsilon^*\cdot\hat{p}_B)\,I(q^2). \tag{5.7d}$$

In the rest-frame of the B meson, $p_{B,K^{*0}}$ and $m_{B,K^{*0}}$ are the four-vectors and masses of the respective particles, $p \equiv p_B + p_{K^{*0}}$, q is the invariant mass of the μ pair and ϵ_μ^* is the K^{*0} polarization vector. Each of these is represented by a dedicated EvtGen object which implements the appropriate algebraic operations. Adding a hat denotes division by m_B, so for example $\hat{m}_{K^{*0}} \equiv m_{K^{*0}}/m_B$. The functions $A(q^2)$ to $I(q^2)$, defined below, contain all theoretical information via the Wilson coefficients and the $P \to V^2$ form factors V, $A_{0,1,2}$, and $T_{1,2,3}$ (see for example [104]). For the conjugate $B_d \to K^{*0}\mu^+\mu^-$ decay,

$$\bar{A}(q^2) \to -A(q^2); \quad \bar{E}(q^2) \to -E(q^2), \tag{5.8}$$

[2] Pseudoscalar→ Vector

while the other auxiliary functions remain unchanged (see Eq. (3.5)). The terms $\left(\bar{l}\gamma^\mu l\right)$, $\left(\bar{l}\gamma^\mu\gamma_5 l\right)$ and $(\bar{l}l)$ refer to the vector, axial and scalar lepton currents respectively, through which the lepton spins are included.

The auxiliary functions have been updated to include the additional operators $\mathcal{O}'_{7-10}$ and $\mathcal{O}^{(\prime)}_{S,P}$. QCDf corrections are also included through the functions $\mathcal{T}_\parallel^{\rm NLO}(q^2)$ and $\mathcal{T}_\perp^{\rm NLO}(q^2)$. These are similar to $\mathcal{T}_\parallel(q^2)$ and $\mathcal{T}_\perp(q^2)$ defined in [54], but neglect the factorizable corrections and numerically small weak-annihilation diagrams derived in that reference. The corrections to the helicity suppressed operators are also included. We define $\mathcal{T}_\parallel'^{\rm NLO}(q^2)$ and $\mathcal{T}_\perp'^{\rm NLO}(q^2)$ as the analogous functions to $\mathcal{T}_\parallel^{\rm NLO}(q^2)$ and $\mathcal{T}_\perp^{\rm NLO}(q^2)$ with all Wilson coefficients replaced by their primed equivalents. The factorizable corrections arise from expressing the full form factors, V, $A_{0,1,2}$, and $T_{1,2,3}$ in terms of the soft form factors, $\xi_{\perp,\parallel}$. Following Ref. [56], the LO results are expressed in terms of the full QCD form factors, automatically including these factorizable corrections from the form factor calculation.

$$\begin{aligned}
A(q^2) =& \frac{2}{1+\hat{m}_{K^*}}(C_9^{\rm eff}+C_9'^{\rm eff})V(q^2)+\frac{4\hat{m}_b}{\hat{q}^2}\Bigg((C_7^{\rm eff}+C_7'^{\rm eff})T_1(q^2)\\
&+\mathcal{T}_\perp^{\rm NLO}(q^2)+\mathcal{T}_\perp'^{\rm NLO}(q^2)\Bigg); && \text{(5.9a)}\\
B(q^2) =& (1+\hat{m}_{K^*})\Bigg\{(C_9^{\rm eff}-C_9'^{\rm eff})A_1(q^2)+\frac{2\hat{m}_b}{\hat{q}^2}(1-\hat{m}_{K^*})\Bigg((C_7^{\rm eff}-C_7'^{\rm eff})T_2(q^2)\\
&+2\hat{E}_{K^*}(q^2)(\mathcal{T}_\perp^{\rm NLO}(q^2)-\mathcal{T}_\perp'^{\rm NLO}(q^2))\Bigg)\Bigg\}; && \text{(5.9b)}\\
C(q^2) =& \frac{1}{1-\hat{m}_{K^*}^2}\Bigg\{(1-\hat{m}_{K^*})(C_9^{\rm eff}-C_9'^{\rm eff})A_2(q^2)\\
&+2\hat{m}_b\Bigg((C_7^{\rm eff}-C_7'^{\rm eff})(T_3(q^2)+\frac{1-\hat{m}_{K^*}^2}{\hat{q}^2}T_2(q^2))\\
&+(1+\frac{(1-\hat{m}_{K^*}^2)\,2\hat{E}_{K^*}(q^2)}{\hat{q}^2})(\mathcal{T}_\perp^{\rm NLO}(q^2)-\mathcal{T}_\perp'^{\rm NLO}(q^2))\\
&+\mathcal{T}_\parallel^{\rm NLO}(q^2)-\mathcal{T}_\parallel'^{\rm NLO}(q^2)\Bigg)\Bigg\}; && \text{(5.9c)}\\
E(q^2) =& \frac{2}{(1+\hat{m}_{K^*})}(C_{10}^{\rm eff}+C_{10}'^{\rm eff})V(q^2); && \text{(5.9d)}\\
F(q^2) =& (1+\hat{m}_{K^*})(C_{10}^{\rm eff}-C_{10}'^{\rm eff})A_1(q^2); && \text{(5.9e)}\\
G(q^2) =& (C_{10}^{\rm eff}-C_{10}'^{\rm eff})\frac{A_2(q^2)}{(1+\hat{m}_{K^*})}; && \text{(5.9f)}\\
H(q^2) =& \frac{1}{\hat{q}^2}(C_{10}^{\rm eff}-C_{10}'^{\rm eff})\Bigg((1+\hat{m}_{K^*})A_1(q^2)-(1-\hat{m}_{K^*})A_2(q^2)\\
&-2\hat{m}_{K^*}A_0(q^2)\Bigg)-\frac{\hat{m}_{K^*}m_B}{2\hat{m}_\mu}A_0(q^2)(\mathcal{C}_P-\mathcal{C}'_P); && \text{(5.9g)}
\end{aligned}$$

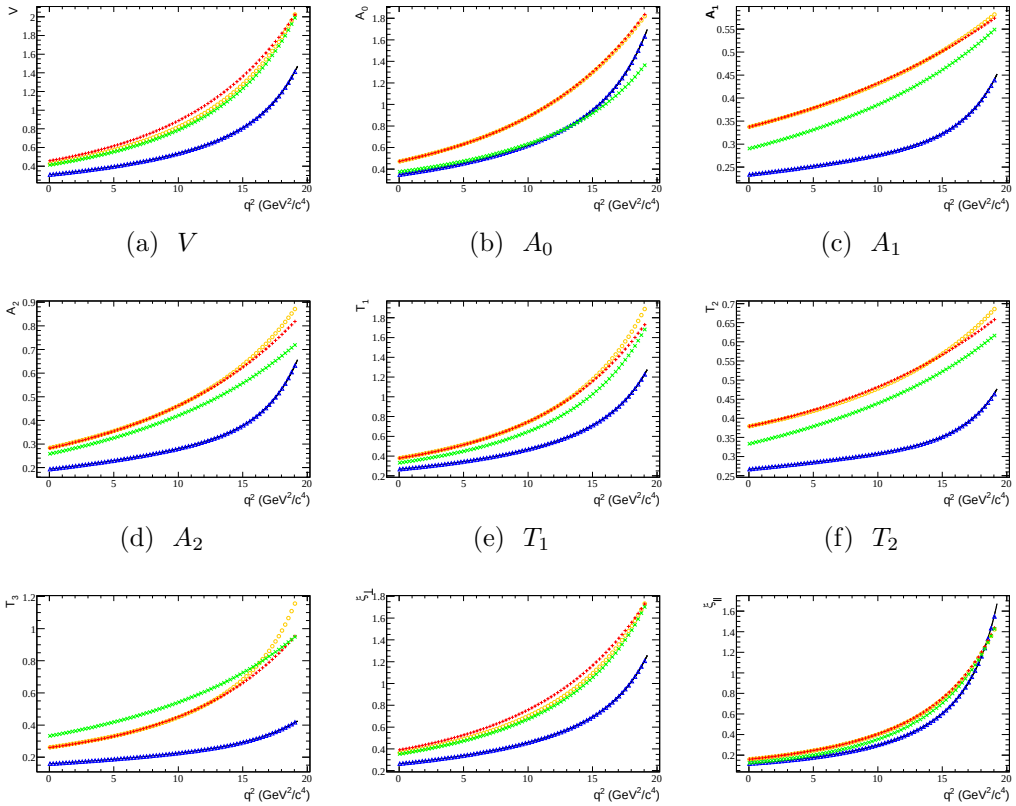

(a) V (b) A_0 (c) A_1

(d) A_2 (e) T_1 (f) T_2

(g) T_3 (h) $\xi_\perp$ (i) $\xi_\parallel$

Figure 5.1: Comparison between the form factor models shown in Tab. B.2. The (blue) triangles, (red) pluses, (green) crosses and (orange) circles show respectively the Ball '07 [120], Ali '01 [69], Ball '05 [104], and Beneke '05 [74, 113] models. The solid (black) line shows the full unparameterized Ball '07 calculation. These figures can be compared with Fig. 1 of Ref. [56], which uses a very similar calculation.

$$I(q^2) = -A_0(q^2)(\mathcal{C}_S - \mathcal{C}'_S). \tag{5.9h}$$

5.2.4 Form factors

The default form factor model 'Ball '07' was implemented as a full Light Cone Sum Rules (LCSR) calculation in MATHEMATICA 6.0 [120]. This has been parametrized, following Ref. [69], as a exponentiated polynomial. To achieve agreement between the parameterization and the full calculation at the sub-percent level the polynomial has been extended to higher order than used in that reference,

$$F(q^2) = F(0) \exp\left(\sum_{i=1}^{6} C_i \hat{s}^i\right). \tag{5.10}$$

$F(0)$, and C_{1-6} are free parameters to be extracted via a fit to the full calculation and $\hat{s} \equiv q^2/m_B^2$. The fitted values are listed in Tab. 5.2, while a comparison

Form factor	$F(0)$	C_1	C_2	C_3	C_4	C_5	C_6	$\delta(\%)$
V	0.31	1.24	0.78	−0.11	−0.16	1.00	2.22	0.05
A_0	0.35	1.31	0.79	−0.07	−0.16	0.81	2.10	0.05
A_1	0.23	0.37	0.28	−0.12	−0.34	0.32	3.07	0.05
A_2	0.19	0.89	0.44	−0.38	−0.31	1.42	3.39	0.03
T_1	0.27	1.26	0.82	−0.15	−0.19	1.15	1.94	0.05
T_2	0.27	0.33	0.20	−0.14	−0.29	0.34	2.82	0.06
T_3	0.16	0.89	0.20	−0.20	0.42	1.41	0.30	0.04
$\xi_\parallel$	0.12	2.05	1.16	2.07	−3.06	−1.57	8.72	0.18
$\xi_\perp$	0.26	1.24	0.81	−0.15	−0.19	1.16	2.09	0.05

Table 5.2: Form factor parameters, as extracted from a fit to Eq. (5.10), of the full Ball '07 calculation.

between the parameterization and the original calculation is shown in Fig. 5.1. To access the fit quality we use the metric

$$\delta = 100\% \times \frac{\sum_t f(t) - f^{\text{fit}}(t)}{\sum_t |f(t)|}, \tag{5.11}$$

where $f(t)$ is the result from the full calculation, $f^{\text{fit}}(t)$ is the result from the fit, and t is the value of q^2 over the range $t \in \{0, 14\}\,\text{GeV}^2/c^4$ in steps of $0.5\,\text{GeV}^2/c^4$ as in Ref. [104]. The goodness of fit as a function of q^2 can be seen in Fig. 5.2, as explained in the caption. The full calculation is reproduced to one percent over most of the kinematic range. The parametrization performs most poorly for $\xi_\perp$, however it was found that going to even higher orders in the polynomial led to oscillation in the shape. The failure to reproduce this form factor distribution is one of the largest sources of numerical discrepancy between the C++ and MATHEMATICA versions of the model. While other parametrizations from Ref. [104] and their higher-order extensions were evaluated, none outperformed Eq. (5.10) and so were not adopted. A number of other form factor models are provided for comparison, and these are also shown in Fig. 5.1. Details can be found in Tab. B.2. These may be of interest for some analyses where the q^2 dependence of observables is important, however, the parameters used in these models are often not compatible with current Particle Data Group (PDG) values [41].

5.2.5 New physics models

A number of benchmark NP models have been included to enable the study of experimental effects arising from the presence of beyond-the-SM physics. The decay model is implemented model independently. New models can thus be in-

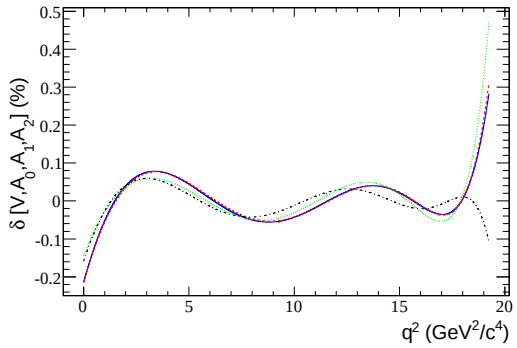

(a) $V, A_{0,1,2}$

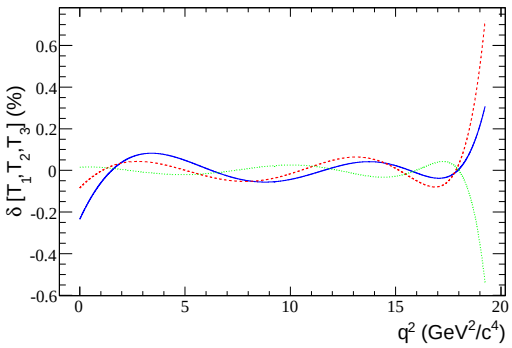

(b) $T_{1,2,3}$

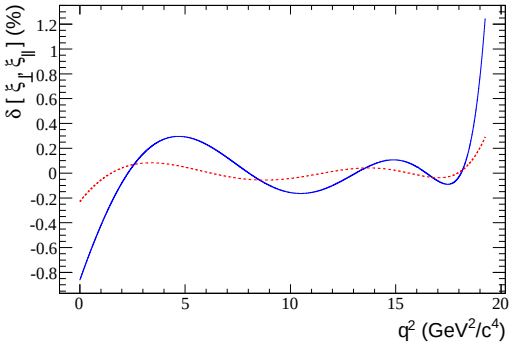

(c) $\xi_{\perp,\parallel}$

Figure 5.2: Form factor fit quality as a function of q^2 over the entire kinematic range. Fig. (a) shows the fit quality $\delta(q^2)$ metric, which is the value of Eq. (5.11) at a given value of $t = q^2$, for V, A_0, A_1 and A_2 shown as solid (blue), dashed (red), dotted (green) and dash-dotted (black) lines respectively. Fig. (b) shows T_1, T_2 and T_3 as solid (blue), dashed (red), and dotted (green) lines while Fig. (c) shows $\xi_\perp$, $\xi_\parallel$ as solid (blue) and dashed (red).

cluded as an additional table of Wilson coefficients or via the EvtGen decay file, as described in Appendix B.1. Some benchmark models are listed below. The effective Wilson coefficients for each model are shown in Tab. 5.3.

- **Universal Extra Dimensions (UED):** This model suggests that all SM particles can propagate freely in additional spatial dimensions [121]. In order to respect existing experimental constraints on $\mathcal{B}(B_s \to \mu^+\mu^-)$ [122], the compactification scale $1/R = 400\,\mathrm{GeV}/c^2$ is adopted; otherwise the treatment is as in Ref. [71].

- **Flavour Blind MSSM (FBMSSM):** Here the Minimal Flavour Violation (MFV) version of the MSSM is modified by some flavour conserving but *CP*-violating phases in the soft Supersymmetry (SUSY) breaking terms [123]. The Wilson coefficients used, [124], correspond to those calculated in scenario FBMSSM II defined in Tab. 11 of Ref. [56].

- **General MSSM (GMSSM):** MFV is not imposed, and generic flavour- and *CP*-violating soft SUSY-breaking terms are allowed [125]. The Wilson coefficients used, [124], are similar those used in the scenario GMSSM IV of Ref. [56].

- **Littlest Higgs with *T*-Parity (LHT):** The LHT model follows model II from Ref. [56], however the phenomenology is such that the effects in $\overline{B}_d \to \overline{K}^{*0}\mu^+\mu^-$ are very limited. It is included for completeness.

In order to allow for a more global view of $b \to s$ transitions, detailed calculations for a number of related experimental observables are included with the model. Definitions, calculation details and SM uncertainties are included in Sec. 6.6. However, their value for the benchmark models is shown in Tab. 5.4.

5.2.6 Validity

It is accepted that the assumptions required to use the QCDf framework for $\overline{B}_d \to \overline{K}^{*0}\mu^+\mu^-$ only hold in the q^2 region from $1\,\mathrm{GeV}^2/c^4$ to $6\,\mathrm{GeV}^2/c^4$. This is discussed in a number of references including [1, 56]. At low q^2, the decay is dominated by the photon diagrams which give rise to the $B \to K^{*0}\gamma$ decay. This *photon pole* is visible in Fig. 5.4a. There may be unknown resonances which will spoil factorization as long-range effects become important. The same is true as q^2 gets closer to the charm resonance at $4m_c^2$. The upper limit of $6\,\mathrm{GeV}^2/c^4$ is thought to be far enough away from this point that these effects can be neglected. While there are some attempts in the literature to include resonance effects from ρ, ω and $c\bar{c}$ [126], it is not clear that studying these contributions in $\overline{B}_d \to \overline{K}^{*0}\mu^+\mu^-$

	Model				
	SM	FBMSSM	GMSSM	LHT	UED
$C_7^{\text{eff}}(\mu)$	-0.306	$0.031 + 0.475i$	$-0.186 + 0.002i$	$-0.308 - 0.001i$	-0.297
$C_8^{\text{eff}}(\mu)$	-0.159	$-0.085 + 0.149i$	$-0.062 + 0.004i$	-0.159	-0.137
$\Delta C_9^{\text{eff}}(\mu)$	4.220	4.257	4.231	$4.295 + 0.006i$	4.230
$C_{10}^{\text{eff}}(\mu)$	-4.093	-4.063	-4.241	$-4.566 - 0.040i$	-4.212
$C_7'^{\text{eff}}(\mu)$	-0.007	$0.008 + 0.003i$	$0.155 + 0.160i$	-0.007	-0.007
$C_8'^{\text{eff}}(\mu)$	-0.004	$-0.000 + 0.001i$	$0.330 + 0.336i$	-0.004	-0.003
$C_9'^{\text{eff}}(\mu)$		0.002	$0.018 + 0.018i$		
$C_{10}'^{\text{eff}}(\mu)$		0.004	$0.003 + 0.003i$		
$(\mathcal{C}_S - \mathcal{C}_S')(\mu)$		$-0.044 - 0.056i$	$0.000 + 0.001i$		
$(\mathcal{C}_P - \mathcal{C}_P')(\mu)$		$0.043 + 0.054i$	$0.001 + 0.001i$		

Table 5.3: NP Wilson coefficients at $\mu = m_{b,\text{PS}}(2\,\text{GeV}/c^2) = 4.52\,\text{GeV}/c^2$.

Observable	Model				SM Error
	SM	FBMSSM	GMSSM	UED	
$\mathcal{B}(B_s \to \mu\mu) \times 10^9$	3.70	34.0	3.79	3.92	± 0.31
$\mathcal{B}(B_d \to X_s\gamma) \times 10^4$	3.28	3.28	3.05	3.13	± 0.25
$\mathcal{B}(B_d \to X_s l^+ l^-)_{1-6\,\text{GeV}^2} \times 10^6$	1.97	3.23	2.19	2.05	± 0.11
$\mathcal{S}_{CP}(B_d \to K^{*0}\gamma) \times 10^2$	-2.6	-3.0	4.9	-2.6	± 0.5
$q_0^2(S_5)$	2.37		0.57	2.30	± 0.11
$q_0^2(A_{\text{FB}})$	4.03	0.63	2.73	3.92	± 0.15
$\langle A_{\text{FB}} \rangle_{1-6\,\text{GeV}^2}$	0.04	-0.12	-0.05	0.03	± 0.03
$\langle F_{\text{L}} \rangle_{1-6\,\text{GeV}^2}$	0.76	0.56	0.70	0.76	± 0.08
$\langle S_5 \rangle_{1-6\,\text{GeV}^2}$	-0.11	-0.28	-0.34	-0.12	± 0.03

Table 5.4: Predictions for $b \to s$ observables for the benchmark NP physics models.

gives new information when compared to other more abundant channels. These effects are not included in the present decay model as other models included in EvtGen are better suited for these resonance regions.

The QCD form factors used may be applied over a wider q^2 range than that specified above. In Ref. [104], the $B \to K^{*0}$ form factors are presented in the range $q^2 \in [0, 14]\,\mathrm{GeV}^2/c^4$. As the Wilson coefficients are not q^2 dependent, the model may have some relevance above the charm resonances. However there are few theoretical results in this region with which to compare. QCD corrections are relatively small so the behaviour will be similar to the previous `BTOSLLBALL` model. Simulations done with either model will be unreliable in this region. However, the model will simulate signal events over the entire kinematic q^2 range as required for LHCb MC production.

5.3 Implementation

The decay model is a full implementation of the theoretical treatment introduced in Sec. 5.2. It was first prototyped with Mathematica, and then translated into C++ for inclusion in EvtGen. This two step process was important to guarantee numerical correctness; the process of cross-checking the C++ model identified numerous problems with the Mathematica version and *vice-versa*. The final versions of both models were in agreement to one percent for a wide range of q^2 values. The main source of differences was in the form factor parametrizations, as discussed in Sec. 5.2.4. For this to be achieved, it was necessary to make extensive usage of numerical routines provided in both the EvtGen framework and the GNU Scientific Library [110]. Most stages of the calculation were required to be undertaken using complex numbers, even if the input and outputs were real. In addition, each spin-amplitude calculation requires four numerical integrals to calculate contributions to $\mathcal{T}_\perp^{(\prime)\mathrm{NLO}}(q^2)$ and $\mathcal{T}_\parallel^{(\prime)\mathrm{NLO}}(q^2)$ at NLO. As one of the design requirements was that additional NP models could be easily added, these integrals are computed numerically during the decay amplitude calculation. These factors makes the full calculation significantly slower than the previous `BTOSLLBALL` model.

5.3.1 Performance

One requirement for the model was that it must be significantly faster to run than the detailed detector simulation used within LHCb to produce MC signal samples. Due to the accept/reject architecture of EvtGen, some events take longer to generate than others depending on the region of parameter space they

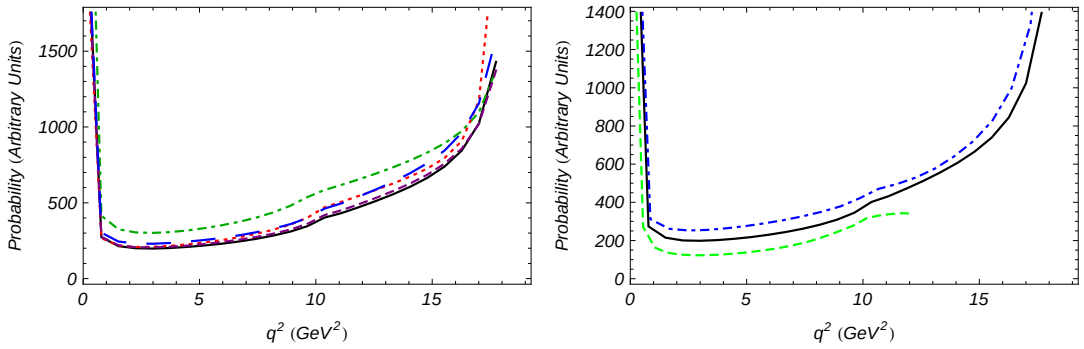

(a) SM & NP Central Values (b) SM K^{*0} mass effects

Figure 5.3: Fig. (a) shows the unnormalized decay probability for $\overline{B}_d \to \overline{K}^{*0}\mu^+\mu^-$ for the SM (solid black), FBMSSM (dot-dash green), GMSSM (dotted red), UED (dashed purple) and, LHT (long-dashed blue). The poles at high and low q^2 can be seen. Fig. (b) shows the same unnormalized probability distribution for the SM for three values of the K^{*0} mass. These are $m_{K^{*0}} = m_{K^{*0}}^{\rm PDG}$ (solid black), $m_{K^{*0}} = m_{K^{*0}}^{\rm min}$ (dot-dashed blue) and, $m_{K^{*0}} = m_{K^{*0}}^{\rm max}$ (dashed green).

sample. As many signal events are typically produced in a single batch, the important metric is the mean time to decay an event. The presence of very long tails in the decay time distribution must be avoided.

When testing the model it was found that a very long tail was indeed present. As explained in Sec. 5.1.1, the accept/reject algorithm used in EvtGen maps the probability distribution encoded in the decay amplitudes into the uniform distribution. One consequence of this is that the probability to accept a given event scales with $1/P^{\rm max}$, the maximum probability that can be produced by the decay model. This is not known *a priori* and so is calculated during initialization by scanning the allowed regions of q^2 with three different values of the K^{*0} mass, $m_{K^{*0}}^{\rm PDG}$, $m_{K^{*0}}^{\rm min}$, and $m_{K^{*0}}^{\rm max}$, where the latter two extremes are fifteen times the K^{*0} natural width away from the nominal PDG mass. The probability profiles generated by the decay model are shown in Fig. 5.3. The probability is highly asymptotic at large values of q^2. This is mainly due to the form factors, shown in Fig. 5.1, which increase sharply as q^2 goes to its kinematic maximum. This behaviour was seen to be particularly extreme in the GMSSM, which featured $P^{\rm max}$ values of $\mathcal{O}(10^5)$. Such large values are probably not physically meaningful, as the calculation is being applied a long way from the region in q^2 for which it is valid. At the same time however, the phase space to actually produce a K^{*0} is decreasing; it must be produced approximately at rest. Events with high q^2 have a large decay probability, but a small phase space left to decay into. The result of these competing effects can be seen in Fig. 5.4a which shows the generated q^2 distribution. The number of generated events above a q^2 of $18\,{\rm GeV}^2/c^4$ rapidly falls off, however, there is a distinct pole starting at this point. It was found that

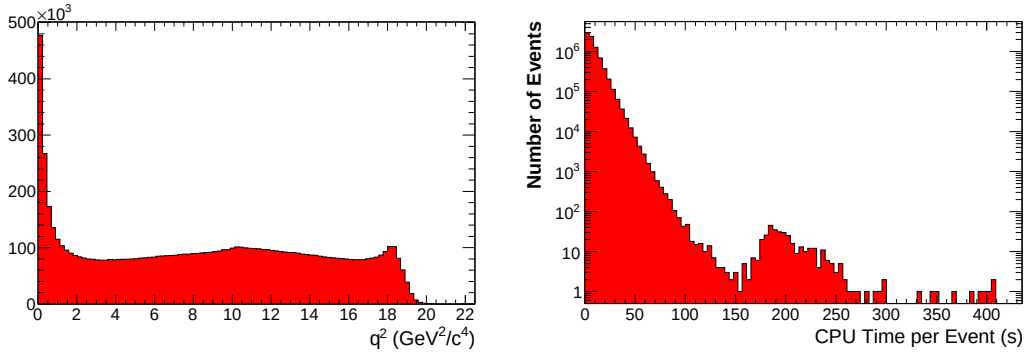

(a) q^2 (b) Generation time

Figure 5.4: Fig. (a) shows the generated q^2 distribution for the SM. Fig. (b) shows the CPU time to generate a SM signal event. The mean generation time over 8M signal events was 8.2 s.

the mean time to generate an event is strongly related to the value of $P^{\max}$. A cut was introduced into the model, so that the probability is artificially forbidden from increasing past 18.25 GeV^2/c^4. This cut-off was chosen to minimize the impact on the q^2 distribution while still providing acceptable performance.

Fig. 5.4b shows a histogram of the number of CPU seconds required to generate each signal event from a sample of 8 million SM events. This sample was generated using 957 individual jobs, running at 42 different computing sites. This is a representative sample for the kind of MC production done in LHCb. The mean time to generate an event was 8.2 s. This should be compared with a mean of 1.9 s for the previous model, however it is still much less than the time required to run the full LHCb detector simulation.

5.3.2 Comparisons

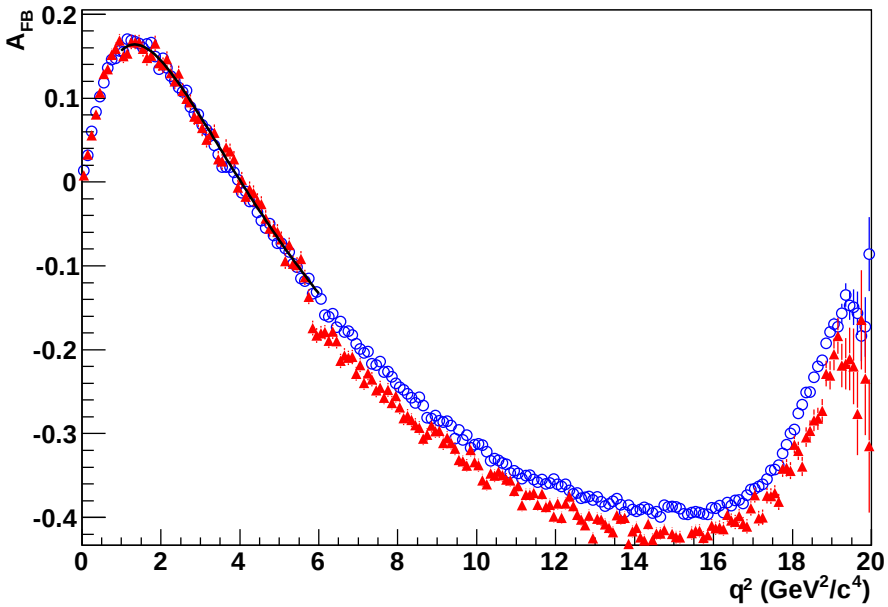

Figure 5.5: Comparison of $A_{\rm FB}$ distributions. The blue open points show the $A_{\rm FB}$ distribution produced by the `BTOKSTARLLDURHAM07` decay model. The black solid line shows the predicted distribution in the range $q^2 \in [1, 6]\,\mathrm{GeV}^2/c^4$ using the underlying K^{*0} spin amplitudes. The red triangles meanwhile show the $A_{\rm FB}$ distribution produced by the `BTOSLLBALL` model.

Fig. 5.5 shows the $A_{\rm FB}$ distributions produced by the `BTOKSTARLLDURHAM07` and `BTOSLLBALL` models. The agreement is excellent in the region $q^2 \in [0, 5.76]\,\mathrm{GeV}^2/c^4$. That the two models produce similar distributions is not surprising; both use similar form factor models [104, 120] and NNLL SM Wilson coefficients. However, there is a clear discontinuity at q^2 of $5.76\,\mathrm{GeV}^2/c^4$ arising from a change in the Wilson coefficient treatment as different renormalization scales become appropriate. The new model is able to avoid these unphysical effects as both low and high scale contributions are simultaneously present for all q^2 values. It should be noted however that the $A_{\rm FB}$ gradients produced by both models are similar at the zero-crossing point. This was, however, not true for the previous version of the `BTOSLLBALL` model considered in Ref. [112].

5.4 Summary

A new decay model for the simulation of $\overline{B}_d \to \overline{K}^{*0}\mu^+\mu^-$ has been developed which allows for a state-of-the-art SM simulation to be performed. The LO con-

tributions from NP may also be included using a selection of benchmark models, or via the direct specification of NP Wilson coefficient components. The basic theoretical framework used in the model has been described, and some comparisons have been made with the previous version. The model is fast enough to be used in signal MC production. It is hoped that it will be a useful tool for the study of $\overline{B}_d \to \overline{K}^{*0}\mu^+\mu^-$ as we enter the LHC era.

Chapter 6

Counting experiments for the first few years

6.1 Introduction

The four-body final state of $\overline{B}_d \to \overline{K}^{*0}(\to K\pi)\mu^+\mu^-$ allows for a wealth of observables beyond the branching fraction. The majority of signal events reconstructed at LHCb will be in the charged decay channel of the $\overline{K}^{*0}$. The presence of four charged tracks means that the angular resolution should be such that the three decay angles shown in Fig. 3.1 are available with high precision. The invariant mass of the muon pair will also be accurately determined. Thus it will be possible to make a detailed study of the angular distribution of the decay with LHCb. In the most commonly used basis, the angular distribution is made up of twelve basic components. The relative contribution of each is given by a coefficient $I_i^{(a)}$ (see Chap. 3) [56]:

$$\begin{aligned}\frac{d^4\Gamma}{dq^2 d\cos\theta_\ell d\cos\theta_{K^*} d\phi} \propto\ & I_1^s \sin^2\theta_{K^*} + I_1^c \cos^2\theta_{K^*} \\ & + \left(I_2^s \sin^2\theta_{K^*} + I_2^c \cos^2\theta_{K^*}\right)\cos 2\theta_\ell \\ & + I_3 \sin^2\theta_{K^*}\sin^2\theta_\ell \cos 2\phi \\ & + I_4 \sin 2\theta_{K^*}\sin 2\theta_\ell \cos\phi \\ & + I_5 \sin 2\theta_{K^*}\sin\theta_\ell \cos\phi \\ & + \left(I_6^s \sin^2\theta_{K^*} + I_6^c \cos^2\theta_{K^*}\right)\cos\theta_\ell \\ & + I_7 \sin 2\theta_{K^*}\sin\theta_\ell \sin\phi \\ & + I_8 \sin 2\theta_{K^*}\sin 2\theta_\ell \sin\phi \\ & + I_9 \sin^2\theta_{K^*}\sin^2\theta_\ell \sin 2\phi. \end{aligned} \tag{6.1}$$

These coefficients are functions of q^2 only. To avoid absolute measurements, these coefficients are normalized by the total rate at a given value of q^2 to give the relative decay rate received by each component of the angular distribution. The SM distribution for a fixed value of q^2 is shown in Fig. 6.1. Both the symmetries and the general features of the distribution can be seen. For more details see Sec. 3.2. NP can alter it by enhancing or suppressing one or more of the $I_i^{(a)}$ basis coefficients, in turn making particular features more or less pronounced. Disentangling the effect of each coefficient is the ultimate aim when planning a programme of measurements at LHCb.

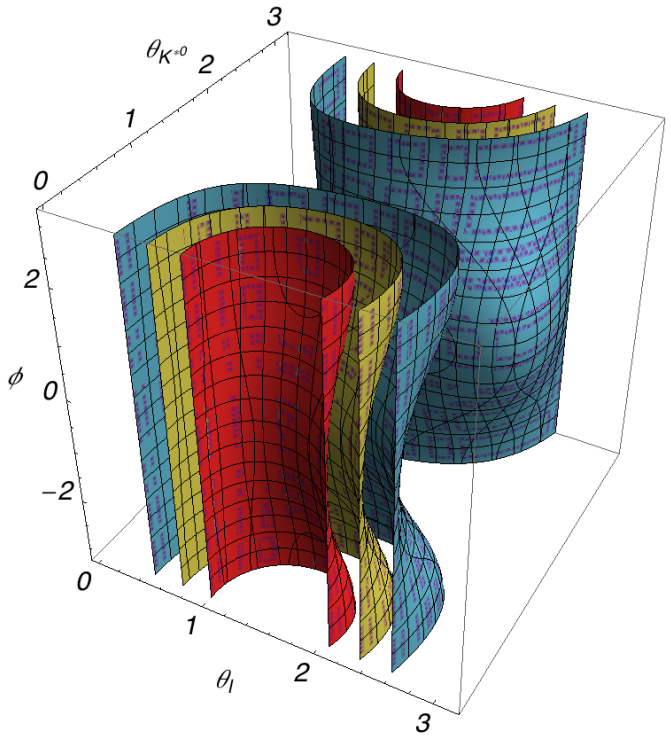

Figure 6.1: Contours of the differential decay rate for $\overline{B}_d \to \overline{K}^{*0}\mu^+\mu^-$. The surfaces show contours of equal differential decay rate, $d^4\Gamma/dq^2 d\theta_\ell d\theta_{K^*} d\phi$, for a fixed value of q^2 equal to $3.5\,\mathrm{GeV}^2/c^4$. The colour of a contour denotes the decay rate on that contour, following a rainbow ordering where red shows the largest decay rate. The distribution shown was generated from the decay model described in Chap. 5 using the SM calculation.

Considering both *CP*-averaged and *CP*-violating quantities we can define two sets of observables [56],

$$S_i^{(a)} = \left(I_i^{(a)} + \bar{I}_i^{(a)}\right) / \frac{d\left(\Gamma + \bar{\Gamma}\right)}{dq^2}, \qquad A_i^{(a)} = \left(I_i^{(a)} - \bar{I}_i^{(a)}\right) / \frac{d\left(\Gamma + \bar{\Gamma}\right)}{dq^2}, \tag{6.2}$$

that describe the properties of the angular distribution and can in turn be com-

pared to theoretical predictions. The total differential width is

$$\frac{d\Gamma}{dq^2} = \frac{3}{4}(2I_1^s + I_1^c) - \frac{1}{4}(2I_2^s + I_2^c), \tag{6.3}$$

implying the normalization condition

$$\frac{3}{4}(2S_1^s + S_1^c) - \frac{1}{4}(2S_2^s + S_2^c) = 1. \tag{6.4}$$

In the limit where the rest mass of the muons is small compared to their invariant mass, further simplifications to the angular distribution are possible. These are discussed further in Chap. 3. However these approximations will be avoided unless explicitly stated as they may introduce small experimental systematic effects.

The distributions of the *CP*-conserving and *CP*-violating observables are shown in Figs 6.2 and 6.3 for the theoretically clean region in q^2 from 1-6 GeV^2/c^4 both for the SM and for various NP models (see Chap. 5). While these figures do not necessarily indicate the full range of allowed values they do show the relative contributions to the angular distribution that might be expected. Several broad conclusions can be drawn by inspecting these figures. Firstly considering the *CP*-conserving observables shown in Fig. 6.2, the numerical sizes of S_3 and S_{7-9} are rather small when compared to typical experimental resolutions attainable for angular observables (e.g. Chap. 4). Noting that in the massless limit that $S_2^s = 1 - S_2^c$, there are four observables with predicted magnitudes of order 0.1 in the SM. These are S_2^c, S_4, S_5 and, S_6. Closer inspection of Eq. (6.1) shows that S_4 must be accessed via a full-angular fit due to the particular combination of trigonometric functions present; the term that it contributes to integrates out of the one- and two-dimensional distributions. The same is true for the term containing S_8. When a full-angular fit becomes possible (Sec. 4.1.3), other considerations are relevant when choosing which observables to measure in order to minimize the combined experimental and theoretical uncertainties (see Chap. 3). The other three observables however can be accessed by considering one or two decay angles only. This will allow for their extraction at an earlier stage than S_4. For this reason, they will be the major focus of this chapter.

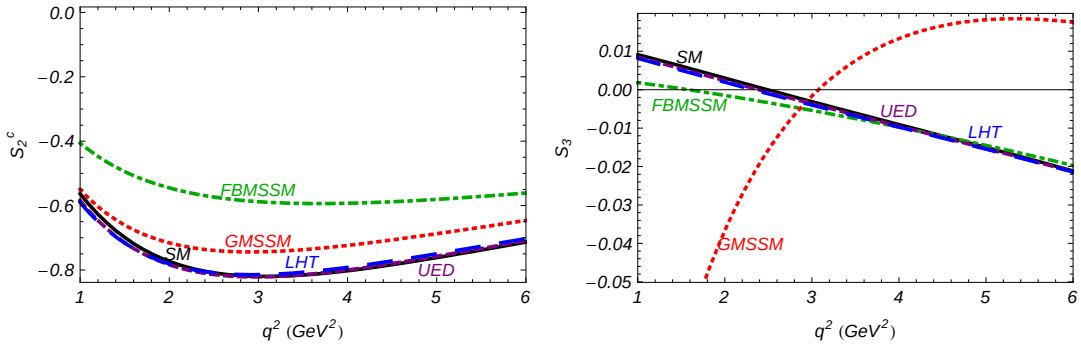

(a) S_2^c

(b) S_3

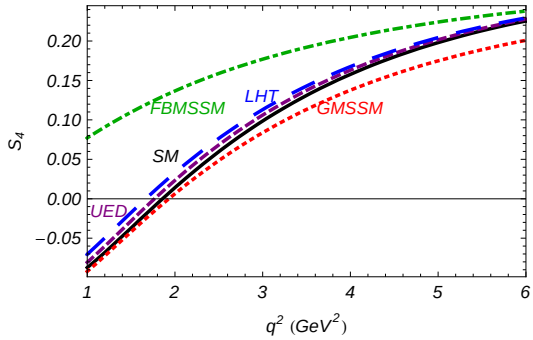

(c) S_4

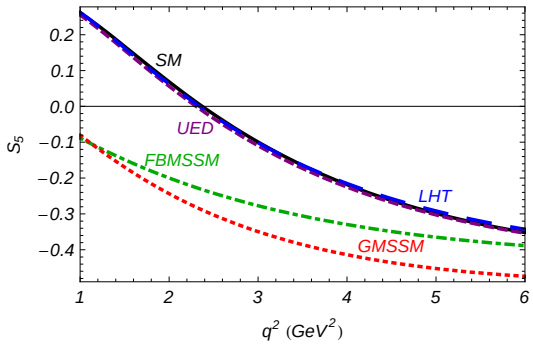

(d) S_5

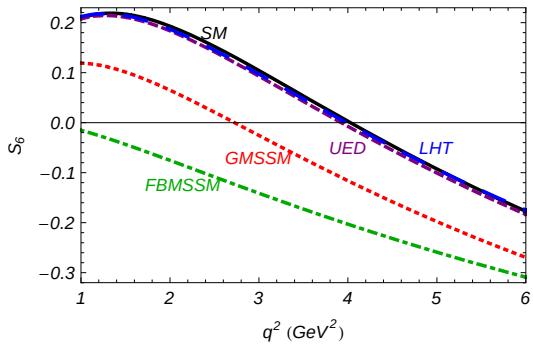

(e) S_6

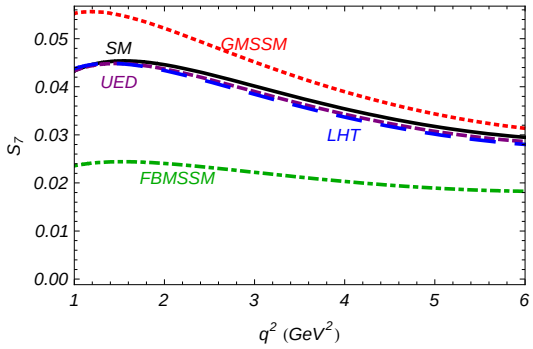

(f) S_7

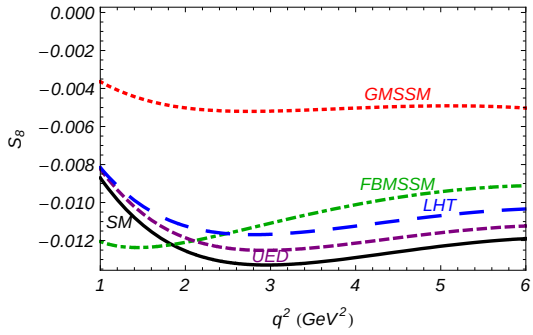

(g) S_8

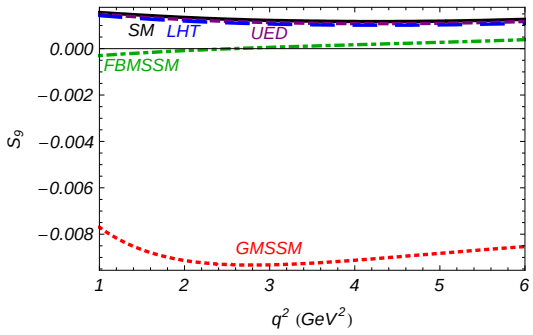

(h) S_9

Figure 6.2: *CP*-conserving angular observables with NP. These figures can be compared with Fig. 2 of Ref. [56]. The individual models shown are introduced in Sec. 5.2.5.

6.2 *CP*-conserving observables

As discussed in Ref. [56], S_2^c and S_6 are related to the commonly studied [75–78, 81] observables $A_{\rm FB}$ [127] and $F_{\rm L}$ [55]:

$$A_{\rm FB} = \frac{3}{8}\left(2S_6^s + S_6^c\right); \qquad F_{\rm L} = -S_2^c. \tag{6.5}$$

S_6^c vanishes in the SM and generically small in the presence of NP ([56] and the constraints shown in Sec. 6.6). S_5 is not linearly related to any other proposed observable, although it contributes to $A_T^{(4)}$ [1]. It provides complementary NP sensitivity to $A_{\rm FB}$ and $F_{\rm L}$; in addition to $C_7^{\rm eff}$ and $C_9^{\rm eff}$ it is sensitive to $C_7^{\prime\,\rm eff}$ and $C_{10}^{\prime\,\rm eff}$ [56]. These observables may be extracted using a fit to one or more decay angles (e.g. [107]) or by counting the number of events in specific angular bins. The latter approach has been extensively studied within LHC*b* as a method of extracting $A_{\rm FB}$ [112, 128]. In this case the number of signal events are split into two samples; one with $\cos\theta_\ell \in [-1, 0]$ and another with $\cos\theta_\ell \in [0, 1]$. $A_{\rm FB}$ can be found using Eq. (6.6) by estimating the number of signal events in each sample.

$$A_{\rm FB}(q^2) = \frac{\int_0^1 \frac{\partial^2\Gamma}{\partial q^2 \partial\cos\theta_\ell}\,{\rm d}\cos\theta_\ell - \int_{-1}^0 \frac{\partial^2\Gamma}{\partial q^2 \partial\cos\theta_\ell}\,{\rm d}\cos\theta_\ell}{\int_0^1 \frac{\partial^2\Gamma}{\partial q^2 \partial\cos\theta_\ell}\,{\rm d}\cos\theta_\ell + \int_{-1}^0 \frac{\partial^2\Gamma}{\partial q^2 \partial\cos\theta_\ell}\,{\rm d}\cos\theta_\ell}. \tag{6.6}$$

This is either done in bins of q^2 as in Ref. [112] or unbinned in q^2 as in Ref. [128]. These so called counting experiments are attractive as relatively early measurements at LHC*b* due to their conceptual simplicity. If we limit ourselves to those expressions which involve one or two decay angles then a variety of interesting observables become accessible, including those shown below, where $A_T^{(2)}$ is defined in Chap. 3. We have:

$$S_2^c = -\frac{1}{9}\left(11 - 16\left[\int_{-1/2}^{1/2} {\rm d}\cos\theta_{\rm K^*} {\rm d}\frac{{\rm d}^2(\Gamma+\bar\Gamma)}{{\rm dq}^2\,{\rm d}\theta_{\rm K^*}} \Big/ \frac{{\rm d}(\Gamma+\bar\Gamma)}{{\rm dq}^2}\right]\right) = -F_{\rm L}; \tag{6.7}$$

$$\begin{aligned} S_3 =& \frac{\pi}{2}\left[\int_0^{2\pi} - 4\int_{\frac{\pi}{4}}^{\frac{3\pi}{4}}\right] {\rm d}\phi \frac{{\rm d}^2(\Gamma+\bar\Gamma)}{{\rm dq}^2\,{\rm d}\phi} \Big/ \frac{{\rm d}(\Gamma+\bar\Gamma)}{{\rm dq}^2} \\ \approx& \frac{1}{2}(1-F_{\rm L})A_T^{(2)}, \text{ if the lepton masses can be neglected;} \end{aligned} \tag{6.8}$$

$$S_5 = \frac{4}{3}\left[\int_0^{\pi/2} + \int_{3\pi/2}^{2\pi} - \int_{\pi/2}^{3\pi/2}\right] {\rm d}\phi \left[\int_0^1 - \int_{-1}^0\right] {\rm d}\cos\theta_{\rm K^*} \frac{{\rm d}^3(\Gamma-\bar\Gamma)}{{\rm dq}^2\,{\rm d}\cos\theta_{\rm K^*}\,{\rm d}\phi} \Big/ \frac{{\rm d}(\Gamma+\bar\Gamma)}{{\rm dq}^2}; \tag{6.9}$$

$$\begin{aligned} S_6^s \approx& \frac{4}{3}\left[\int_0^1 - \int_{-1}^0\right] {\rm d}\theta_\ell \frac{{\rm d}^2(\Gamma+\bar\Gamma)}{{\rm dq}^2\,{\rm d}\theta_\ell} \Big/ \frac{{\rm d}(\Gamma+\bar\Gamma)}{{\rm dq}^2}, \text{ neglecting the contribution from } S_6^c, \\ \approx& \frac{4}{3}A_{\rm FB}. \end{aligned} \tag{6.10}$$

Of the numerically large observables, only S_2^c and S_6^s are accessible by considering a single decay angle. At the price of considering two decay angles, S_5 may also be extracted.

6.3 *CP*-violating observables

The SM expectations for the $A_i^{(a)}$ observables are very small and are neglected in Fig. 6.3. Allowing a weak phase to enter the NP Wilson coefficients can generate large *CP* asymmetries, for example in A_7 and A_9 which are both available without performing a full-angular analysis [106]. The SM contribution comes from a doubly Cabibbo suppressed term in the effective Hamiltonian (see Sec. 3.5.1). Any observation of non-zero asymmetries would be a clear sign of physics beyond the standard model. Both A_7 and A_9 may be extracted using angular counting as shown below.

$$A_7 = \frac{4}{3}\left[\int_0^{\pi} - \int_{\pi}^{2\pi}\right] \mathrm{d}\phi \left[\int_0^{1} - \int_{-1}^{0}\right] \mathrm{d}\cos\theta_{\mathrm{K}^*} \frac{\mathrm{d}^3(\Gamma - \bar{\Gamma})}{\mathrm{dq}^2\, \mathrm{d}\cos\theta_{\mathrm{K}^*}\mathrm{d}\phi} \Big/ \frac{\mathrm{d}(\Gamma + \bar{\Gamma})}{\mathrm{dq}^2} \tag{6.11}$$

$$A_9 = \frac{\pi}{2}\left[4\int_0^{\frac{\pi}{2}} - \int_0^{2\pi}\right] \mathrm{d}\phi \frac{\mathrm{d}^2(\Gamma - \bar{\Gamma})}{\mathrm{dq}^2\, \mathrm{d}\phi} \Big/ \frac{\mathrm{d}(\Gamma + \bar{\Gamma})}{\mathrm{dq}^2} \tag{6.12}$$

As discussed in Ref. [106], A_9 is particularly attractive experimentally. It is the *CP* asymmetry of the A_{Im} observable studied in Chap. 4. The angular coefficients $I_i^{(a)}$ transform under *CP* as

$$I^{(a)}_{1,2,3,4,7} \to I^{(a)}_{1,2,3,4,7}; \qquad I^{(a)}_{5,6,8,9} \to -I^{(a)}_{5,6,8,9}. \tag{6.13}$$

By performing the transformation $\phi \to -\phi$ on the signal B sample, A_9 may be extracted by considering only the ϕ angle and considering the B and $\overline{B}$ samples together.

6.4 Experimental analysis

In order to make a fair comparison between the statistical experimental sensitivities that might be expected for the different observables, a framework for making q^2 binned and unbinned counting analyses was constructed, following Refs [112, 128] where possible.

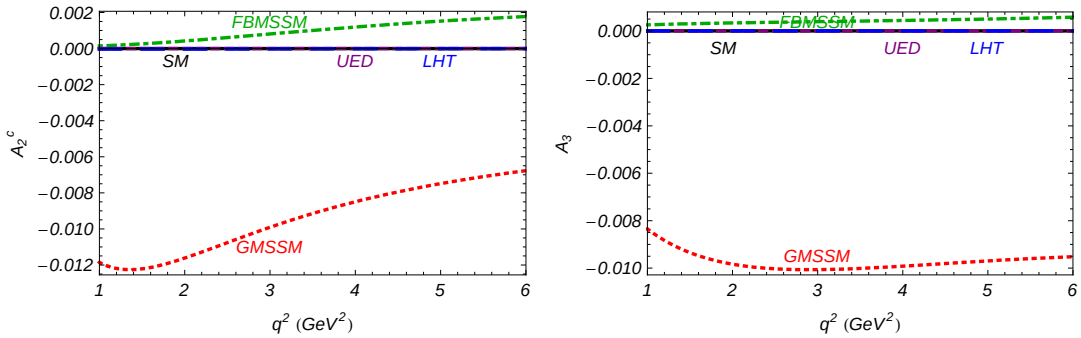

(a) A_2^c

(b) A_3

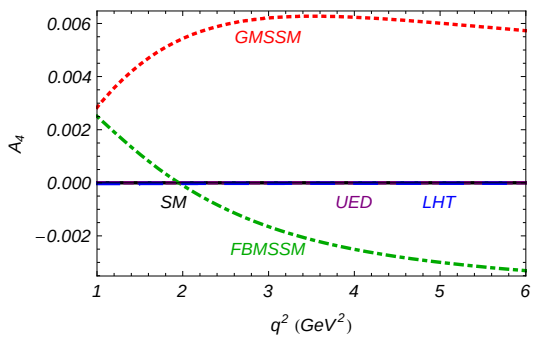

(c) A_4

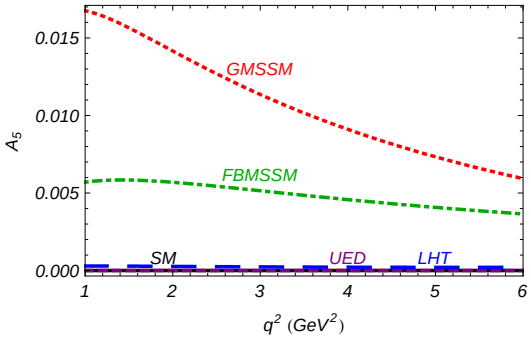

(d) A_5

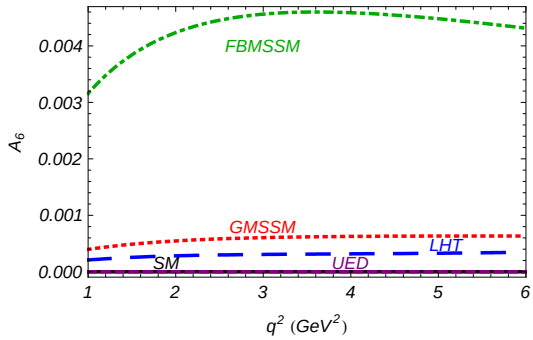

(e) A_6

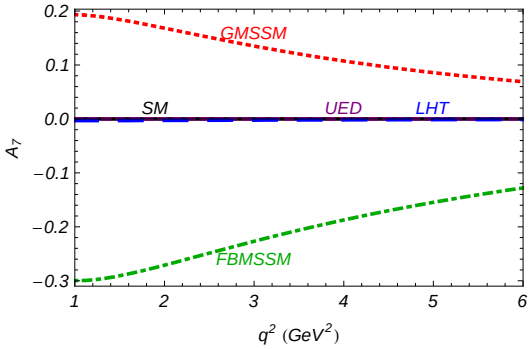

(f) A_7

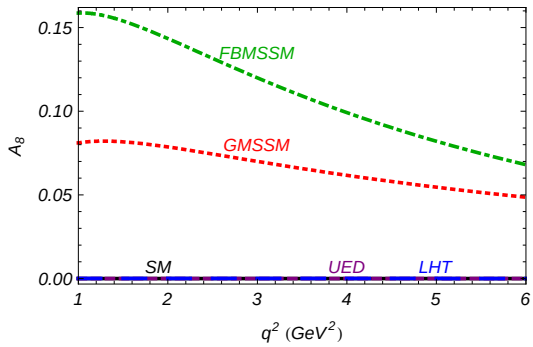

(g) A_8

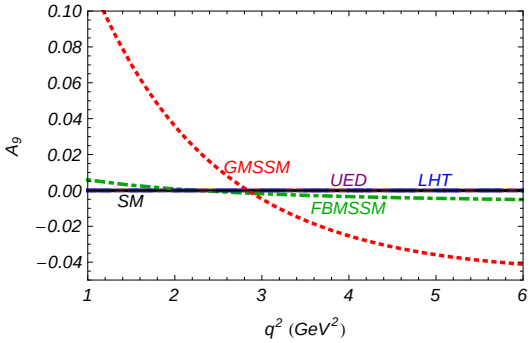

(h) A_9

Figure 6.3: *CP*-violating angular observables with NP. These figures can be compared with Fig. 3 of Ref. [56].

6.4.1 Generation

The decay model introduced in Chap. 5 was used to generate a sample of 8 million generator level SM signal events. These events were used as a source of signal events to produce an ensemble of toy experiments. A background sample was also included. As in Chap. 4, this background was generated as flat in the decay angles but follows the signal in q^2 and a gently falling exponential in m_B, the invariant mass of the B meson. The signal, background, and combined distributions are shown in Fig. 6.4. A particular event could be identified as being from the signal or background distributions, however this information was not used in the fits.

6.4.2 B mass fits

Fits to the B invariant mass distribution were used to determine the relative contribution of signal and background. The signal shape was parametrized as a Gaussian with an exponential tail, known as the Crystal Ball function (e.g. [129]). This includes the contribution from final state radiation. The background was modelled as an exponential with a single negative floating parameter. The shape parameters were determined in a fit to the entire data set and then fixed to determine the fraction of signal and background present in each angular bin. An example fit to $2\,\text{fb}^{-1}$ of simulated SM data can be seen in Fig. 6.4e.

6.4.3 Polynomial fits

A simultaneous fit in the signal region ($m_B^{\text{PDG}} \pm 50\,\text{MeV}$) and the region outside of this was performed to get the shape of each angular region as a function of q^2; m_B is the measured B meson mass, while m_B^{PDG} is its nominal value. A 10 MeV region either side of the signal box was excluded so that the signal contamination in the B mass side-band could be neglected. The background side-band region was taken to be $(m_B^{\text{PDG}} - 250\,\text{MeV}) \leq m_B \leq (m_B^{\text{PDG}} + 150\,\text{MeV})$, in line with LHC$b$ offline selections [72]. The signal fraction in the signal region was fixed using a fit to the B mass distribution and re-normalized numerically using the background shape function. It was assumed that all events in the mass side-band were background events although a one percent contamination was seen in the lower mass side band. The background distribution was modelled as a second order Chebyshev polynomial, while the signal distribution was taken to third order.

6.4.4 Analysis procedure: A_{FB}

Following Eq. (6.10), A_{FB} can be extracted by performing separate fits in two bins of the decay angle θ_ℓ. This was done for events with $q^2 \in [0.5, 8.5]\,\text{GeV}^2/c^4$

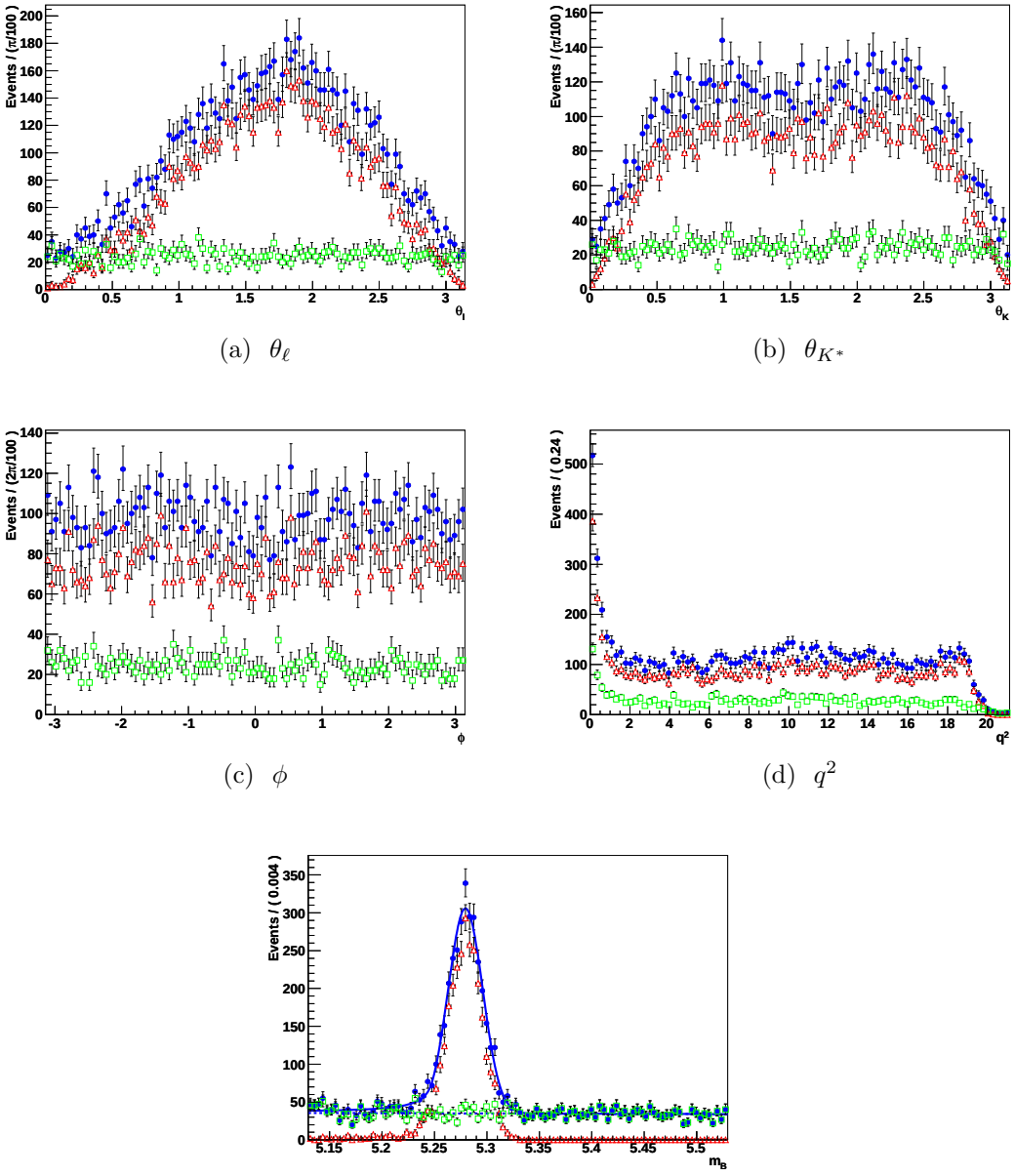

(a) θ_ℓ (b) θ_{K^*}

(c) ϕ (d) q^2

(e) m_B

Figure 6.4: A sample $2\,\mathrm{fb}^{-1}$ SM toy data set showing the decay angles (Figs (a)-(c)), and the invariant masses of the di-muon (squared; Fig. (d)) and total decay (Fig. (e)). The blue closed circles, red open triangles and green open squares show respectively the combined, generated signal, and background distribution. In addition Fig. (e) shows an example mass fit to the entire toy data set.

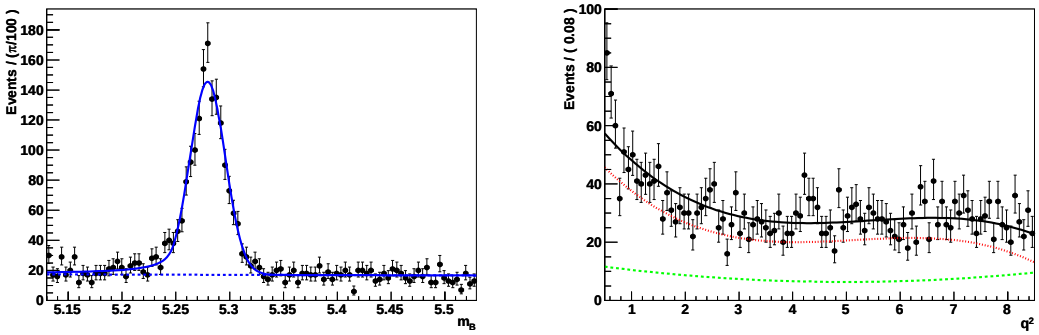

(a) m_B^F (b) q_F^2

(c) m_B^B (d) q_B^2

Figure 6.5: B mass and θ_ℓ polynomial fits for $A_{\rm FB}$. The F and B labels indicate the forward and backward angular bins.

to maximize the sensitivity to the zero-crossing [128]. The analysis framework described above was applied as follows:

- Perform a fit to the B mass distribution for all events with $q^2 \in [q^2_{\rm min}, q^2_{\rm max}]$ to determine the m_B signal and background shape parameters. An example $2\,{\rm fb}^{-1}$ fit can be seen in Fig. 6.4e.

- Divide the data set into two; one with $\cos\theta_\ell \in [-1, 0]$ and another with $\cos\theta_\ell \in [0, 1]$, following Eq. (6.10).

- Perform individual fits to the B mass distribution with the shape parameters fixed. Determine the signal fraction in each of the angular bins and estimate its value in the signal region. The number of signal events in each bin, n_F and n_B can be found. Example fits are shown in Figs 6.5a and 6.5c.

- Fit the q^2 distribution simultaneously in the signal and B mass side-band regions using Chebyshev polynomials. The signal fraction in the signal region is now fixed to the value found in the previous step. This allows for the background subtracted signal distributions $f(q^2)$ and $b(q^2)$ to be found. Example fits are shown in Figs 6.5b and 6.5d.

- Use the number of signal events found with the mass fits, and the shape information from the polynomial fits to determine

$$A_{\rm FB}(q^2) = \frac{n_F f(q^2) - n_B b(q^2)}{n_F b(q^2) + n_B b(q^2)}. \tag{6.14}$$

- Determine the point in q^2 were $A_{\rm FB}$ is zero using a iterative numerical algorithm applied to Eq. (6.14).

Any observable which can be extracted via a counting experiment of this sort can in principle have its q^2 dependent distribution determined if there are enough events in each angular bin to perform a mass fit. For smaller data sets, considering q^2 integrated quantities will produce more robust results.

6.4.5 Integrated quantities

Theoretical uncertainties are under control in the *theoretically clean* window, $q^2 \in [1, 6]\,{\rm GeV}^2/c^4$, as discussed in Chap. 3. To minimize the combined experimental and theoretical uncertainties, a single measurement can be made of the rate average of an observable within this window, defined for a variable $V(q^2)$ as

$$\langle V \rangle_{1-6\,{\rm GeV}^2} = \int_{1\,{\rm GeV}^2}^{6\,{\rm GeV}^2} {\rm d}q^2 V(q^2) \Bigg/ \int_{1\,{\rm GeV}^2}^{6\,{\rm GeV}^2} {\rm d}q^2 \frac{{\rm d}(\Gamma + \bar{\Gamma})}{{\rm dq}^2}. \tag{6.15}$$

While the q^2 dependence of the angular observables will be important to separate different classes of NP if discovered, comparing SM predictions and the rate averaged quantities offer a chance for discovery with lower integrated luminosities and allows for precision measurements.

The same tools are used to perform the fits as in the previous section. A B mass fit of the entire data set is performed to extract the signal and background shape parameters, as described in Sec. 6.4.2. The data is then split up into the appropriate angular bins and a second B mass fit is performed in each bin. These are used to extract the fraction of signal and background per angular bin, from which an estimate of the actual number of signal events present can be made. These numbers may then be used to find the integrated value of each observable directly using the appropriate expression.

6.5 Results

The methods described in Sec. 6.4 can be applied to a number of observables using Eqs 6.7-6.12. This was done for toy LHCb data sets corresponding to $0.5\,\text{fb}^{-1}$, $1\,\text{fb}^{-1}$ and $2\,\text{fb}^{-1}$, assuming the SM. It is expected that LHCb will accumulate the largest of these data set sizes in the first three years of running, so these samples illustrate what may be possible in this time. Following the methods of Chap. 4, an ensemble of 1200 toy LHCb experimental data sets was generated for each of the three integrated luminosities considered. Each data set was produced as described in Sec. 6.4.1. For each data set, q^2 dependent analyses were performed to extract A_{FB}, S_3, S_5, A_7, and A_9 as well as the zero-crossing points of A_{FB} and S_5. In addition q^2 integrated analyses were run to extract $\langle A_{\text{FB}}\rangle_{1-6\,\text{GeV}^2}$, $\langle F_{\text{L}}\rangle_{1-6\,\text{GeV}^2}$, $\langle S_5\rangle_{1-6\,\text{GeV}^2}$, and $\langle A_9\rangle_{1-6\,\text{GeV}^2}$. Each data set was independent, however the individual analyses were run sequentially on the same data, so that any correlations could be seen. This produced a further ensemble, for example, $\{\langle A_{\text{FB}}\rangle_{1-6\,\text{GeV}^2}\}^{1200}$ enabling an estimate of the 1σ statistical uncertainty expected for a data set of that size to be found. As in chapters 3 and 4, this was done by ordering the ensemble and then selecting the results closest to the appropriate contour.

Fig. 6.6 shows the results of this process for the integrated quantities and zero-crossings using $2\,\text{fb}^{-1}$ SM data sets. The one and two σ contours are shown, as are the median and input values. It can be seen that for all but $\langle F_{\text{L}}\rangle_{1-6\,\text{GeV}^2}$, shown in Fig. 6.6d, any biases seen are small compared to the estimated sensitivities. This bias appears relative to the value of $\langle F_{\text{L}}\rangle_{1-6\,\text{GeV}^2}$ calculated using the underlying amplitudes of the decay model and is thought to be an artefact of the method used to generate the input data sets. A summary of the estimated sensitivities can be found in Tab. 6.1. Where possible the smallest available official LHCb

Observable	$2\,\text{fb}^{-1}$	$1\,\text{fb}^{-1}$	$0.5\,\text{fb}^{-1}$	LHCb $2\,\text{fb}^{-1}$	Ref.
$q_0^2(A_{\text{FB}})$	$^{+0.56}_{-0.94}$	$^{+1.27}_{-0.97}$	–	0.42	[128]
$q_0^2(S_5)$	$^{+0.27}_{-0.25}$	$^{+0.53}_{-0.40}$	–	–	
$\langle A_{\text{FB}}\rangle_{1-6\,\text{GeV}^2}$	$^{+0.03}_{-0.04}$	$^{+0.05}_{-0.03}$	$^{+0.08}_{-0.06}$	0.020	[107]
$\langle F_{\text{L}}\rangle_{1-6\,\text{GeV}^2}$	$^{+0.02}_{-0.02}$	$^{+0.04}_{-0.03}$	$^{+0.04}_{-0.06}$	0.016	[107]
$\langle S_5\rangle_{1-6\,\text{GeV}^2}$	$^{+0.07}_{-0.08}$	$^{+0.09}_{-0.11}$	$^{+0.16}_{-0.15}$	–	
$\langle A_9\rangle_{1-6\,\text{GeV}^2}$	$^{+0.08}_{-0.07}$	$^{+0.11}_{-0.11}$	$^{+0.22}_{-0.14}$	0.015	[2][a]

Table 6.1: Estimated 1σ LHCb sensitivities for $2\,\text{fb}^{-1}$, $1\,\text{fb}^{-1}$ and $0.5\,\text{fb}^{-1}$ of integrated luminosity, assuming the SM. Where available, the smallest official LHCb $2\,\text{fb}^{-1}$ sensitivity estimate is also shown. Only Ref. [128] is directly comparable with this work, although LHCb signal yield estimates have been revised downwards since its release [8, 72].

[a]Based on the sensitivity to A_{Im}, which is the *CP* average of the I_9 angular term while A_9 is the *CP* asymmetry. See also Sec. 4.3.

$2\,\text{fb}^{-1}$ estimate is also shown for comparison. The same ordering procedure can be used to estimate the contours for the q^2 dependent quantities. In this case the contours are found as with the integrated quantities, but with a fixed value of q^2. Doing this at many values of q^2 results in the bands shown in Fig. 6.7.

6.5.1 Analysis

The sensitivities shown in Tab. 6.1 follow a pattern hinted at in Sec. 6.1. The observable with the largest absolute size, as shown in Fig. 6.2, is F_{L}. This can be extracted using only the θ_{K^*} decay angle with Eq. (6.7). This is borne out by recent Belle experimental results [75]. The ratio of uncertainties for $\langle A_{\text{FB}}\rangle_{1-6\,\text{GeV}^2}$ and $\langle F_{\text{L}}\rangle_{1-6\,\text{GeV}^2}$ is similar to that found by Belle. The estimated sensitivity on $\langle S_5\rangle_{1-6\,\text{GeV}^2}$ is poorer still. $\langle F_{\text{L}}\rangle_{1-6\,\text{GeV}^2}$ may be extracted by performing fits in two bins, as can $\langle A_{\text{FB}}\rangle_{1-6\,\text{GeV}^2}$. To extract $\langle S_5\rangle_{1-6\,\text{GeV}^2}$ requires six angular bins; experimental systematic effects are also likely to be a concern due to a more challenging angular acceptance.

We also study the sensitivity to S_3, which is related to the well known observable $A_T^{(2)}$ [55]. Its smallness in the SM means that, as found in Ref. [107], the experimental resolutions obtained are poor, as seen in Fig. 6.7c. In the presence of significant NP in $C_7'^{\text{eff}}$, this term can be considerably enhanced [57], however it will be challenging to find an unambiguous NP signal in the first few years with this observable alone. Fig. 6.2b shows the S_3 distribution in various NP scenarios, including the GMSSM which has $C_7'^{\text{eff NP}} = 0.174 + 0.174i$. While the

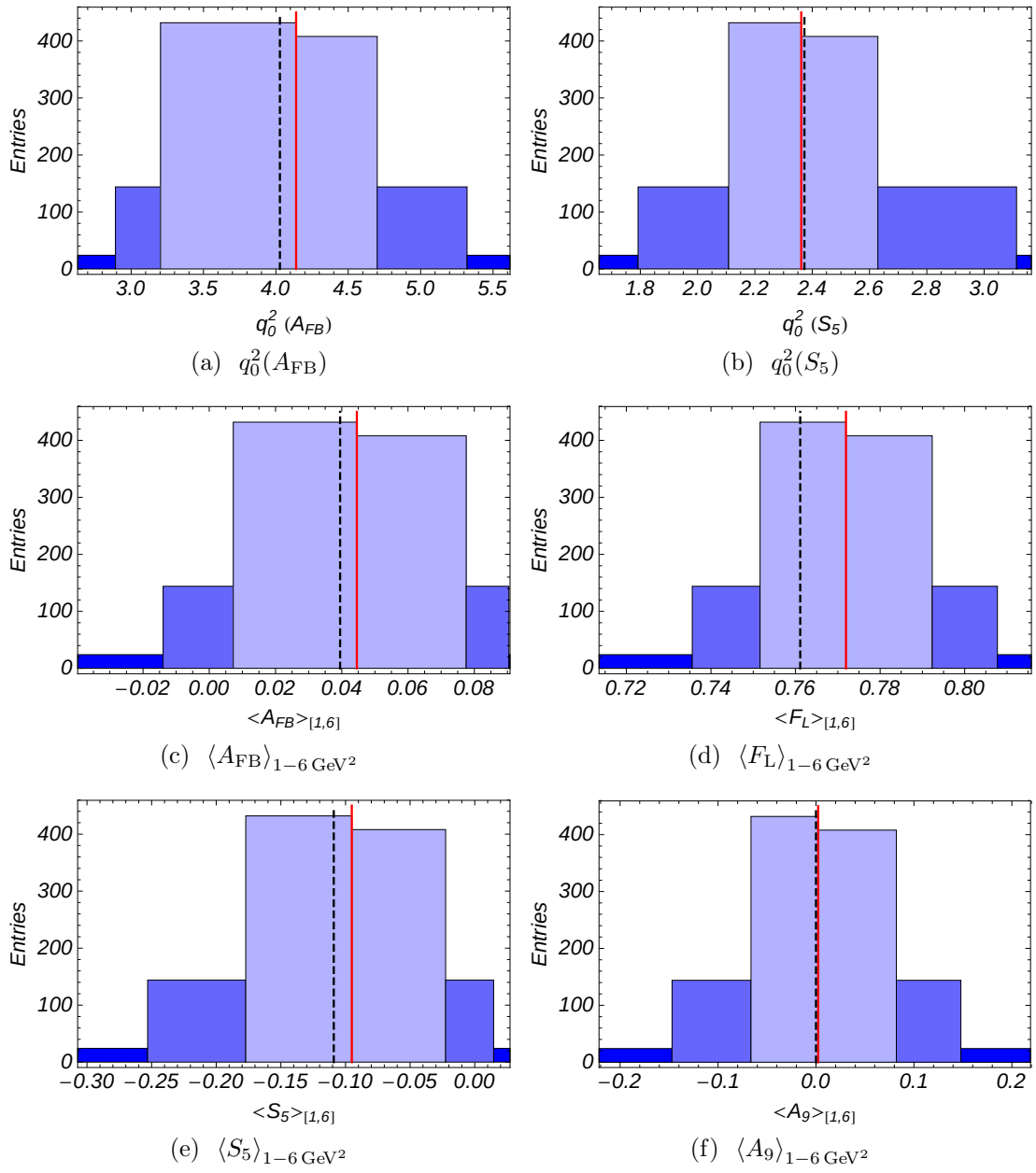

(a) $q_0^2(A_{\rm FB})$ (b) $q_0^2(S_5)$

(c) $\langle A_{\rm FB}\rangle_{1-6\,{\rm GeV}^2}$ (d) $\langle F_{\rm L}\rangle_{1-6\,{\rm GeV}^2}$

(e) $\langle S_5\rangle_{1-6\,{\rm GeV}^2}$ (f) $\langle A_9\rangle_{1-6\,{\rm GeV}^2}$

Figure 6.6: Figs (a) and (b) show histograms of the q^2 values at which the $A_{\rm FB}$ and S_5 distributions shown in Figs 6.7a and 6.7b respectively are equal to zero. Figs (c)-(f) show the ensemble of q^2 integrated observables for $2\,{\rm fb}^{-1}$ of simulated SM data. In each figure the input distribution is shown as a dashed black line. The median value of the ensemble as a function of q^2 is shown as a solid red line. The light and dark bands show estimates of the one and two sigma confidence levels that would be found if these fits were performed on $2\,{\rm fb}^{-1}$ of SM like data. In addition the very dark blue bands indicate those events in the ensemble which fall outside of the two sigma contour.

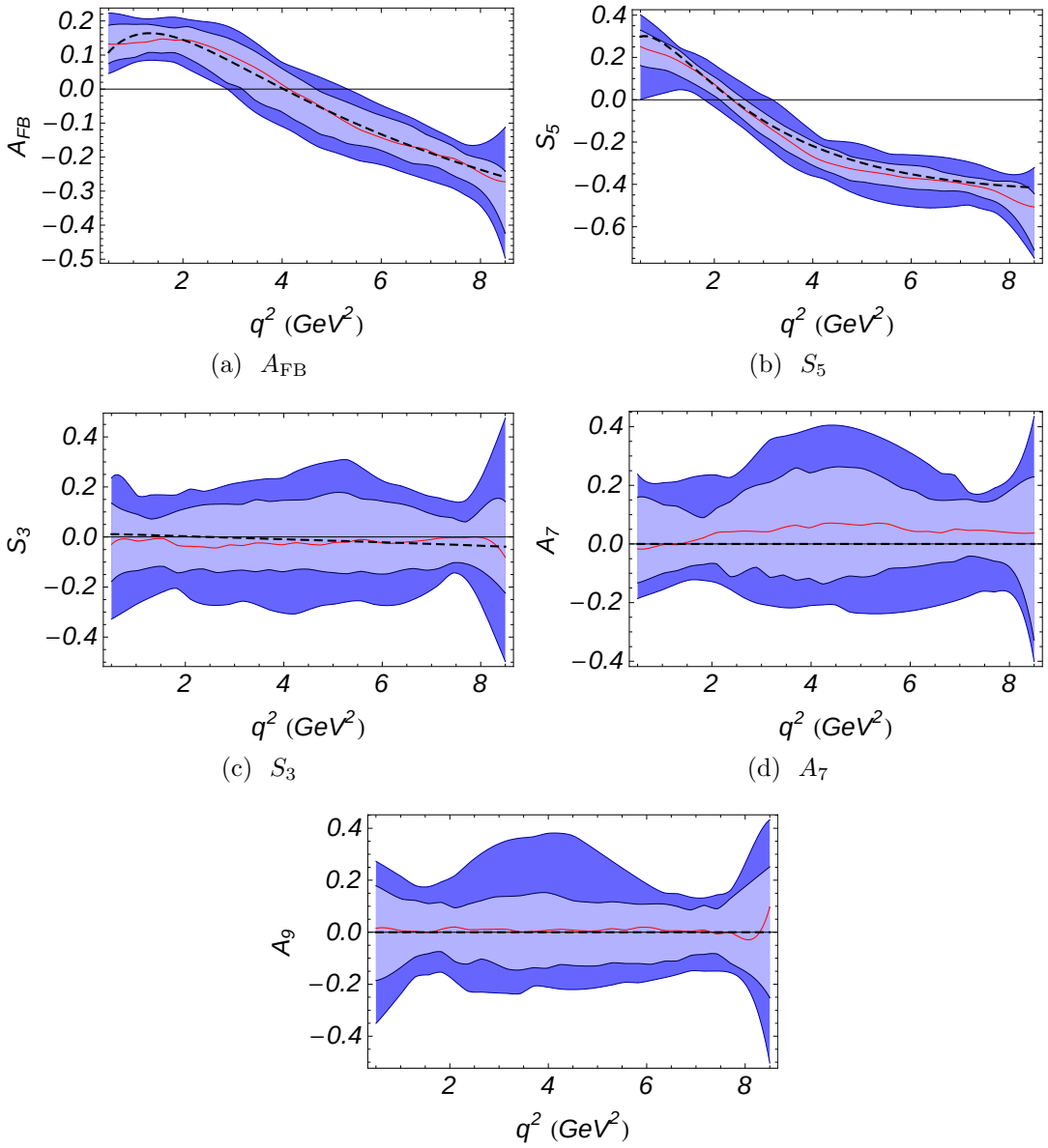

(a) A_{FB} (b) S_5

(c) S_3 (d) A_7

(e) A_9

Figure 6.7: Results of unbinned polynomial fits for $2\,\mathrm{fb}^{-1}$ in the range $q^2 \in [0.5, 8.5]\,\mathrm{GeV}^2/c^4$. The colour scheme is the same as in Fig. 6.6, but regions outside the 2σ contour are no longer shown.

enhancement seen is significant, the overall magnitude is still rather small. In this chapter, those observables which are numerically large are favoured for pragmatic reasons and so S_3 will be left for other works less bound by these considerations, notably Ref. [1].

Both $A_{\rm FB}$ and S_5 have zero-crossings in the SM. These are of interest as they provide additional opportunities for comparison with theoretical predictions and have reduced hadronic theoretical uncertainties [7]. As discussed in Sec. 4.3.2, the experimental uncertainty on a zero-crossing point is approximately linearly related to the gradient of the distribution as it goes through the zero. We define these gradients for $A_{\rm FB}$ and S_5 as

$$G_0(A_{\rm FB}) = \frac{{\rm d}A_{\rm FB}}{{\rm d}q^2}\Big|_{q_0^2(A_{\rm FB})} \qquad \text{and} \qquad G_0(S_5) = \frac{{\rm d}S_5}{{\rm d}q^2}\Big|_{q_0^2(S_5)} . \tag{6.16}$$

In the SM treatment used in this chapter, these have the ratio

$$\frac{G_0(S_5)}{G_0(A_{\rm FB})} \approx 1.75. \tag{6.17}$$

The ratio of the estimated $q_0^2(A_{\rm FB})$ and $q_0^2(S_5)$ uncertainties shown in Tab. 6.1 is actually greater than this due to the long negative tail in the $q_0^2(A_{\rm FB})$ ensemble, see Fig. 6.6a; the RMSs of the two distributions are closer to the expected value of two. This is significant, as it offers the chance to access $q_0^2(S_5)$ with better statistical precision than for $q_0^2(A_{\rm FB})$ for the same integrated luminosity.

Finally the *CP* asymmetries A_7 and A_9 are considered. As can be seen in Fig. 6.3, these asymmetries vanish in the SM, but may be significantly enhanced in some NP models. The experimental sensitivity, as seen from Tab. 6.1 and Fig. 6.7 is quite limited. As explained in Ref. [106], $\langle A_9 \rangle_{1-6\,{\rm GeV}^2}$ has some promise as it may be extracted using just two angular bins in the ϕ decay angle. Current limits on *CP* violation are rather poor, and any constraint would be worthwhile. The sensitivities for a $10\,{\rm fb}^{-1}$ full-angular analysis are shown in Fig. 4.8. The improvement is significantly better than would be expected from naive scaling of the uncertainties. It may require an analysis of this sort before these measurements reach the precision required to exclude more realistic NP models.

Consideration of Tab. 6.1 shows that the counting analyses presented, while generic, are not optimal. The LHC*b* $B_d \to K^{*0}\mu^+\mu^-$ signal yield estimates have recently been revised downwards [8]. This is reflected in this work, but not in those referenced in Tab. 6.1. The sensitivities presented in this chapter are expected to be relatively conservative and may be improved once dedicated methods have been developed and LHC*b* data taking has further progressed.

6.6 Model-independent constraints on NP

Experimental results can be used to constrain NP contributions, $C_i^{\rm NP}$, of the Wilson coefficients, C_i, where $C_i = C_i^{\rm SM} + C_i^{\rm NP}$. We can then determine possible model-independent effects of NP on $\overline{B}_d \to \overline{K}^{*0}\mu^+\mu^-$. The most important constraints on the Wilson coefficients are the following:

$\mathcal{B}(B_s \to \mu^+\mu^-)$: This is used to constrain the possible NP contribution to the scalar and pseudoscalar operators. To calculate the branching ratio the standard result from Ref. [56] is used. In agreement with existing results, we find the SM prediction $\mathrm{BR}(B_s \to \mu^+\mu^-) = (3.70 \pm 0.31) \cdot 10^{-9}$ to be well below the current experimental upper bound $3.6 \cdot 10^{-8}$ [122].

$\mathcal{B}(B \to X_s l^+ l^-)$: We compare NP predictions for $\mathcal{B}(B \to X_s l^+ l^-)_{1-6\,\mathrm{GeV}^2}$ to the mean experimental value $(1.60 \pm 0.51) \cdot 10^{-6}$, as adopted in Ref. [106] combining the results of *BABAR*, $(1.8 \pm 0.7 \pm 0.5) \cdot 10^{-6}$ [130], and Belle, $(1.49^{+0.41}_{-0.32} \pm 0.50) \cdot 10^{-6}$ [131]. This helps to constrain the NP contribution to $C_{7,8,9}^{(\prime)\,\mathrm{eff}}$ as well as $\mathcal{C}_{S,P}^{(\prime)}$. Being an inclusive mode, the calculation for the region $q^2 \in [1,6]\,\mathrm{GeV}^2/c^4$ of the branching ratio is theoretically clean. We use the expression for the differential decay distribution in Ref. [132], but also include the NLO corrections computed in Ref. [133], and the contribution of the primed operators as in Ref. [134]. Using our parameters we predict $\mathcal{B}(B \to X_s l^+ l^-) = (1.97 \pm 0.11) \cdot 10^{-6}$ for the SM.

$\mathcal{B}(B \to X_s\gamma)$: The recent theoretical result of Ref. [49], $(3.28 \pm 0.25) \cdot 10^{-4}$, is used and NP effects are included as in Ref. [57]. This can be compared to the current experimental average for $\mathrm{E}_\gamma > 1.6\,\mathrm{GeV}$, $\mathcal{B}(B \to X_s\gamma) = (3.52 \pm 0.23 \pm 0.09) \cdot 10^{-9}$ found by the Heavy Flavour Averaging Group (HFAG) [20].

$\mathcal{S}(B \to K^*\gamma)$: The time-dependent *CP* asymmetry of $B \to K^{*0}\gamma$ is sensitive to the photon polarization, and hence to $C_7^{\prime\,\mathrm{eff}}$. Our result of $\mathcal{S}(B \to K^*\gamma) = (-0.26 \pm 0.05) \cdot 10^{-1}$ agrees with that of Ref. [106] within uncertainties. This should be compared to $\mathcal{S}(B \to K^*\gamma) = (-1.6 \pm 2.2) \cdot 10^{-1}$ from experiment [20].

$\langle A_{\rm FB}\rangle_{1-6\,\mathrm{GeV}^2}$ for $\overline{B}_d \to \overline{K}^{*0}\mu^+\mu^-$: Belle has a recent measurement of $\langle A_{\rm FB}\rangle_{1-6\,\mathrm{GeV}^2}$ equal to -0.26 ± 0.29 [75]. This is to be compared to the SM prediction of 0.04 ± 0.03, made using the underlying amplitudes of the decay model presented in Chap. 5 and compatible with the value found in Ref. [111] once the sign convention change has been taken into account. While *BABAR* has a comparable measurement [77], it is made in a larger q^2 window which is

Observable	Experiment	SM Theory
$\mathcal{B}(B_s \to \mu^+\mu^-)$	$3.6 \cdot 10^{-8}$ [122]	$(3.70 \pm 0.31) \cdot 10^{-9}$
$\mathcal{B}(B \to X_s l^+ l^-)_{1-6\,\mathrm{GeV}^2}$	$(1.60 \pm 0.51) \cdot 10^{-6}$ [106]	$(1.97 \pm 0.11) \cdot 10^{-6}$
$\mathcal{B}(B \to X_s \gamma)$	$(3.52 \pm 0.23 \pm 0.09) \cdot 10^{-4}$ [20]	$(3.28 \pm 0.25) \cdot 10^{-4}$
$\mathcal{S}(B \to K^* \gamma)$	$(-1.6 \pm 2.2) \cdot 10^{-1}$ [20]	$(-0.26 \pm 0.05) \cdot 10^{-1}$
$\langle A_{\mathrm{FB}} \rangle_{1-6\,\mathrm{GeV}^2}$	-0.26 ± 0.29 [75]	0.04 ± 0.03
$\langle F_L \rangle_{1-6\,\mathrm{GeV}^2}$	0.67 ± 0.24 [75]	0.76 ± 0.08

Table 6.2: Experimental measurements used as constraints, along with theoretical predictions in the SM.

problematic to handle theoretically. An analysis which includes the *BABAR* data can be found in Ref. [135].

$\langle F_{\mathrm{L}} \rangle_{1-6\,\mathrm{GeV}^2}$ for $\overline{B}_d \to \overline{K}^{*0} \mu^+ \mu^-$: Belle has also recently measured $\langle F_{\mathrm{L}} \rangle_{1-6\,\mathrm{GeV}^2}$ to be 0.67 ± 0.24 [75]. This should be compared to the SM prediction 0.76 ± 0.08, again made using the underlying decay model amplitudes. This is very compatible with the values found in Refs [106, 111] but less so with Ref. [1].

These expressions were implemented using the framework introduced in Chap. 5. This allowed for their value with arbitrary values of $C_i^{(\prime)\mathrm{NP}}$ to be calculated, for $i \in \{7\text{-}10, S, P\}$. No observable considered here has sensitivity to $\mathcal{C}_{S,P}$ and $\mathcal{C}'_{S,P}$ individually. These are combined as ($\mathcal{C}_S$-$\mathcal{C}'_S$) and ($\mathcal{C}_P$-$\mathcal{C}'_P$) for clarity. A semi-random walk through parameter space was performed in order to assess the impact of these constraints on the underlying Wilson coefficients in as general a way as possible. We allow the NP components of all Wilson coefficients to vary simultaneously, both in magnitude and phase. A simple optimization algorithm, shown in Alg. 1 and based on the ideas of Markov Chain Monte Carlo (MCMC), was used to sample the allowed regions of parameter space without prejudice. It traces a path through parameter space where each point has a χ^2, calculated using the six experimental constraints above, smaller than the last point in the chain, until a region is found that is in better agreement with data than two σ.

A probability metric was used which treats experimental uncertainties as being normally distributed, but theoretical uncertainties as having uniform probability within a specified range,

$$\begin{aligned}\Pr(C_i, P_i, \sigma_{C_i}, \sigma_{P_i}) =& \int_{(P_i - \sigma_{P_i})}^{(P_i + \sigma_{P_i})} \mathrm{Gaus}[C_i, \sigma_{C_i}](x)\,\mathrm{d}x \\ =& \frac{1}{2\sqrt{2}\sigma_{C_i}} \left[\mathrm{Erf}\left(C_i - x \right) \right]_{(P_i + \sigma_{P_i})}^{(P_i - \sigma_{P_i})}. \end{aligned} \tag{6.18}$$

This probability was then mapped on to the one dimensional χ^2 distribution.

Algorithm 1 The MCMC algorithm for a semi-random walk through Wilson coefficients parameter space.

repeat
  {Pick starting values}
  for $j \in [7, 8, 9, 10, S, P]$ **do**
    $\mathcal{C}_j \leftarrow \text{Gaus}(0,1)\exp(i\,\text{uniform}(0, 2\pi))$
    $\mathcal{C}'_j \leftarrow \text{Gaus}(0,1)\exp(i\,\text{uniform}(0, 2\pi))$
  end for
until $\chi^2 < 5\sigma$
repeat
  $total \leftarrow \chi^2$; $prob \leftarrow \Pr(total)$
  repeat
    for $j \in [7, 8, 9, 10, S, P]$ **do**
      {Perturb both modulus and phases of all coefficients}
      $\mathcal{C}_j \leftarrow \mathcal{C}_j \times \text{Gaus}(0, 1 - prob)$; $\mathcal{C}'_j \leftarrow \mathcal{C}'_j \times \text{Gaus}(0, 1 - prob)$
    end for
    if $(\chi^2 > total)$ **then**
      if $(\text{uniform}(0, 1000) < 997)$ **then**
        Reset to previous values of $\mathcal{C}_j^{(\prime)}$
      end if
    end if
  until $\chi^2 < total$
until $total < 2\sigma$

Using this approach, greater consistency was provided with the treatment of theoretical uncertainties in Sec. 3.5. However the difference between this and a traditional χ^2 metric was minimal.

In order to treat the $\mathcal{B}(B_s \to \mu^+\mu^-)$ measurement consistently with other constraints, it was assumed that the reported exclusion contours were normally distributed. This allowed for the ninety and ninety-five percent exclusion limits to be converted to a central value and uncertainty. This is illustrated in Fig. 6.8. The central value found was $(1.13 \pm 1.93) \times 10^{-8}$. The fact that positive values are favoured suggests that signal events were seen, but with low significance.

As shown in Alg. 1, the random walk is guided by the value of the χ^2 so that regions with higher compatibility may be identified. The additive nature of the χ^2 distribution was particularly important as some constraints were much less computationally intensive to calculate than others. The fastest constraints to calculate were applied first with looser bounds, so that computationally complex quantities such as $\langle A_{\text{FB}} \rangle_{1-6\,\text{GeV}^2}$ were only calculated if the agreement with other observables was already close to the level required. Using this method, a sample of $2.5 \cdot 10^5$ independent sets of Wilson coefficients were produced. Each set results in predictions for the observables listed above with better than two σ agreement with current measurements. It was found that the agreement with the

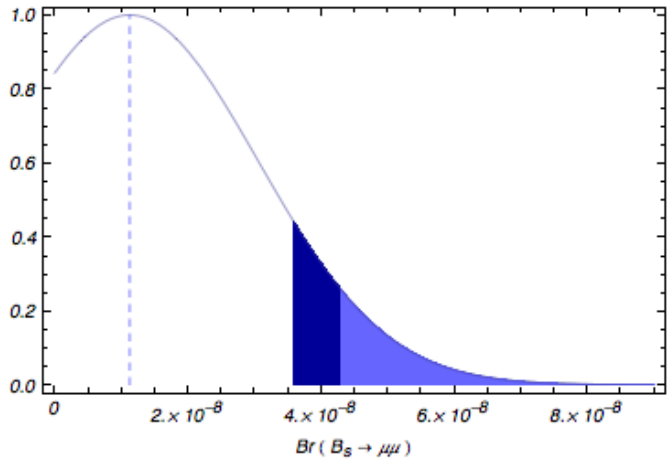

Figure 6.8: The contours of $\mathcal{B}(B_s \to \mu^+\mu^-)$ from Ref. [122] assuming normal distribution.

SM is currently excellent, with a χ^2 per degree of freedom of 0.35 (91%). This agreement is better than would normally be expected for six semi-independent measurements. The current treatment neglects correlations between theoretical uncertainties; the low χ^2 found may suggest that a more detailed study of the theoretical uncertainties will be required once higher precision experimental measurements become available.

Fig. 6.9 shows the range of values found for the phase and magnitude of the NP contribution to C_7^{eff} during the parameter space exploration. It is shown at the weak scale, $\mu = m_W$. The colour index shows the mean probability of that point being compatible with current experimental results. Areas with probability greater than one σ are shaded red, while those below this are shaded blue. The outline of the one σ contour can be seen. For comparison, the values of the NP Wilson coefficients are shown for the SM, the FBMSSM and the GMSSM. All three models are compatible with current constraints. Similar figures are shown for the other Wilson coefficients in Figs 6.10 and 6.11. The allowed regions of parameter space are still large.

The ensemble of constrained NP models can also be used to explore the likely values of $q_0^2(A_{\text{FB}})$ and $q_0^2(S_5)$. It was found that eight percent of parameter space points considered had no A_{FB} zero in the range $q^2 \in [0.5, 15]\,\text{GeV}^2/c^4$, and twelve percent for S_5. Theoretical uncertainties are not well controlled over this q^2 range, however, the majority of points within the one σ contour lie in the theoretically clean region, $q^2 \in [1, 6]\,\text{GeV}^2/c^4$. The distribution can be seen in Fig. 6.12a. Fig. 6.12b shows the distribution of A_{FB} and S_5 gradients at their zero-crossing points. There is a clear linear relationship. We find for the majority of points, $G_0(S_5)$ is greater than $G_0(A_{\text{FB}})$. This suggests that the improvement on the experimental resolution of $q_0^2(S_5)$ relative to $q_0^2(A_{\text{FB}})$ is a general feature of the

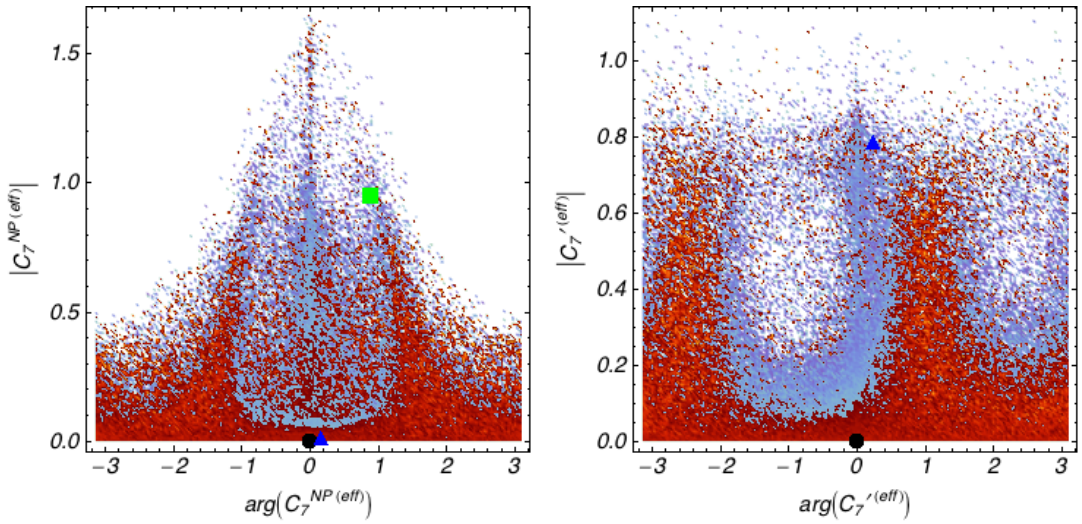

(a) C_7^{eff} (b) $C_7'^{\text{eff}}$

Figure 6.9: Allowed parameter space for the NP contribution to the Wilson coefficients C_7^{eff} and $C_7'^{\text{eff}}$ at m_W. The SM point lies at the origin and is marked with a black point. The SM point is shown in black at the origin, while the FBMSSM is a green square and the GMSSM is an blue triangle. These models are introduced in Chap. 5. The colour of each point in parameter space denotes the mean degree of compatibility between current measurements and the sets of observables which fall into that particular $\{\text{abs}(C_7^{(\prime)\,\text{eff NP}}), \arg(C_7^{(\prime)\,\text{eff NP}})\}$ bin. Points with a compatibility with data of sixty-eight percent or better are drawn with a red colour pallet, while those less compatible than this are shown with a blue pallet. All points are required to have a compatibility with data better than five percent.

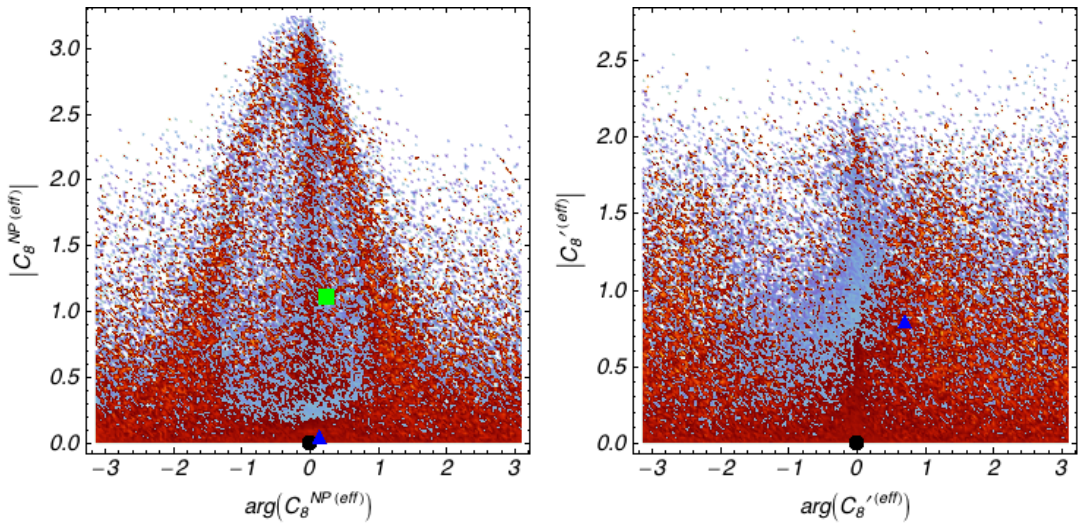

(a) C_8^{eff} (b) $C_8'^{\text{eff}}$

(c) C_9^{eff} (d) $C_9'^{\text{eff}}$

Figure 6.10: Allowed parameter space for the Wilson coefficients $C_{8,9}^{(\prime)\,\text{eff}}$ after applying 2009 $b \to s$ experimental constraints. The colour coding is the same as in Fig. 6.9.

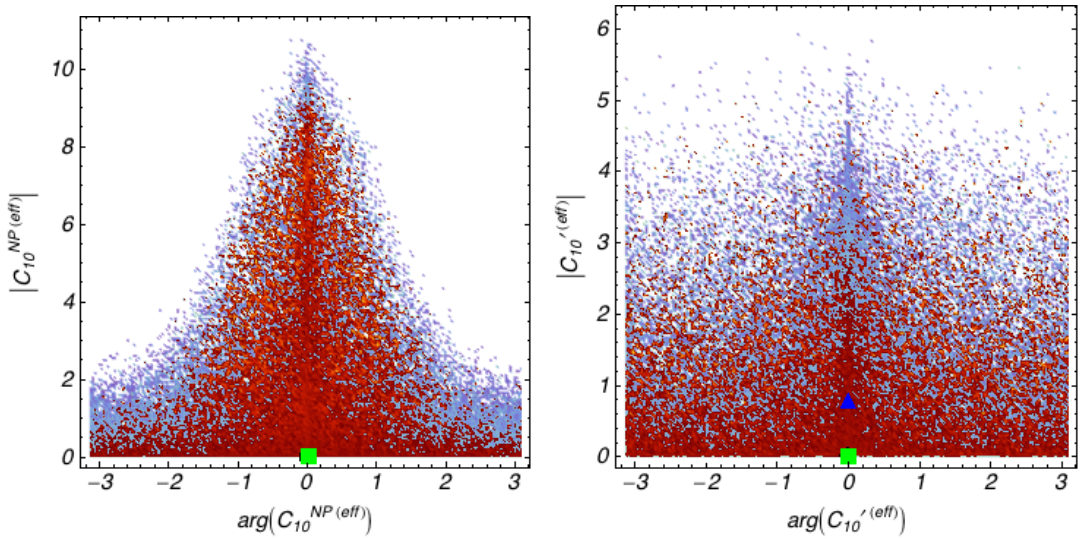

(a) $C_{10}^{\rm eff}$ (b) $C_{10}^{\prime\,\rm eff}$

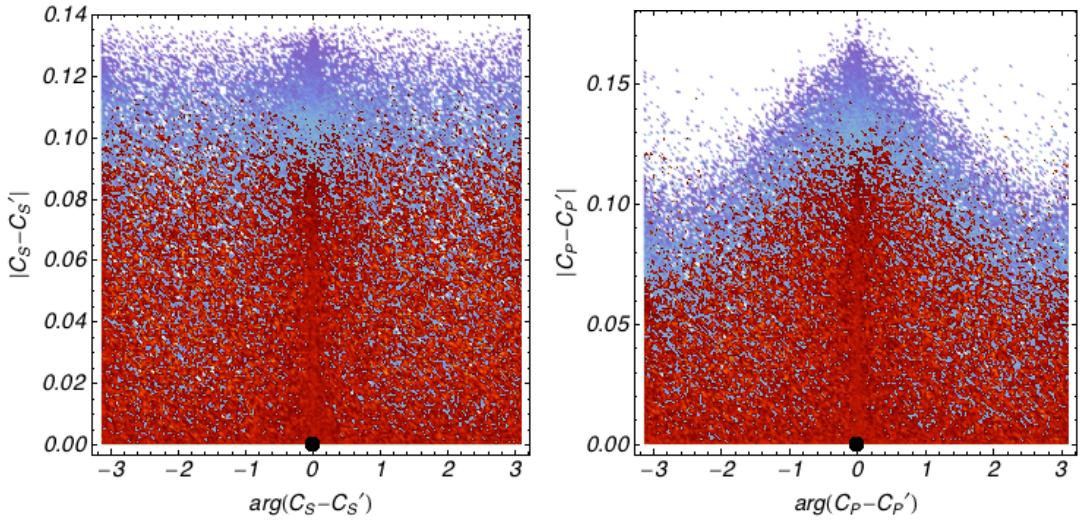

(c) $(\mathcal{C}_S - \mathcal{C}'_S)$ (d) $(\mathcal{C}_P - \mathcal{C}'_P)$

Figure 6.11: Allowed parameter space for the Wilson coefficients $C_{10}^{\prime\,\rm eff}$, $(\mathcal{C}_S - \mathcal{C}_S)$, and $(\mathcal{C}_P - \mathcal{C}_P)$ after applying 2009 $b \to s$ experimental constraints. The colour coding is the same as in Fig. 6.9.

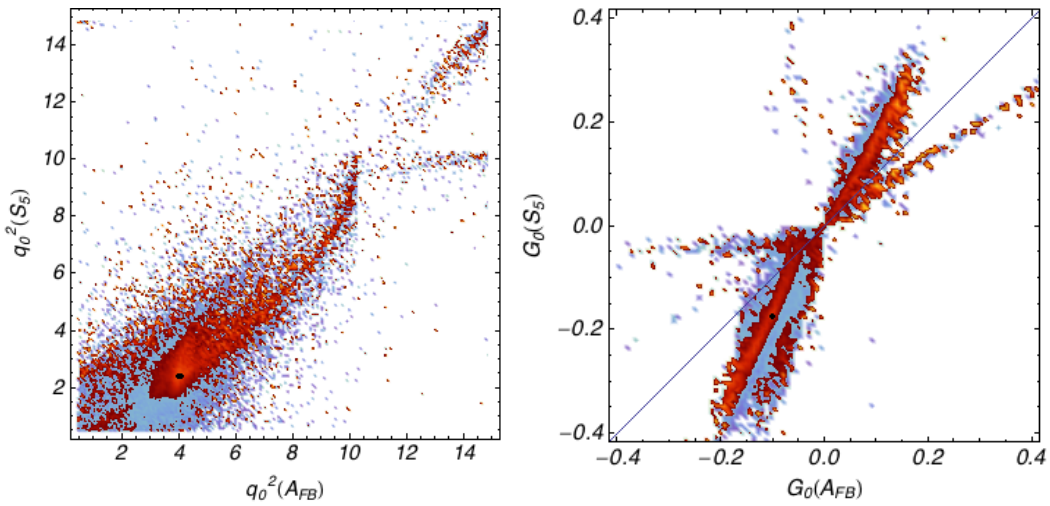

(a) (b)

Figure 6.12: Fig. (a) shows allowed values of the $A_{\rm FB}$ and S_5 zero-crossing points in the range $q^2 \in [0.5, 15]\,{\rm GeV}^2/c^4$. The SM point and its uncertainty is shown as a black ellipse. Fig. (b) shows the gradient of the $A_{\rm FB}$ and S_5 at the zero-point. In each case the colour index has the same meaning as in Fig. 6.9.

decay and not just a property of the SM. Analysis of the soft form factors shows that this prediction is robust [7].

6.7 Experimental impact

The relative impact of the different analyses presented in Sec. 4.1 can be assessed by again considering the results of the parameter space exploration performed in Sec. 6.6. It is assumed that LHCb will make $2\,{\rm fb}^{-1}$ measurements of the observables $\langle A_{\rm FB}\rangle_{1-6\,{\rm GeV}^2}$, $\langle S_5\rangle_{1-6\,{\rm GeV}^2}$, $\langle F_{\rm L}\rangle_{1-6\,{\rm GeV}^2}$, $q_0^2(A_{\rm FB})$ and $q_0^2(S_5)$ and that the resultant experimental uncertainties are symmetrized versions of those given in Tab. 6.1. In addition, we assume that there is no NP present in $b \to s$ decays and that the extracted value of each observable is as given in Tab. 6.2. The total χ^2 for each point in parameter space is then updated to reflect the hypothetical SM measurements. Where individual measurements are superseded they are replaced with no attempt at combination. However, other current constraints such as $\mathcal{B}(B \to X_s\gamma)$ are included as before. The constraining power of each analysis can then be compared.

Fig. 6.13 shows the relative impact of these measurements on the NP component of $C_7^{\rm eff}$. In Fig. 6.13a, SM values of $\langle A_{\rm FB}\rangle_{1-6\,{\rm GeV}^2}$ and $q_0^2(A_{\rm FB})$ are imposed with the estimated $2\,{\rm fb}^{-1}$ experimental sensitivities taken from Tab. 6.1. Fig. 6.13b shows the impact of $\langle F_{\rm L}\rangle_{1-6\,{\rm GeV}^2}$ and Fig. 6.13c of $\langle S_5\rangle_{1-6\,{\rm GeV}^2}$ and $q_0^2(S_5)$ for the same LHCb integrated luminosity. These should be compared with

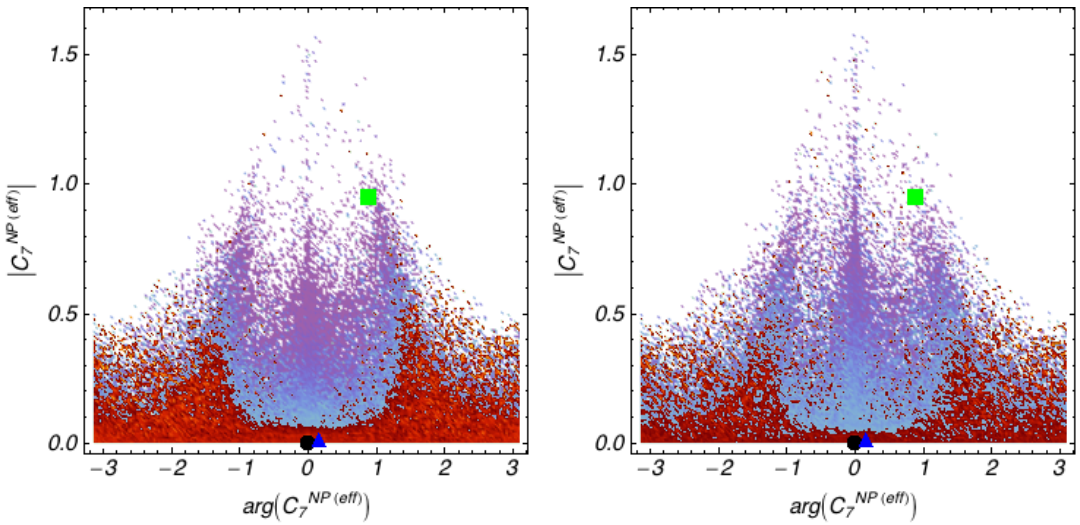

(a) $\langle A_{\rm FB}\rangle_{1-6\,{\rm GeV}^2}$ & $q_0^2(A_{\rm FB})$ (b) $\langle F_{\rm L}\rangle_{1-6\,{\rm GeV}^2}$

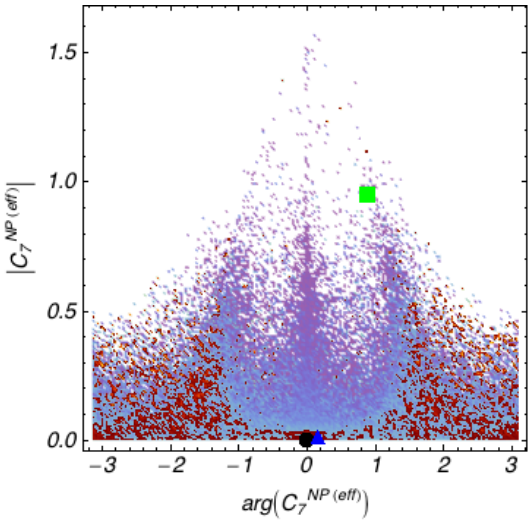

(c) $\langle S_5\rangle_{1-6\,{\rm GeV}^2}$ & $q_0^2(S_5)$

Figure 6.13: The relative impact of different proposed LHCb measurements after $2\,{\rm fb}^{-1}$ of integrated luminosity, assuming the SM, on the NP component of $C_7^{\rm eff}$. In each case the colour index has the same meaning as in Fig. 6.9.

the currently allowed parameter space for C_7^{eff}, shown in Fig. 6.9. The small statistical uncertainty shown in Tab. 6.1 for $q_0^2(S_5)$ allows for a stringent constraint on parameter space to be made.

Fig. 6.14 shows the combined effect of the proposed measurements, again assuming the SM and the estimated sensitivities from Tab. 6.1 on the NP components of the Wilson coefficients C_7^{eff}, $C_7^{\prime\text{eff}}$, C_9^{eff} and $C_{10}^{\prime\text{eff}}$. These are relevant for S_5. The other Wilson coefficient components are shown in Figs 6.15 and 6.16. The amount of parameter space left after these measurements would be significantly reduced. Most NP contributions would lie outside the one σ contour unless there are significant NP weak phases present. This again illustrates the importance of *CP*-asymmetries, as described in [106]. The FBMSSM and GMSSM models would be excluded by these measurements alone. The UED could also be excluded if proposed LHCb measurements of $\mathcal{B}(B_s \to \mu^+\mu^-)$ were included [8].

6.8 Summary

In this chapter, angular observables in the decay distribution of $\overline{B}_d \to \overline{K}^{*0}(\to K\pi)\mu^+\mu^-$ have been studied with emphasis on finding suitable measurements for the first few years of LHCb data taking. Techniques to extract the observables A_{FB}, F_{L}, S_3, S_5, A_7 and A_9 have been presented. Two different approaches have been investigated. The first, where a q^2 integrated value is extracted, is suitable for making both precision and low-statistics measurements. The other, where the q^2 dependence is also mapped out, offers additional NP discrimination once data set sizes increase and allows for zero crossings to be extracted where available. The sensitivity to the A_{FB} and S_5 zero crossings have been found. It was shown that the sensitivity to $q_0^2(S_5)$ should be considerably better than for $q_0^2(A_{\text{FB}})$, as the ratio $G_0(S_5)/G_0(A_{\text{FB}})$ is close to two in the SM.

An analysis of the parameter space allowed by experimental constraints has been presented. There is significant room for NP contributions to $b \to s$ transitions, especially if extra weak phases from beyond the CKM mechanism are present. It was also shown that the ratio of $G_0(S_5)/G_0(A_{\text{FB}})$ will be greater than one for most allowed areas of parameter space, if current form factor predictions and uncertainties are upheld.

By applying the results of hypothetical SM results, the impact of making $2\,\text{fb}^{-1}$ LHCb measurements was assessed. $\langle A_{\text{FB}}\rangle_{1-6\,\text{GeV}^2}$, $\langle F_{\text{L}}\rangle_{1-6\,\text{GeV}^2}$, $\langle S_5\rangle_{1-6\,\text{GeV}^2}$, $q_0^2(A_{\text{FB}})$, and $q_0^2(S_5)$ all provide useful and complementary constraints, enabling a number of the specific NP models considered in Chap. 5 to be excluded. The constraining power of S_5 was particularly significant due to the projected smallness of the $q_0^2(S_5)$ uncertainty. Thus, it is recommended that an analysis of S_5 is

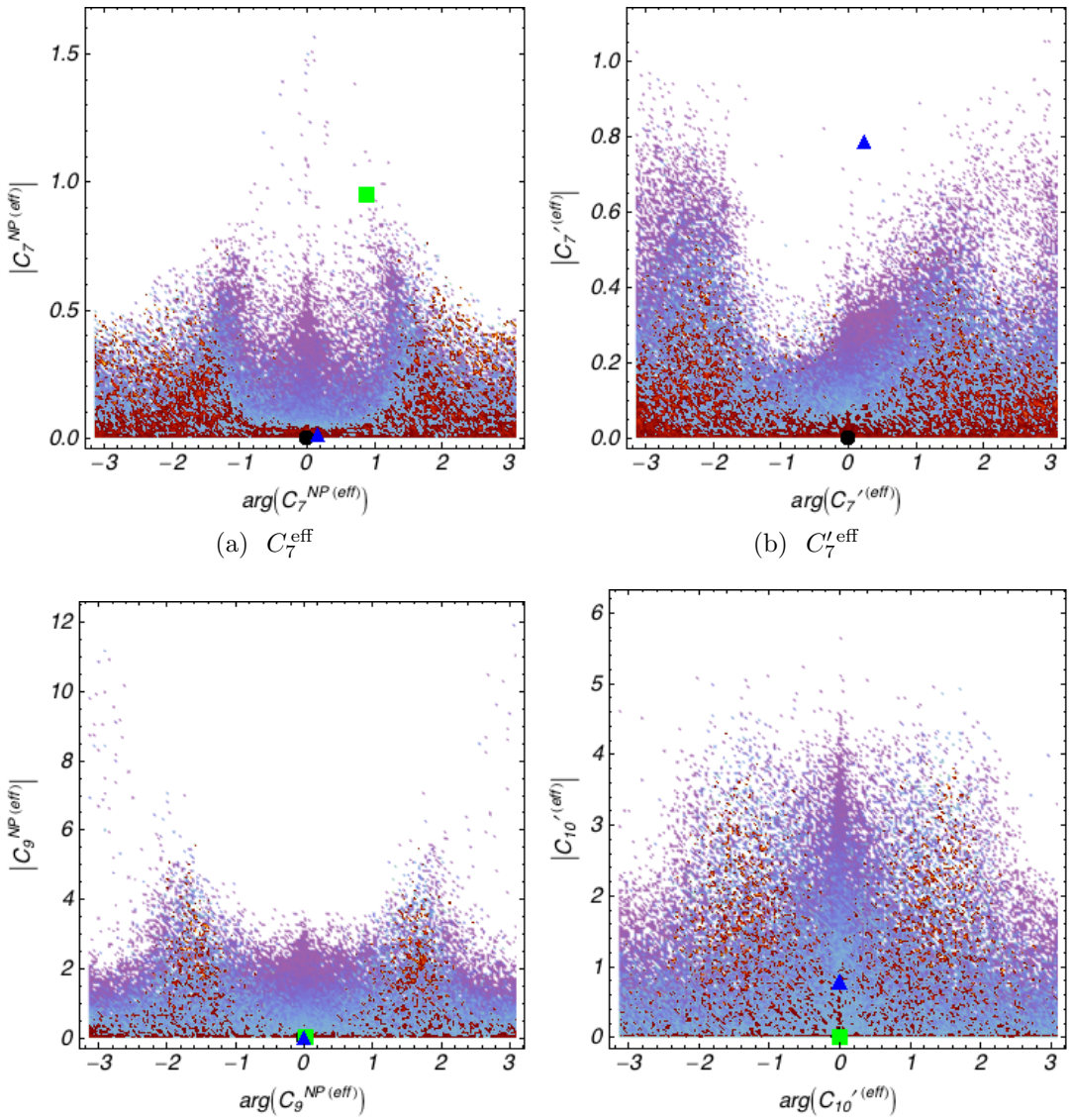

(a) C_7^{eff} (b) $C_7'^{\text{eff}}$

(c) C_9^{eff} (d) $C_{10}'^{\text{eff}}$

Figure 6.14: Allowed parameter space for the Wilson coefficients C_7^{eff}, $C_7'^{\text{eff}}$, C_9^{eff} and $C_{10}'^{\text{eff}}$ after $2\,\text{fb}^{-1}$ measurements at LHCb of $\langle F_{\text{L}}\rangle_{1-6\,\text{GeV}^2}$, $\langle A_{\text{FB}}\rangle_{1-6\,\text{GeV}^2}$, $q_0^2(A_{\text{FB}})$, $\langle S_5\rangle_{1-6\,\text{GeV}^2}$ and $q_0^2(S_5)$, assuming the SM. The colour coding is the same as in Fig. 6.9.

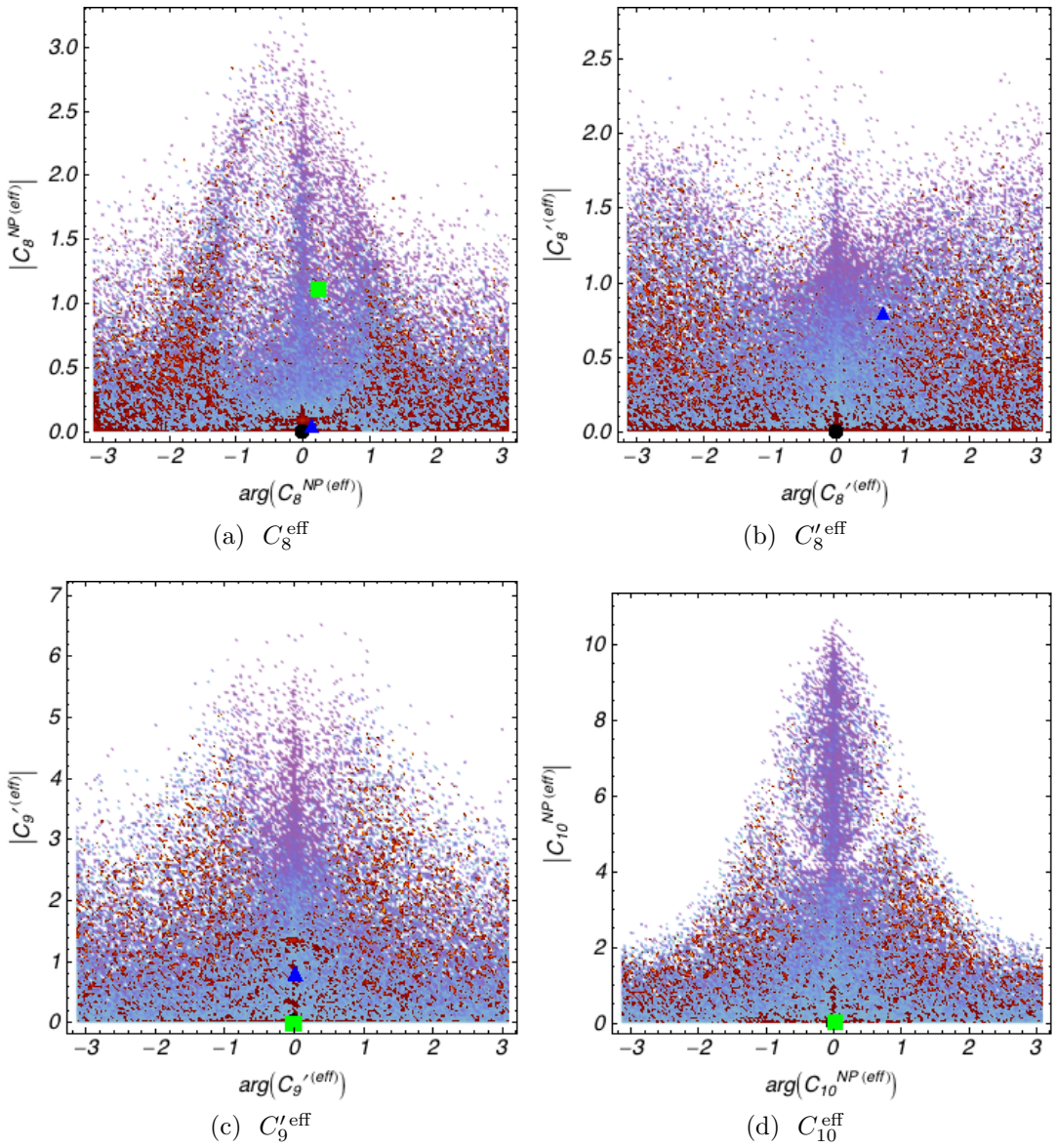

(a) C_8^{eff} (b) $C_8'^{\text{eff}}$

(c) $C_9'^{\text{eff}}$ (d) C_{10}^{eff}

Figure 6.15: Allowed parameter space for the Wilson coefficients C_8^{eff}, $C_8'^{\text{eff}}$, $C_9'^{\text{eff}}$, and C_{10}^{eff} after $2\,\text{fb}^{-1}$ measurements at LHCb of $\langle F_{\text{L}}\rangle_{1-6\,\text{GeV}^2}$, $\langle A_{\text{FB}}\rangle_{1-6\,\text{GeV}^2}$, $q_0^2(A_{\text{FB}})$, $\langle S_5\rangle_{1-6\,\text{GeV}^2}$ and $q_0^2(S_5)$, assuming the SM. The colour coding is the same as in Fig. 6.9.

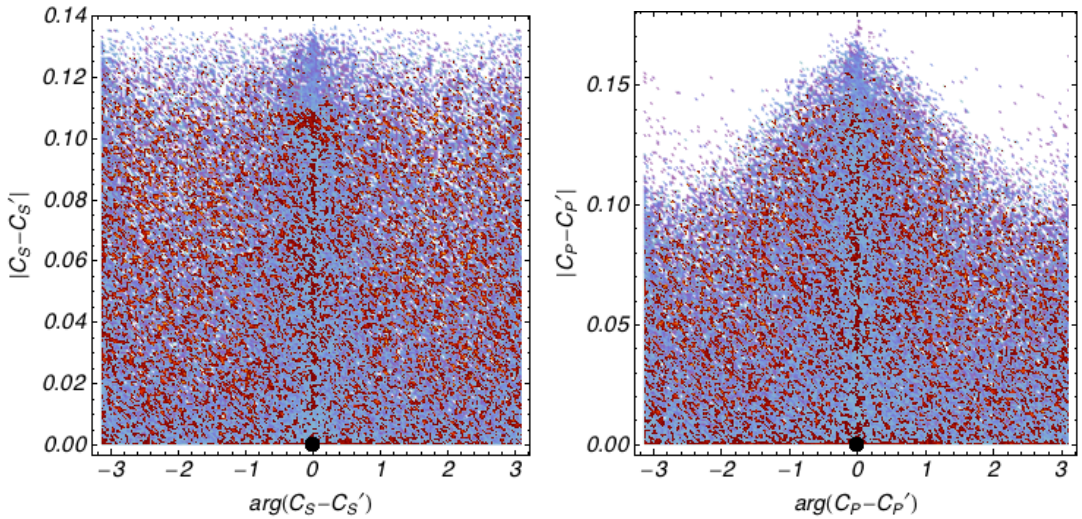

(a) $\mathcal{C}_S - \mathcal{C}'_S$ (b) $\mathcal{C}_P - \mathcal{C}'_P$

Figure 6.16: Allowed parameter space for the Wilson coefficients $(\mathcal{C}_S - \mathcal{C}_S)$ and $(\mathcal{C}_P - \mathcal{C}_P)$ after $2\,\text{fb}^{-1}$ measurements at LHCb of $\langle F_\text{L}\rangle_{1-6\,\text{GeV}^2}$, $\langle A_\text{FB}\rangle_{1-6\,\text{GeV}^2}$, $q_0^2(A_\text{FB})$, $\langle S_5\rangle_{1-6\,\text{GeV}^2}$ and $q_0^2(S_5)$, assuming the SM. The colour coding is the same as in Fig. 6.9.

performed with the first few years of LHCb data in addition to those of A_FB and F_L already planned [8].

Chapter 7

Conclusions

At the time of writing this thesis, the LHC was just starting its 2010 run. It is to be hoped that this will herald the start of a new era of discovery in HEP. There are many long-standing problems with our current model of weak interactions; however, the overall picture is one of amazing consistency between experimental measurements and SM predictions. It seems unlikely that the SM is valid to the Planck scale; it must break down at some energy. It is reasonable to think that this will occur at the TeV scale, and that we may see light shed on the mechanisms behind the electroweak symmetry breaking at the LHC.

The evidence for the existence of massive *dark matter* on cosmological scales with significantly suppressed EM interactions is increasingly convincing – there is something new to discover (see Fig. 1.1). There is no guarantee that this discovery will be in collider physics; however, we can interpret the cosmological relic density of dark matter as a *hint* that there are new massive particles to study on weak scales.

Flavour physics offers a direct connection to the mechanisms behind electroweak symmetry breaking in the SM through the Yukawa couplings. The unexplained hierarchy of the CKM matrix, shown in Eq. (1.30), as well as the huge t-quark mass means that if there are weak scale NP effects, they might be seen in the interactions of the third generation.

This thesis has been focused on the discovery of NP in the $b \to s$ quark transition through the study of rare electroweak decays. These are governed by the CKM elements V_{tb} and V_{ts} and are dominated by loop effects, giving sensitivity to new massive virtual particles that might be present. The effects of current $b \to s$ observables were considered in Sec. 6.6 where it was shown that the NP parameter space is still large. The b-quark production cross-section at the LHC is expected to be huge; even very rare decays can be studied in detail so that the allowed parameter space can be significantly reduced.

The LHCb detector, introduced in Chap. 2, has been developed to make pre-

cision measurements of B meson decays at the LHC. It is a single-arm spectrometer with highly specialized vertex tracking, PID from two RICH detectors, and an extensive muon system. It has been designed to operate at a luminosity of $2 \times 10^{32}\,\mathrm{cm}^{-2}\,\mathrm{s}^{-1}$, producing a proton-proton interaction rate of 10 MHz. This must be reduced to 2 kHz for storage; this is achieved with a two-level trigger. The first level uses custom hardware to select high E_T hadrons and photons as well as high p_T muons. The second then uses the full detector read-out to analyse events in software. The detector provides excellent B mass and track momentum resolutions, allowing many rare B decays to be selected with high efficiency.

$\overline{B}_d \to \overline{K}^{*0}\mu^+\mu^-$ is a rare electroweak penguin decay that will be recorded thousands of times a year by LHCb. The presence of four charged tracks in the final state mean that it can be selected with relative ease, and gives access to the angular distribution, the study of which has been of primary concern in this thesis. The decay has been introduced in Sec. 1.4, and many of the features of LHCb that allow for its detection described in Chap. 2. It is commonly studied in the framework of OPE, introduced in Sec. 1.3.1, using HQET, described in Sec. 1.3.2. A model-independent treatment of the full-angular distribution can then be derived in terms of three decay angles and one invariant mass. Several measurements of the decay have been made at *BABAR*, Belle, and CDF, but, given current experimental uncertainties, they are in good agreement with SM predictions.

The properties of the $\overline{B}_d \to \overline{K}^{*0}\mu^+\mu^-$ angular distribution were discussed in Sec. 3.1, and a selection of observables that have reduced theoretical uncertainties in certain areas of phase space were introduced in Sec. 3.3. It was shown that these observables may, in principle, be measured by considering the symmetries of the angular distribution in Sec. 3.2. That the NP sensitivity they provide is enough when theoretical uncertainties are taken into account was verified in Sec. 3.5.4 and Ref. [1]. In addition, it was shown that the estimates of theoretical uncertainties coming from $\Lambda_{\mathrm{QCD}}/m_b$ corrections, which are expected to be the dominant source of theoretical uncertainty, are not as large as previously thought; NP effects could in principle be distinguished using these observables.

An important tool in developing these measurements will be simulations of $\overline{B}_d \to \overline{K}^{*0}\mu^+\mu^-$ decays in the LHCb detector. A new model was developed as a plug-in for EvtGen that allows simulation of the signal angular distribution, both in the SM and model independently with NP. The EvtGen framework was introduced in Sec. 5.1.1, and then the theoretical framework was specified in Sec. 5.2 in a way that allows comparison with the previous generation of decay models. The performance of the model was studied and it was shown that it is good enough to be used in LHCb MC productions, as discussed in Sec. 5.3.

In the first few years of LHC running, it will be important to focus on those observables which are relatively straight-forward to measure. The most widely studied of these observables is $A_{\rm FB}$, defined in Eq. (6.6). This can be found by counting the number of signal events with $\cos\theta_\ell$ greater than zero and less than zero, and then forming an asymmetry. In the SM, this vanishes at some point in q^2, known as the zero-crossing point, $q_0^2(A_{\rm FB})$. The value of the zero-crossing has reduced hadronic uncertainties in the large recoil limit, due to the LO cancellation of the universal *heavy-to-light* form factors, as explained in Sec. 3.3. The extraction of the zero-crossing has attracted significant study at LHCb.

There are a number of other observables that may be found in a similar way, taking asymmetries in angular bins of one or more decay angles, as introduced in Secs. 6.2 and 6.3. These observables were studied in a simplified analysis framework that allowed for a fair comparison to be made between them. It was shown that the zero-crossing of the observable S_5 can be found with small uncertainty due to the gradient of the S_5 distribution at that point, $G_0(S_5)$. Furthermore, it was demonstrated model independently in Sec. 6.6 that $G_0(S_5)$ is greater than $G_0(A_{\rm FB})$ for most of the allowed parameter space. This implies that $q_0^2(S_5)$ can often be found with an uncertainty smaller than that for $q_0^2(A_{\rm FB})$, despite the use of two decay angles. The implications for a $2\,{\rm fb}^{-1}$ measurement on parameter space were assessed; it was found that an S_5 measurement would be a useful addition to those already considered by LHCb.

In later years of LHCb running, the number of $\overline{B}_d \to \overline{K}^{*0}\mu^+\mu^-$ signal events may be great enough, and the detector well enough understood, to make a full-angular analysis of the decay. The general framework for doing this was considered in the first three sections of Chap. 3. A number of theoretically clean observables can be found which provide reduced hadronic theoretical uncertainties and excellent sensitivity to NP. A fitting methodology was developed in Sec. 4.1 that allowed for estimates of the LHCb sensitivities to these observables with $10\,{\rm fb}^{-1}$ to be made, both for the SM and following the SUSY-b model. This work led to many of the conceptual issues associated with making fits of this kind being explored. It was shown in Sec. 4.3 that performing the full-angular analysis provided large improvements in the sensitivity to those observables available through angular projection fits; $A_T^{(2)}$ and $A_{\rm FB}$ both showed significant improvement. *CP*-asymmetries were also considered with the aim of imposing constraints on the NP phases of the Wilson coefficients active in the decay.

Correlations in the fit led to the discovery of an additional symmetry in the angular distribution. The implications of this were discussed in Sec. 4.6. It seems that while the sensitivity estimates shown in Chap. 4 are probably correct, the presence of a fourth symmetry means that a new fitting methodology must be

developed before this measurement can be made. The requirements for this are clear, however work must continue beyond the time-scale of this thesis. The full-angular analysis remains the ultimate goal of the $\overline{B}_d \to \overline{K}^{*0}\mu^+\mu^-$ physics programme at LHCb and has the potential to be one of the most interesting measurements performed with the detector.

In summary, this thesis has laid out the theoretical and experimental reasons to search for NP effects in the weak sector, and particularly in rare electroweak $b \to s$ penguin decays like $\overline{B}_d \to \overline{K}^{*0}\mu^+\mu^-$. Both the LHC project and the LHCb detector have been introduced. It has been shown that the allowed regions in parameter space for NP in $b \to s$ quark transitions are still relatively large, despite a number of interesting measurements already made at the B-factories and the TeVatron. A programme of measurements has been outlined that would take the LHCb collaboration from its first measurements of the decay to its last. Particular input to this has been made, showing that the S_5 zero-crossing is an excellent candidate for study in the first few years of running, and providing many details on how to perform a full-angular analysis with larger data sets. In addition, a new decay model was been developed which will allow the study of experimental effects in the presence of NP. The author is now keenly awaiting the first results from LHCb.

Appendix A

Results of full-angular analysis

In this appendix, additional results for the full-angular analysis described in Chap. 4 are presented. Firstly, Fig. A.1 shows the fit-quality of an example $10\,\text{fb}^{-1}$ SM three-symmetry fit directly. The actual toy data set used in the fit is shown; the figure shows the distributions of all four experimental observables. Numerical projections of the full-angular PDF must be used in order to make a direct comparison between the input data and the extracted distributions. The solid red line shows the input distribution from which the toy data was generated using an accept/reject algorithm. The blue line shows the distribution obtained by performing the full-angular fit. The agreement between these two lines is excellent for the θ_ℓ and θ_{K^*} distributions, and slightly worse for ϕ. The largest discrepancy is in the q^2 distribution. This may be due to a failure of the polynomial parametrization, and is particularly distinct at the high and low extremes of the q^2 window. The effect is, however, relatively small.

The other figures shown in this appendix give estimates for the statistical uncertainties obtainable with 2 and $100\,\text{fb}^{-1}$. These integrated luminosities are the nominal values expected after one year of LHCb data taking, and at the end of a SuperLHCb run. As explained in the main thesis body, full-angular fit convergence may be achieved with only $2\,\text{fb}^{-1}$ of integrated luminosity. Whether an analysis can be made will depend on how well LHCb can be understood. Estimated sensitivities are also shown for an upgraded LHCb detector at the end of an extended run where $100\,\text{fb}^{-1}$ of integrated luminosity might be expected. In this case, the fit could provide extremely precise estimates for many angular observables.

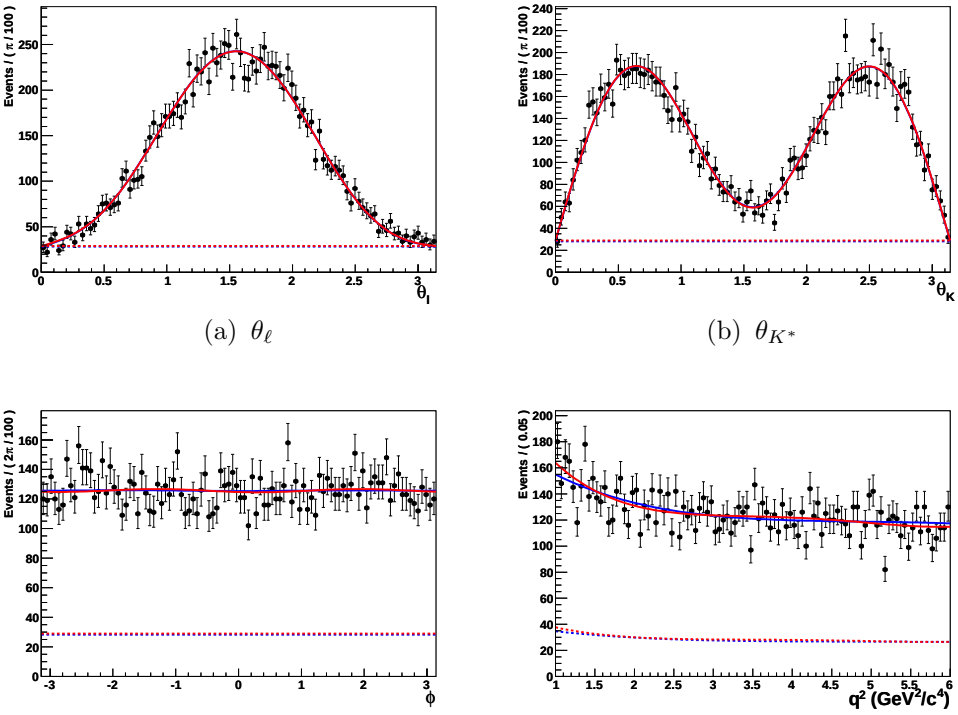

(a) θ_ℓ (b) θ_{K^*}

(c) ϕ (d) q^2

Figure A.1: Numerical projections of the full polynomial fit PDF over an example toy data set for each of the experimental observables. The points show a randomly chosen $10\,\text{fb}^{-1}$ data set, generated assuming the SM as described in Sec. 4.1.2. The solid red line shows numerical projections over this data set with the full-angular polynomial PDF, described in Sec. 4.1.1, with its parameters set via a fit to the data set. The dashed line shows only the background contribution. Underlayed on each plot is the blue line showing the input PDF. The parameters of this PDF have been set by performing a polynomial fit to each of the K^{*0} spin amplitudes. Comparing these two lines we see that the full-angular fit is able to extract the PDF parameters with good accuracy. The differences are largest for the q^2 distribution.

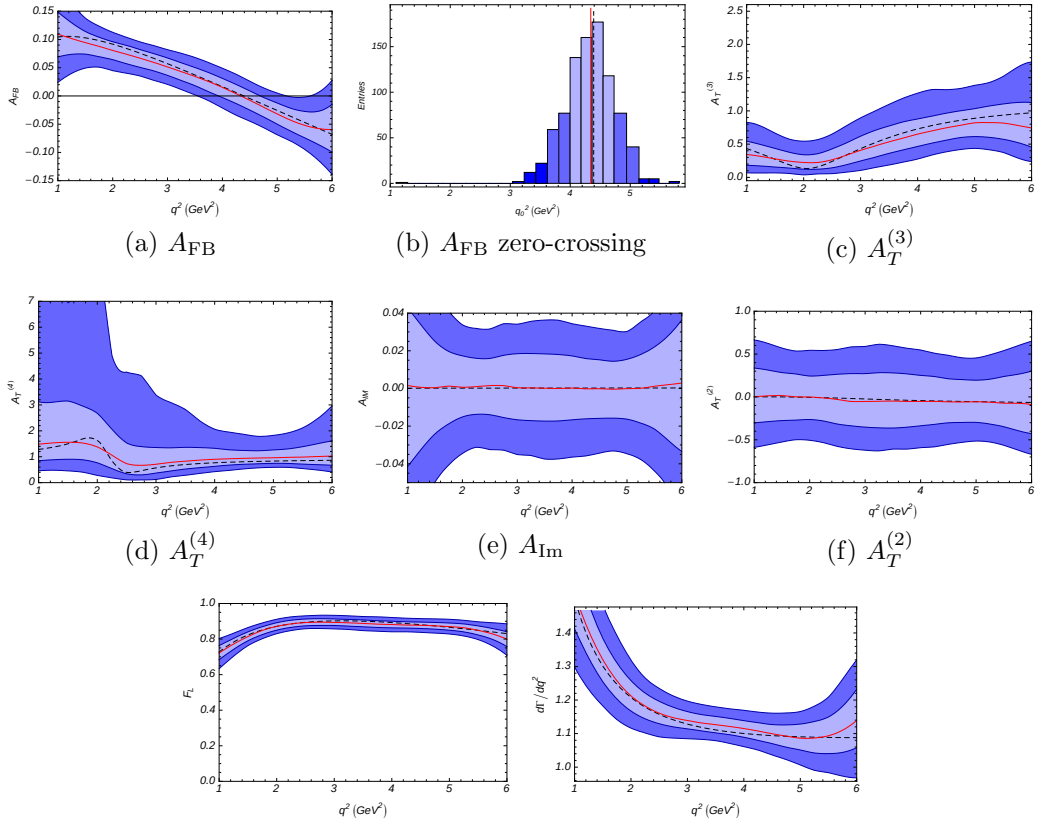

(a) A_{FB} (b) A_{FB} zero-crossing (c) $A_T^{(3)}$

(d) $A_T^{(4)}$ (e) A_{Im} (f) $A_T^{(2)}$

(g) F_{L} (h) Γ'

Figure A.2: Estimated experimental sensitivities for $2\,\mathrm{fb}^{-1}$ of LHCb data assuming the SM. The zero-crossing point extracted from (b) is $4.32^{+0.37}_{-0.35}\,\mathrm{GeV}^2/c^4$. The colour scheme is the same as in Fig. 4.1.

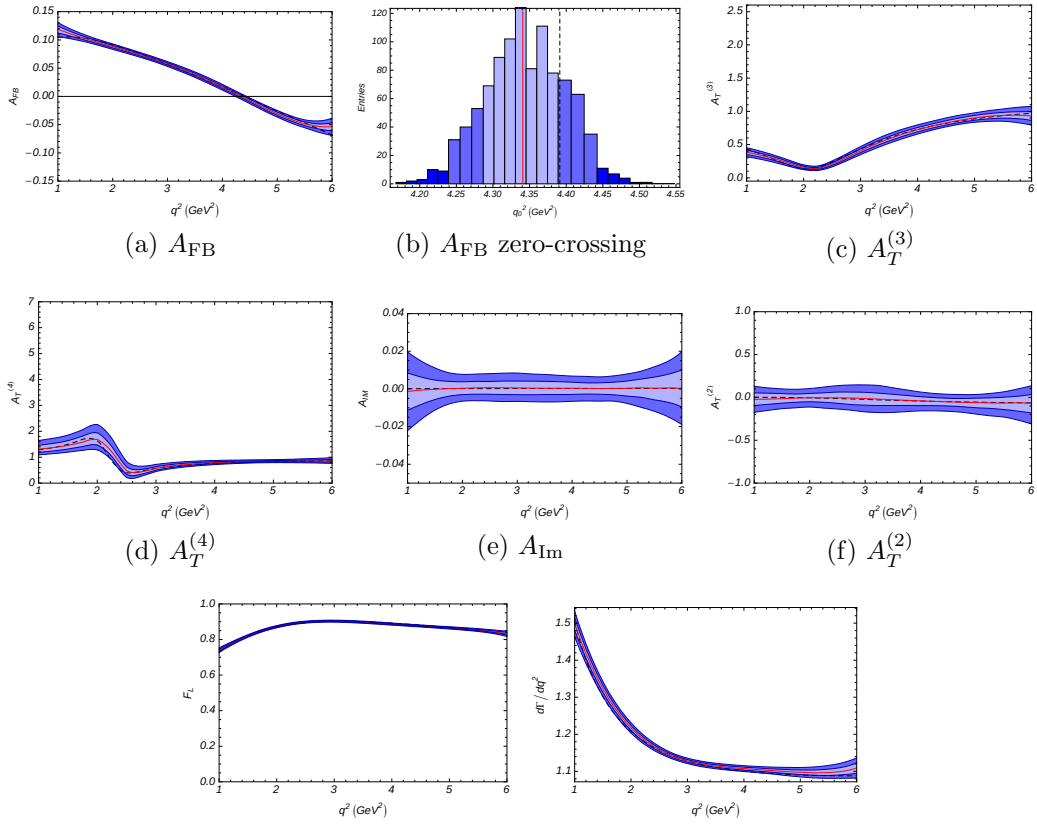

(a) $A_{\rm FB}$ (b) $A_{\rm FB}$ zero-crossing (c) $A_T^{(3)}$

(d) $A_T^{(4)}$ (e) $A_{\rm Im}$ (f) $A_T^{(2)}$

(g) $F_{\rm L}$ (h) Γ'

Figure A.3: Estimated experimental sensitivities for $100\,\text{fb}^{-1}$ of LHCb data assuming the SM. The zero-crossing point extracted from (b) is $4.345^{+0.052}_{-0.049}\,\text{GeV}^2/c^4$; the bias on its value is now significant and could perhaps be improved by increasing the order of the polynomials used in the full-angular fit. The colour scheme is the same as in Fig. 4.1.

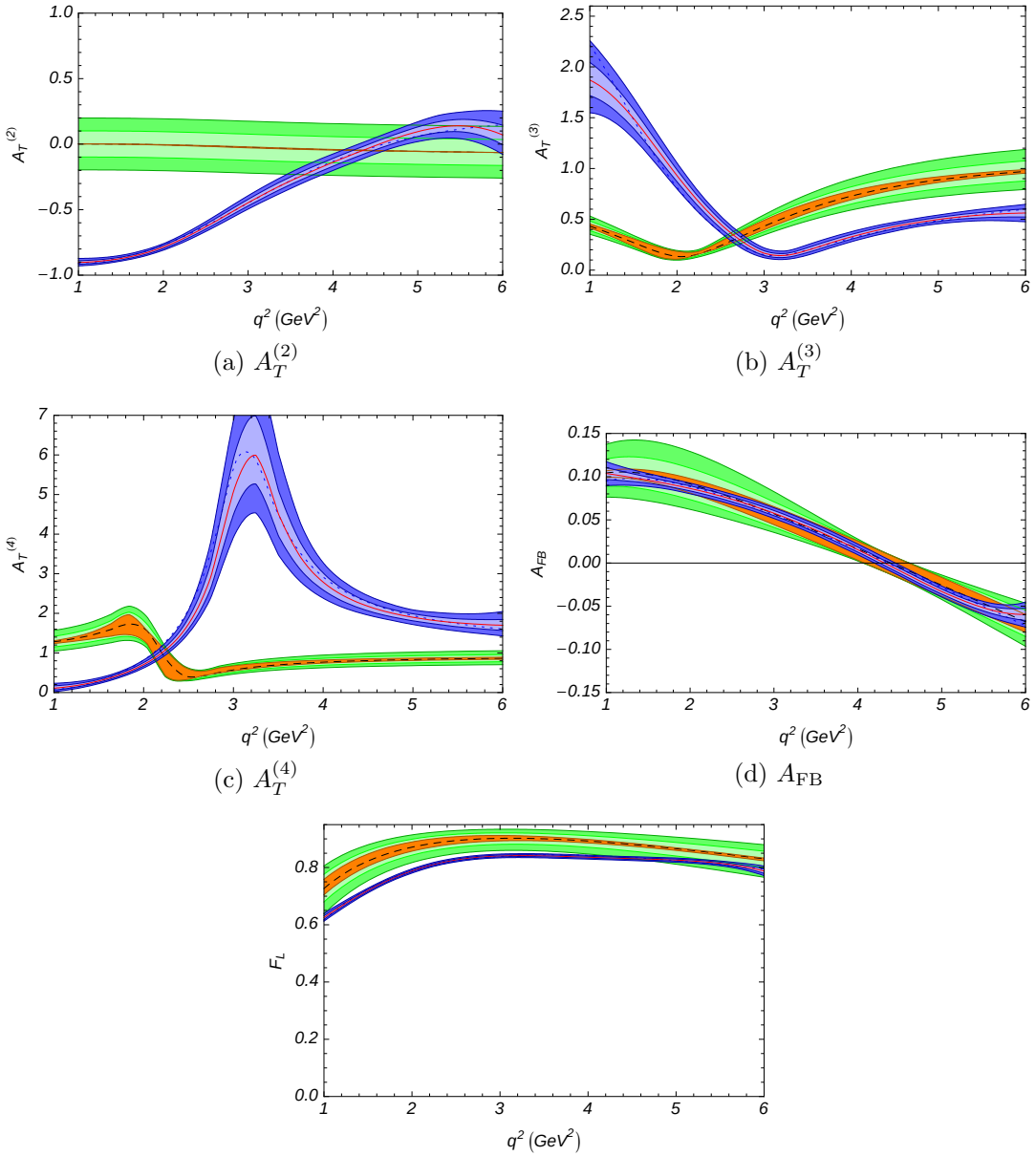

(a) $A_T^{(2)}$ (b) $A_T^{(3)}$

(c) $A_T^{(4)}$ (d) A_{FB}

(e) F_{L}

Figure A.4: Comparison between the estimated experimental sensitivities to $A_T^{(2)}$, $A_T^{(3)}$, $A_T^{(4)}$, A_{FB} and F_{L} and the theoretical SM distribution for $100\,\mathrm{fb}^{-1}$ of LHCb data assuming the SUSY-b scenario. The colour scheme is the same as in Fig. 4.6.

Appendix B

Model commands and decay files

In this appendix, more detailed information of how to control the decay model described in Chap. 5 will be presented. The model may be configured at run time using commands in the EvtGen decay file. The syntax of this file has been extended with a dedicated parser so that different physics models, form factors, and options may be selected without recompiling the model. An example of this is shown in Fig. B.1. A summary of the available commands is given in Tab. B.1, and extra information is given below.

```
Alias      MyK*0       K*0
Alias      Myanti-K*0  anti-K*0
ChargeConj Myanti-K*0  MyK*0
EVTBTOKSTARLLDURHAM07_MODEL physicsModel(UED_Model),calcConstraints(1)
Decay B0sig
  1.000  MyK*0  mu+ mu-     EVTBTOKSTARLLDURHAM07;
Enddecay
CDecay anti-B0sig
Decay MyK*0
  1.000         K+ pi-      VSS;
Enddecay
CDecay Myanti-K*0
End
```

Figure B.1: An example decay file for $B_d \to K^{*0}\mu^+\mu^-$ with $K^{*0} \to K\pi$. The first decay is done with the new `EVTBTOKSTARLLDURHAM07` decay model, while the second is done with the generic `VSS` model, which models resonant vector to scalar scalar decay. Additional commands are passed to the model with the command `EVTBTOKSTARLLDURHAM07_MODEL`. This accepts a comma separated list of setting commands. The supported commands are given in Tab. B.1.

- `calcConstraints`: Calculate a set of experimental constraints for using the selected physics and form factor models. Values are found for the zero-crossing points of $A_{\rm FB}$, S_4 and S_5, the rate averages of $A_{\rm FB}$, $F_{\rm L}$ and S_5 in the

Command	Valid Arguments	Default Value
`calcConstraints(logical)`	0 or 1	0
`formFactorModel(number)`	See Tab. B.2.	0
`highq2Cut(q2)`	$4m_\mu^2 \leq q^2 \leq (m_B - m_{K^{*0}})^2$	$(m_B - m_{K^{*0}})^2$
`lowq2Cut(q2)`	$4m_\mu^2 \leq q^2 \leq (m_B - m_{K^{*0}})^2$	$4m_\mu^2$
`physicsModel(name)`	See Tab. B.3.	`Standard_Model`
`wilsonCoefficients(list)`	See Sec. B.1.	SM values
`writeProbProfile(logical)`	0 or 1	0

Table B.1: Model commands, their arguments and default values.

range $q^2 \in [1\,\mathrm{GeV}^2/c^4, 6\,\mathrm{GeV}^2/c^4]$, $\mathcal{B}(B_s \to \mu\mu)$, $\mathcal{B}(B \to X_s\gamma)$, $\mathcal{B}(B \to X_s\ell\ell)$ and, $S_{CP}(B \to K^{*0}\gamma)$. More details are given in Chap. 6.

- `formFactorModel`: The particular model for the vector form factors used will affect physical observables in a way which may produce better or worse sensitivities than will be obtained from actual measurements - see e.g. Ref. [2]. Several form factor models are provided so that this can be explored however their use in production is not recommended.

- `high/lowq2Cut`: EvtGen requires each model to report the maximum probability it could produce. The maximum probability is found by sampling the available phase space as a function of q^2. The `highq2Cut` and `lowq2Cut` commands allow for bounds to be put on the region sampled in order to cut-off poles and very low and high q^2.

- `physicsModel`: A number of new physics models have been provided as sets of Wilson coefficients at m_W. Additional new physics models can be added at run time by making use of the `Generic_Model`. See Sec. B.1.

- `writeProbProfile`: If this option is set, the probability profile used to set the maximum probability will be written to a file. These files may be of particular interest in the case that a particular NP model is generating with very low efficiency. Example output from this routine can be seen in Fig. 5.3 for the benchmark physics models.

B.1 The generic physics model

New physics models can be added at run-time by specifying a set of Wilson coefficients at m_W. These may include those with complex values. Wilson coefficients not explicitly set will default to their SM values. It is also possible to modify

Model	Ref	Number
Ball '07	[56][a]	0
Ali '01	[69]	1
Ball '05	[104]	2
Beneke '05	[74, 113]	3

[a]Private communication. Statistically compatible but slightly modified version of that used in reference.

Table B.2: Available form factor models with references. The entries in the column 'Number' are the arguments to the command `formFactorModel(n)` needed to activate that model.

a given SM Wilson coefficient from its SM value by a scaling factor using the operators `+=`, `-=`, `*=` and, `/=`. For clarity, $\mathcal{C}_x \equiv$ `LX` and $\mathcal{C}'_x \equiv$ `RX` where x can be in the range 1-12 for left-handed coefficients and 7-10 for right-handed version (`L11` $\equiv \mathcal{C}_{Q_1} = (\mathcal{C}_S - \mathcal{C}'_S)$ and `L12` $\equiv \mathcal{C}_{Q_2} = (\mathcal{C}_P - \mathcal{C}'_P)$). Each coefficient must be followed by a colon.

```
physicsModel(Generic_Model),wilsonCoefficients(L7*1.05:R9=0.34-i0.78:)
```

In the following example, $\mathcal{C}_7(m_W) = 1.05 \times \mathcal{C}_7(m_W)^{\rm SM}$ and $\mathcal{C}'_9(m_W) = 0.34 - 0.78i$. Wilson coefficient indices out of the range $i \in \{1, .., 12\}$ will throw an exception at run time.

Model	Name
FBMSSM	`FBMSSM_Model`
Generic	`Generic_Model`
GMSSM	`GMSSM_Model`
LHT	`LHT_Model`
SM	`Standard_Model`
UED	`UED_Model`

Table B.3: The physics model to be used can be specified in the model decay file using the command `physicsModel(Name)` where the appropriate `Name` is shown for each model appearing in Tab. 5.3.

Appendix C

List of acronyms

CDF Collider Detector at Fermilab

CERN Organisation Européenne pour la Recherche Nucléaire

CKM Cabibbo-Kobayashi-Maskawa

$\sqrt{s}$ center-of-mass energy

CPU Central Processing Unit

ECAL electromagnetic calorimeter

HCAL hadronic calorimeter

EM electro-magnetic

FPGA field-programmable gate array

FBMSSM Flavour Blind MSSM

GMSSM General MSSM

FCNC flavour changing neutral current

GEM gas electron multiplier

GSL GNU Scientific Library

HEP High Energy Physics

HFAG Heavy Flavour Averaging Group

HLT High-Level Trigger

HQET heavy quark effective theory

HPD Hybrid Photon Detector

IP interaction point

IP8 Intersection Point 8

IT Inner Tracker

LØ Level-0

LEET large energy effective theory

LCSR Light Cone Sum Rules

LHC Large Hadron Collider

LHT Littlest Higgs with T-Parity

LO Leading Order

MC Monte Carlo

MCMC Markov Chain Monte Carlo

MFV Minimal Flavour Violation

MSSM Minimal Supersymmetric Standard Model

MWPC multiple-wire proportional chamber

NLL negative log-likelihood

NLO Next-to-Leading Order

NNLL Next-to-Next-to-Leading Log

NP new physics

OPE Operator Product Expansion

OT Outer Tracker

PDF parton distribution function

PDF probability density function

PDG Particle Data Group

PID particle identification

PMT photomultiplier tube

PSB Proton Synchrotron Booster

PS Proton Synchrotron

SPD/PS scintillator-pad detector/pre-shower

QCD Quantum Chromodynamics

QCDf QCD factorization

QED Quantum Electrodynamics

QFT quantum field theory

QM quantum mechanics

RF radio frequency

RGE Renormalisation Group equation

RICH Ring-Imaging Čerenkov

RMS root-mean square

SCET soft-collinear effective theory

SM Standard Model

SPS Super Proton Synchrotron

ST Silicon Tracker

STFC Science and Technology Research Council

SUSY Supersymmetry

TT Tracker Turicensis

UED Universal Extra Dimensions

VELO Vertex Locator

WIMP Weakly-Interacting Massive Particle

WMAP Wilkinson Microwave Anisotropy Probe

Bibliography

[1] U. Egede, T. Hurth, J. Matias, M. Ramon and W. Reece, *New observables in the decay mode* $\overline{B}_d \to \overline{K}^{*0}\mu^+\mu^-$, *JHEP* **11** (2008) 032 [0807.2589].

[2] W. Reece and U. Egede, "Performing the full-angular analysis of $\overline{B}_d \to \overline{K}^{*0}\mu^+\mu^-$ at LHC*b*." CERN-LHCb-2008-041.

[3] **LHC*b*** Collaboration, W. Reece, *Extracting angular correlations from the rare decay* $\overline{B}_d \to \overline{K}^{*0}\mu^+\mu^-$ *at LHC*b, *Phys. Atom. Nucl.* **72** (2009) 1543–1547.

[4] **LHC*b*** Collaboration, W. Reece, "Prospects for $\overline{B}_d \to \overline{K}^{*0}\mu^+\mu^-$." PoS(2008LHC)086. Talk at Physics at the LHC, 29.9.-4.10.2009, Split, Croatia.

[5] **LHC*b*** Collaboration, W. Reece, "$\overline{B}_d \to \overline{K}^{*0}\mu^+\mu^-$ at LHC*b*." PoS(BEAUTY2009)051. Talk at Beauty, 7.-11.9.2009, Heidelberg, Germany.

[6] U. Egede, T. Hurth, J. Matias, M. Ramon and W. Reece, "New physics reach of the mode $B_d \to K^* l^+ l^-$: *CP* violating observables." PoS(EPS-HEP2009)184. Talk at EPS, 16.-22.7.2009, Krakow, Poland; U. Egede, T. Hurth, J. Matias, M. Ramon and W. Reece, "The exclusive $B_d \to K^* l^+ l^-$ decay: *CP* violating observables." Talk at FLAVIAnet, 23.-27.7.2009, Kazimierz, Poland, 0912.1339; U. Egede, T. Hurth, J. Matias, M. Ramon and W. Reece. In preparation.

[7] A. Bharucha and W. Reece, *Constraining new physics with* $B_d \to K^{*0}\mu^+\mu^-$ *in the early LHC era*, 1002.4310.

[8] **LHC*b*** Collaboration, B. Adeva *et. al.*, *Roadmap for selected key measurements of LHC*b, 0912.4179.

[9] J. T. Moscicki *et. al.*, GANGA*: a tool for computational-task management and easy access to Grid resources*, *Computer Physics Communications* **180** (2009), no. 11 2303–2316 [0902.2685].

[10] D. Clowe *et. al.*, *A direct empirical proof of the existence of dark matter*, *Astrophys. J.* **648** (2006) L109–L113 [astro-ph/0608407].

[11] F. Zwicky, *On the masses of nebulae and of clusters of nebulae*, *Astrophys. J.* **86** (1937) 217–246.

[12] **WMAP** Collaboration, E. Komatsu *et. al.*, *Five-year Wilkinson Microwave Anisotropy Probe (WMAP) observations: Cosmological interpretation*, *Astrophys. J. Suppl.* **180** (2009) 330–376 [0803.0547].

[13] J. R. Primack, *Dark matter and structure formation*, astro-ph/9707285. In *Formation of Structure in the Universe*, Proceedings of the Jerusalem Winter School 1996, edited by A. Dekel and J.P. Ostriker (Cambridge University Press).

[14] G. Kane and S. Watson, *Dark matter and LHC: What is the connection?*, *Mod. Phys. Lett.* **A23** (2008) 2103–2123 [0807.2244].

[15] S. Dimopoulos and H. Georgi, *Softly broken supersymmetry and SU(5)*, *Nucl. Phys.* **B193** (1981) 150.

[16] P. Huet and E. Sather, *Electroweak baryogenesis and standard model CP violation*, *Phys. Rev.* **D51** (1995) 379–394 [hep-ph/9404302].

[17] **Muon (g-2)** Collaboration, G. W. Bennett *et. al.*, *An improved limit on the muon electric dipole moment*, *Phys. Rev.* **D80** (2009) 052008 [0811.1207].

[18] L. Evans and P. Bryant, *LHC machine*, *JINST* **3** (2008) S08001.

[19] J. R. Ellis, *Beyond the standard model with the LHC*, *Nature* **448** (2007) 297–301.

[20] **Heavy Flavor Averaging Group (HFAG)** Collaboration, E. Barberio *et. al.*, *Averages of B–hadron properties at the end of 2006*, 0704.3575. Updated results and plots available at: http://www.slac.stanford.edu/xorg/hfag/.

[21] S. L. Glashow, *Partial symmetries of weak interactions*, *Nucl. Phys.* **22** (1961) 579–588.

[22] S. Weinberg, *A model of leptons*, *Phys. Rev. Lett.* **19** (1967) 1264–1266.

[23] A. Salam, *Weak and electromagnetic interactions*, . Originally printed in Svartholm: Elementary Particle Theory, Proceedings Of The Nobel Symposium Held 1968 At Lerum, Sweden, Stockholm 1968, 367-377.

[24] P. W. Higgs, *Broken symmetries, massless particles and gauge fields*, *Phys. Lett.* **12** (1964) 132–133.

[25] P. W. Higgs, *Spontaneous symmetry breakdown without massless bosons*, *Phys. Rev.* **145** (1966) 1156–1163.

[26] G. S. Guralnik, C. R. Hagen and T. W. B. Kibble, *Global conservation laws and massless particles*, *Phys. Rev. Lett.* **13** (1964) 585–587.

[27] T. W. B. Kibble, *Symmetry breaking in non-abelian gauge theories*, *Phys. Rev.* **155** (1967) 1554–1561.

[28] N. Cabibbo, *Unitary symmetry and leptonic decays*, *Phys. Rev. Lett.* **10** (1963) 531–533.

[29] M. Kobayashi and T. Maskawa, *CP violation in the renormalizable theory of weak interaction*, *Prog. Theor. Phys.* **49** (1973) 652–657.

[30] T. Mannel, *Effective field thories in flavour physics*, *Springer Tracts Mod. Phys.* **203** (2004) 1–175.

[31] M. E. Peskin and D. V. Schroeder, *An introduction to quantum field theory*, . Reading, USA: Addison-Wesley (1995) 842 p.

[32] S. Weinberg, *The Quantum theory of fields. Vol. 1: Foundations*, . Cambridge Univ. Pr. (1995) 609 p.

[33] S. Weinberg, *The Quantum theory of fields. Vol. 2: Modern applications*, . Cambridge Univ. Pr. (1996) 489 p.

[34] R. K. Ellis, W. J. Stirling and B. R. Webber, *QCD and collider physics*, *Camb. Monogr. Part. Phys. Nucl. Phys. Cosmol.* **8** (1996) 1–435.

[35] A. V. Manohar and M. B. Wise, *Heavy quark physics*, *Camb. Monogr. Part. Phys. Nucl. Phys. Cosmol.* **10** (2000) 1–191.

[36] C. S. Wu, E. Ambler, R. W. Hayward, D. D. Hoppes and R. P. Hudson, *Experimental test of parity conservation in β decay*, *Phys. Rev.* **105** (1957) 1413–1414.

[37] C.-N. Yang and R. L. Mills, *Conservation of isotopic spin and isotopic gauge invariance*, *Phys. Rev.* **96** (1954) 191–195.

[38] **ALEPH, CDF, D0, DELPH, L3, OPAL, SLD** Collaborations, *Precision Electroweak Measurements and Constraints on the Standard*

Model, 0911.2604. Updated results and plots available at: http://lepewwg.web.cern.ch/LEPEWWG/.

[39] **Gfitter** Collaboration, H. Flacher *et. al.*, *Revisiting the global Electroweak fit of the Standard Model and beyond*, *Eur. Phys. J.* **C60** (2009) 543–583 [0811.0009]. Updated results and plots available at: http://gfitter.desy.de/.

[40] H. Yukawa, *On the interaction of elementary particles*, *Proc. Phys. Math. Soc. Jap.* **17** (1935) 48–57.

[41] **Particle Data Group** Collaboration, C. Amsler *et. al.*, *Review of particle physics*, *Phys. Lett.* **B667** (2008) 1.

[42] L. Wolfenstein, *Parametrization of the Kobayashi-Maskawa Matrix*, *Phys. Rev. Lett.* **51** (1983) 1945.

[43] **CKMfitter Group** Collaboration, J. Charles *et. al.*, *CP violation and the CKM matrix: Assessing the impact of the asymmetric B factories*, *Eur. Phys. J.* **C41** (2005) 1–131 [hep-ph/0406184]. Updated results and plots available at: http://ckmfitter.in2p3.fr.

[44] **UTfit** Collaboration, M. Bona *et. al.*, *The unitarity triangle fit in the standard model and hadronic parameters from lattice QCD: A reappraisal after the measurements of* Δm_s *and* $\mathcal{B}(B \to \tau\nu_\tau)$, *JHEP* **10** (2006) 081 [hep-ph/0606167]. Updated results and plots available at: http://www.utfit.org.

[45] **CKMFitter** Collaboration, K. Trabelsi. Talk at Beauty 2009, 11-11.09.2009, Evian, Germany. PoS(BEAUTY2009)016.

[46] T. Appelquist and J. Carazzone, *Infrared singularities and massive fields*, *Phys. Rev.* **D11** (1975) 2856.

[47] **LHC*b*** Collaboration, S. Amato *et. al.*, "LHCb: Technical proposal." CERN-LHCC-98-004.

[48] R. Fleischer, *Electroweak penguin effects beyond leading logarithms in the b meson decays* $B^- \to K^-\Phi$ *and* $B^- \to \pi^-\bar{K}^0$, *Z. Phys.* **C62** (1994) 81–90.

[49] P. Gambino and P. Giordano, *Normalizing inclusive rare B decays*, *Phys. Lett.* **B669** (2008) 69–73 [0805.0271].

[50] E. Fermi, *An attempt of a theory of beta radiation. 1*, *Z. Phys.* **88** (1934) 161–177; F. L. Wilson, *Fermi's theory of beta decay*, *American Journal of Physics* **36** (1968), no. 12 1150–1160.

[51] K. G. Wilson, *Nonlagrangian models of current algebra*, *Phys. Rev.* **179** (1969) 1499–1512.

[52] C. Bobeth, M. Misiak and J. Urban, *Photonic penguins at two loops and m_t-dependence of $\mathcal{B}(B \to x_s l^+ l^-)$*, *Nucl. Phys.* **B574** (2000) 291–330 [hep-ph/9910220].

[53] C. Bobeth, A. J. Buras and T. Ewerth, *$\bar{B} \to X_s l^+ l^-$ in the MSSM at NNLO*, *Nucl. Phys.* **B713** (2005) 522–554 [hep-ph/0409293].

[54] M. Beneke, T. Feldmann and D. Seidel, *Systematic approach to exclusive $B \to V l^+ l^-, V\gamma$ decays*, *Nucl. Phys.* **B612** (2001) 25–58 [hep-ph/0106067].

[55] F. Kruger and J. Matias, *Probing new physics via the transverse amplitudes of $B^0 \to K^{*0}(\to K^-\pi^+) l^+ l^-$ at large recoil*, *Phys. Rev.* **D71** (2005) 094009 [hep-ph/0502060].

[56] W. Altmannshofer *et. al.*, *Symmetries and asymmetries of $B \to K^* \mu^+ \mu^-$ decays in the standard model and beyond*, *JHEP* **01** (2009) 019 [0811.1214].

[57] E. Lunghi and J. Matias, *Huge right-handed current effects in $B \to K^*(K\pi) l^+ l^-$ in supersymmetry*, *JHEP* **04** (2007) 058 [hep-ph/0612166].

[58] M. Gorbahn and U. Haisch, *Effective Hamiltonian for non-leptonic $|\Delta(F)| = 1$ decays at NNLO in QCD*, *Nucl. Phys.* **B713** (2005) 291–332 [hep-ph/0411071]; P. Gambino, M. Gorbahn and U. Haisch, *Anomalous dimension matrix for radiative and rare semileptonic B decays up to three loops*, *Nucl. Phys.* **B673** (2003) 238–262 [hep-ph/0306079]; M. Gorbahn, U. Haisch and M. Misiak, *Three–loop mixing of dipole operators*, *Phys. Rev. Lett.* **95** (2005) 102004 [hep-ph/0504194].

[59] A. J. Buras, *Weak Hamiltonian, CP violation and rare decays*, hep-ph/9806471. Les Houches Ecole d'été de physique théorique, session LXVIII. Elsevier (1999) 1644 p.

[60] M. Neubert, *Heavy quark symmetry*, *Phys. Rept.* **245** (1994) 259–396 [hep-ph/9306320].

[61] N. Isgur and M. B. Wise, *Weak decays of heavy mesons in the static quark approximation*, *Phys. Lett.* **B232** (1989) 113; N. Isgur and M. B. Wise, *Weak transition form factors between heavy mesons*, *Phys. Lett.* **B237** (1990) 527.

[62] E. Eichten and B. R. Hill, *Static effective field theory: 1/m corrections*, *Phys. Lett.* **B243** (1990) 427–431; H. Georgi, *An effective field theory for heavy quarks at low- energies*, *Phys. Lett.* **B240** (1990) 447–450.

[63] J. M. Flynn and N. Isgur, *Heavy quark symmetry: Ideas and applications*, *J. Phys.* **G18** (1992) 1627–1644 [hep-ph/9207223].

[64] M. J. Dugan and B. Grinstein, *QCD basis for factorization in decays of heavy mesons*, *Phys. Lett.* **B255** (1991) 583–588.

[65] C. W. Bauer, S. Fleming, D. Pirjol and I. W. Stewart, *An effective field theory for collinear and soft gluons: Heavy to light decays*, *Phys. Rev.* **D63** (2001) 114020 [hep-ph/0011336].

[66] C. W. Bauer, D. Pirjol and I. W. Stewart, *Soft-collinear factorization in effective field theory*, *Phys. Rev.* **D65** (2002) 054022 [hep-ph/0109045].

[67] C. W. Bauer, D. Pirjol and I. W. Stewart, *Power counting in the soft-collinear effective theory*, *Phys. Rev.* **D66** (2002) 054005 [hep-ph/0205289].

[68] **BELLE** Collaboration, A. Ishikawa *et. al.*, *Observation of the electroweak penguin decay* $B \to K^* l^+ l^-$, *Phys. Rev. Lett.* **91** (2003) 261601 [hep-ex/0308044].

[69] A. Ali, P. Ball, L. T. Handoko and G. Hiller, *A comparative study of the decays* $B \to (K, K^*) l^+ l^-$ *in Standard Model and supersymmetric theories*, *Phys. Rev.* **D61** (2000) 074024 [hep-ph/9910221].

[70] C. Bobeth, T. Ewerth, F. Kruger and J. Urban, *Analysis of neutral Higgs-boson contributions to the decays* $\bar{B}_s \to l^+ l^-$ *and* $\bar{B} \to K l^+ l^-$, *Phys. Rev.* **D64** (2001) 074014 [hep-ph/0104284].

[71] P. Colangelo, F. De Fazio, R. Ferrandes and T. N. Pham, *Exclusive* $B \to K^{(*)} l^+ l^-$, $B \to K^{(*)} \nu\bar{\nu}$ *and* $B \to K^* \gamma$ *transitions in a scenario with a single universal extra dimension*, *Phys. Rev.* **D73** (2006) 115006 [hep-ph/0604029].

[72] J. Dickens, V. Gibson, C. Lazzeroni and M. Patel, "Selection of the decay $B_d \to K^{*0} \mu^+ \mu^-$ at LHCb." CERN-LHCb-2007-038.

[73] M. Patel and H. Skottowe, "A Fisher discriminant selection for $B_d \to K^{*0}\mu^+\mu^-$." CERN-LHCb-2009-009.

[74] M. Beneke, T. Feldmann and D. Seidel, *Exclusive radiative and electroweak $b \to d$ and $b \to s$ penguin decays at NLO*, *Eur. Phys. J.* **C41** (2005) 173–188 [hep-ph/0412400].

[75] **BELLE** Collaboration, J. T. Wei *et. al.*, *Measurement of the differential branching fraction and forward-backword asymmetry for $B \to K(^*)l^+l^-$*, *Phys. Rev. Lett.* **103** (2009) 171801 [0904.0770].

[76] ***BABAR*** Collaboration, B. Aubert *et. al.*, *Measurements of branching fractions, rate asymmetries, and angular distributions in the rare decays $B \to K\ell^+\ell^-$ and $B \to K^*\ell^+\ell^-$*, *Phys. Rev.* **D73** (2006) 092001 [hep-ex/0604007].

[77] ***BABAR*** Collaboration, B. Aubert *et. al.*, *Angular distributions in the decays $B \to K^*\ell^+\ell^-$*, *Phys. Rev.* **D79** (2009) 031102 [0804.4412].

[78] **BELLE** Collaboration, A. Ishikawa *et. al.*, *Measurement of forward-backward asymmetry and Wilson coefficients in $B \to K^*l^+l^-$*, *Phys. Rev. Lett.* **96** (2006) 251801 [hep-ex/0603018].

[79] ***BABAR*** Collaboration, B. Aubert *et. al.*, *Direct CP, lepton flavor and isospin asymmetries in the decays $B \to K^{(*)}\ell^+\ell^-$*, *Phys. Rev. Lett.* **102** (2009) 091803 [0807.4119].

[80] **BELLE** Collaboration, I. Adachi *et. al.*, *Measurement of the differential branching fraction and forward-backward asymmetry for $B \to K^{(*)}l^+l^-$*, 0810.0335.

[81] **CDF** Collaboration, H. Miyake. PoS(HCP2009)033. Talk at HCP2009, 16-20.11.2009, Evian, France.

[82] A. K. Alok *et. al.*, *New-physics contributions to the forward-backward asymmetry in $B_d \to K^{*0}\mu^+\mu^-$*, *JHEP* **02** (2010) 053 [0912.1382].

[83] P. Gambino, U. Haisch and M. Misiak, *Determining the sign of the $b \to s$ gamma amplitude*, *Phys. Rev. Lett.* **94** (2005) 061803 [hep-ph/0410155].

[84] Image from http://accel-general.web.cern.ch/accel-general/.

[85] **ATLAS** Collaboration, G. Aad *et. al.*, *The ATLAS experiment at the CERN large hadron collider*, *JINST* **3** (2008) S08003.

[86] **CMS** Collaboration, R. Adolphi *et. al.*, *The CMS experiment at the CERN LHC*, *JINST* **3** (2008) S08004.

[87] **ALICE** Collaboration, K. Aamodt *et. al.*, *The ALICE experiment at the CERN LHC*, *JINST* **3** (2008) S08002.

[88] `http://twitter.com/CERN`.

[89] **LHC*b*** Collaboration, A. A. Alves *et. al.*, *The LHC*b *Detector at the LHC*, *JINST* **3** (2008) S08005.

[90] M. Patel and H. Skottowe, "A cut-based selection for $B_d \to K^{*0}\mu^+\mu^-$ at LHCb." CERN-LHCb-2009-008.

[91] Image from `http://lhcb-public.web.cern.ch/lhcb-public/`.

[92] M. Gandelman and E. Polycarpo, "The performance of the LHCb muon identification procedure." CERN-LHCb-2007-145.

[93] G. Lanfranchi, X. Cid Vidal, S. Furcas, M. Gandelman, J. A. Hernando, J. H. Lopez, E. Polycarpo and A. Sarti, "The muon identification procedure of the LHCb experiment for the first data." CERN-LHCb-2009-013.

[94] A. Sarti, S. Furcas, G. Lanfranchi and M. Palutan, "Calibration strategy and efficiency measurement of the muon identification procedure at LHCb." CERN-LHCb-2010-002.

[95] J.-A. Hernando Morata, "The 'hadron alley' description." CERN-LHCb-2009-034.

[96] S. Amato, A. Satta, B. Souza de Paula and L. De Paula, "HLT1 muon alley description." CERN-LHCb-2008-058.

[97] A. Pérez-Calero and H. Ruiz, "The muon+track alley of the LHCb high level trigger." CERN-LHCb-2008-075.

[98] K. Senderowska, M. Witek and A. Zuranski, "HLT1 Electromagnetic alley." LHCb-PUB-2009-001.

[99] B. Grinstein and D. Pirjol, *The forward-backward asymmetry in $B \to K\pi l^+l^-$ decays*, *Phys. Rev.* **D73** (2006) 094027 [`hep-ph/0505155`].

[100] F. Kruger, L. M. Sehgal, N. Sinha and R. Sinha, *Angular distribution and CP asymmetries in the decays $\overline{B} \to K^-\pi^+e^-e^+$ and $\overline{B} \to \pi^-\pi^+e^-e^+$*, *Phys. Rev.* **D61** (2000) 114028 [`hep-ph/9907386`].

[101] J. Charles, A. Le Yaouanc, L. Oliver, O. Pene and J. C. Raynal, *Heavy-to-light form factors in the heavy mass to large energy limit of QCD*, *Phys. Rev.* **D60** (1999) 014001 [hep-ph/9812358].

[102] J. Charles, A. Le Yaouanc, L. Oliver, O. Pene and J. C. Raynal, *Heavy–to–light form factors in the final hadron large energy limit: Covariant quark model approach*, *Phys. Lett.* **B451** (1999) 187 [hep-ph/9901378].

[103] M. Beneke and T. Feldmann, *Symmetry–breaking corrections to heavy–to–light B meson form factors at large recoil*, *Nucl. Phys.* **B592** (2001) 3–34 [hep-ph/0008255].

[104] P. Ball and R. Zwicky, $B_{d,s} \to \rho,\, \omega,\, K^*,\, \phi$ *decay form factors from light-cone sum rules reexamined*, *Phys. Rev.* **D71** (2005) 014029 [hep-ph/0412079].

[105] G. Burdman, *Short distance coefficients and the vanishing of the lepton asymmetry in* $B \to V l^+ l^-$, *Phys. Rev.* **D57** (1998) 4254–4257 [hep-ph/9710550].

[106] C. Bobeth, G. Hiller and G. Piranishvili, *CP asymmetries in* $\overline{B} \to \overline{K}^{*0}(\to \bar{K}\pi) l^+ l^-$ *and untagged* $\bar{B}_s, B_s \to \phi(\to K^- K^+) l^+ l^-$ *decays at NLO*, *JHEP* **07** (2008) 106 [0805.2525].

[107] U. Egede, "Angular correlations in the $\overline{B}_d \to \overline{K}^{*0} \mu^+ \mu^-$ decay." CERN-LHCb-2007-057.

[108] M. Beneke, A. P. Chapovsky, M. Diehl and T. Feldmann, *Soft-collinear effective theory and heavy-to-light currents beyond leading power*, *Nucl. Phys.* **B643** (2002) 431–476 [hep-ph/0206152].

[109] W. Verkerke and D. Kirkby, "The RooFit toolkit for data modelling." Talk at CHEP, 24.-28.3.2003, La Jolla, California, USA, physics/0306116.

[110] M. Galassi *et. al.*, *GNU Scientific Library Reference Manual*. Network Theory, 2009.

[111] M. Bauer, S. Casagrande, U. Haisch and M. Neubert, *Flavor physics in the Randall-Sundrum model: II. tree- level weak-interaction processes*, 0912.1625.

[112] J. Dickens, V. Gibson, C. Lazzeroni and M. Patel, "A study of the sensitivity to the forward-backward asymmetry in $B_d \to K^{*0}\mu^+\mu^-$ decays at LHCb." CERN-LHCb-2007-039.

[113] P. Ball and V. M. Braun, *Exclusive semileptonic and rare B meson decays in QCD*, *Phys. Rev.* **D58** (1998) 094016 [hep-ph/9805422].

[114] Source code available from `https://svnweb.cern.ch/trac/evtbtokstmumu`.

[115] T. Sjostrand *et. al.*, *High-energy physics event generation with PYTHIA 6.1*, *Comput. Phys. Commun.* **135** (2001) 238–259 [hep-ph/0010017].

[116] G. Corcella *et. al.*, *HERWIG 6.5: an event generator for Hadron Emission Reactions With Interfering Gluons (including supersymmetric processes)*, *JHEP* **01** (2001) 010 [hep-ph/0011363].

[117] D. J. Lange, *The* EvtGen *particle decay simulation package*, *Nucl. Instrum. Meth.* **A462** (2001) 152–155.

[118] A. Ryd, D. Lange, N. Kuznetsova, S. Versille, M. Rotondo, D. Kirkby, F. Wuerthwein and A. Ishikawa, EvtGen*: A Monte Carlo Generator for B–Physics*, 2005. `http://www.slac.stanford.edu/~lange/EvtGen/`.

[119] Q.-S. Yan, C.-S. Huang, W. Liao and S.-H. Zhu, *Exclusive semileptonic rare decays $B \to (K, K^{*0})l^+l^-$ in supersymmetric theories*, *Phys. Rev.* **D62** (2000) 094023 [hep-ph/0004262].

[120] P. Ball. Private communication, 2009.

[121] T. Appelquist, H.-C. Cheng and B. A. Dobrescu, *Bounds on universal extra dimensions*, *Phys. Rev.* **D64** (2001) 035002 [hep-ph/0012100].

[122] **CDF** Collaboration, T. Aaltonen *et. al.*, *Search for $B_s^0 \to \mu^+\mu^-$ and $B_d^0 \to \mu^+\mu^-$ decays with $2fb^{-1}$ of $p\bar{p}$ collisions*, *Phys. Rev. Lett.* **100** (2008) 101802 [0712.1708]; **CDF** Collaboration, "Search for $B_s^0 \to \mu^+\mu^-$ and $B_d^0 \to \mu^+\mu^-$ decays with $3.7fb^{-1}$ of $p\bar{p}$ collisions." CDF Public Note 9892, 2009.

[123] W. Altmannshofer, A. J. Buras and P. Paradisi, *Low energy probes of CP violation in a flavor blind MSSM*, *Phys. Lett.* **B669** (2008) 239–245 [0808.0707].

[124] W. Altmannshofer. Private communication, 2009.

[125] E. Gabrielli and S. Khalil, *On the $B \to X_s l^+ l^-$ decays in general supersymmetric models*, *Phys. Lett.* **B530** (2002) 133–141 [hep-ph/0201049].

[126] F. Kruger and L. M. Sehgal, *CP violation in the decay $B \to X_d e^+ e^-$*, *Phys. Rev.* **D55** (1997) 2799–2805 [hep-ph/9608361].

[127] A. Ali, T. Mannel and T. Morozumi, *Forward backward asymmetry of dilepton angular distribution in the decay $b \to s l^+ l^-$*, *Phys. Lett.* **B273** (1991) 505–512.

[128] F. Jansen, N. Serra, G. Y. Smit and N. Tuning, "Determination of the forward-backward asymmetry in the decay $B_d \to K^{*0} \mu^+ \mu^-$ with an unbinned counting analysis." CERN-LHCb-2009-003, May, 2009.

[129] M. Oreglia, *A study of the reaction $\Psi' \to \gamma\gamma\Psi$*. PhD thesis, SLAC, 1980. SLAC-R-236.

[130] ***BABAR*** Collaboration, B. Aubert *et. al.*, *Measurement of the $B \to X_s \ell^+ \ell^-$ branching fraction with a sum over exclusive modes*, *Phys. Rev. Lett.* **93** (2004) 081802 [hep-ex/0404006].

[131] **BELLE** Collaboration, M. Iwasaki *et. al.*, *Improved measurement of the electroweak penguin process $B \to X_s l^+ l^-$*, *Phys. Rev.* **D72** (2005) 092005 [hep-ex/0503044].

[132] G. Hiller and F. Kruger, *More model-independent analysis of $b \to s$ processes*, *Phys. Rev.* **D69** (2004) 074020 [hep-ph/0310219].

[133] A. Ghinculov, T. Hurth, G. Isidori and Y. P. Yao, *The rare decay $B \to X_s l^+ l^-$ to NNLL precision for arbitrary dilepton invariant mass*, *Nucl. Phys.* **B685** (2004) 351–392 [hep-ph/0312128].

[134] D. Guetta and E. Nardi, *Searching for new physics in rare $B \to \tau$ decays*, *Phys. Rev.* **D58** (1998) 012001 [hep-ph/9707371].

[135] T. Hurth, G. Isidori, J. F. Kamenik and F. Mescia, *Constraints on new physics in MFV models: A model- independent analysis of $\Delta F = 1$ processes*, *Nucl. Phys.* **B808** (2009) 326–346 [0807.5039].